

GROUND BASED THz SPECTROSCOPY OF
OBSCURED STARBURSTS IN THE EARLY
UNIVERSE ENABLED BY
THE 2nd GENERATION z (REDSHIFT) & EARLY
UNIVERSE SPECTROMETER

A Dissertation

Presented to the Faculty of the Graduate School
of Cornell University

in Partial Fulfillment of the Requirements for the Degree of
Doctor of Philosophy

by

Amit Vishwas

May 2019

© 2019 Amit Vishwas
ALL RIGHTS RESERVED

GROUND BASED THz SPECTROSCOPY OF
OBSCURED STARBURSTS IN THE EARLY UNIVERSE ENABLED BY
THE 2nd GENERATION z (REDSHIFT) & EARLY UNIVERSE
SPECTROMETER

Amit Vishwas, Ph.D.

Cornell University 2019

Galaxies were surprisingly dusty in the early Universe, with more than half of the light emitted from stars being absorbed by dust within the system and re-radiated into far infrared (FIR, $\sim 50\text{-}150\ \mu\text{m}$) wavelengths. Dusty star forming galaxies (DSFGs) dominate the co-moving star formation rate density of the Universe that peaks around redshift, $z\sim 2$, making it compelling to study them in rest frame FIR bands. From galaxies at $z>1$, the FIR line emission from abundant ions like O^{++} , C^+ and N^+ , are redshifted into the short sub-mm telluric windows.

My thesis work is based on upgrading and deploying the 2nd Generation z (Redshift) and Early Universe Spectrometer (ZEUS-2), a long-slit, echelle grating spectrometer optimized to study broad ($\Delta v = 300\ \text{km s}^{-1}$) spectral lines from galaxies in the $200\text{-}650\ \mu\text{m}$ telluric windows using TES bolometers. These far-IR lines being extinction free and major coolants of the gas heated by (young) massive stars, are powerful probes of the physical conditions of the gas and the stellar radiation field.

I present results from our observations of the $[\text{O III}] 88\ \mu\text{m}$ line in galaxies at redshift, $z\sim 3\text{-}4$, with ZEUS-2 at the Atacama Pathfinder Experiment (APEX) Telescope. To interpret our observations along with ancillary data from optical

to radio facilities, we apply photo-ionization models for HII regions and Photo Dissociation Region (PDR) models and confirm that the galaxies host substantial ongoing obscured star formation. The presence of doubly ionized oxygen suggests hard radiation fields and often elevated ionization parameters that can only be accounted for by a population of massive stars formed during the ongoing starburst, that contribute a large fraction of the infrared luminosity. This work highlights the use of FIR line emission to trace the assembly of current day massive galaxies, details of their stellar populations and physical conditions of the interstellar medium undergoing rapid star-formation activity.

BIOGRAPHICAL SKETCH

Amit Vishwas was born in Mandsaur, a small town in rural central India in April 1986. He has no memories of the first few years of his life till he moved to the city of Bhopal with his mother and close to his grandparents. He has one sibling, a younger brother Aman, who is a real-life rock star.

Amit finished his schooling in Bhopal from Jawaharlal Nehru School in 2004, made some friends for life and was eager to learn more astronomy, chemistry, coding and geography. He then moved to the shores of the Arabian sea to pursue a Bachelor of Technology degree at the National Institute of Technology Karnataka in Surathkal. For his final year project, he worked with Prof. Tushar Prabhu at the Indian Institute of Astrophysics to build a automated all-sky camera for a remote observatory in the Himalayas and its image processing pipeline. This first hand experience at the intersection of hand-on instrumentation and programming sparked his interest towards pursuing more opportunities for instrumentation in astronomy. It was while debugging a circuit when due to a lucky co-incidence he crossed paths with one of the most intelligent, caring and sensitive person he has known and his partner through thick and thin since, Bhargavi Narayanasetty. He received his B.Tech degree in Information Technolgy with a focus on computer networking and signal processing from NITK Surathkal in 2009.

He moved *far above Cayuga's waters* to Ithaca, NY in July 2009 to purse a Master of Engineering degree in Electrical and Computer Engineering at Cornell University. Along with the M.Eng coursework, he started work on a feasibility study for a focal plane phased array feed for the Arecibo radio telescope with Dr. Germán Cortés and received his degree in August 2010. He joined the National Astronomy and Ionosphere Center and continued working on the phased array feed project with Germán and Prof. Donald Campbell. Amit joined the Astronomy department as a graduate student in August 2011 and has worked on two instruments; a novel cryogenically cooled phased array feed camera, AO-19 for the Arecibo radio telescope and a direct-detection sub-mm grating spectrometer, ZEUS-2. He helped assemble, characterize and deploy AO-19 for a field test in Summer 2013. Soon after, he joined the sub-mm Astrophysics

group, working with Prof. Gordon Stacey and blue-shifted the operating wavelength, working on the 2nd generation z(Redshift) and Early Universe Spectrometer (ZEUS-2). These years through graduate school were a whirlwind journey of learning physics then learning astrophysics, drowning in coffee, three seasons of high altitude observing at APEX, *detailed* balance, soldering, not so much coffee, wire bonding, extreme galaxies in the early Universe and proposal writing. He is glad to have crossed the finish line and will continue to work with astronomical instrumentation. Amit received the 2018 Roger Doxsey Travel Prize for presenting his dissertation research at the 231st annual meeting of the American Astronomical Society. His next endeavor is to design and build the cryostat for the Advanced Cryogenic L-band Phased Array Camera for the Arecibo Radio Telescope (ALPACA).

This thesis is dedicated to my Grand Parents,
Dr. Ramesh Chandra Singhai Shri Bhagwan Das Arakh
&
Smt. Hemlata Singhai Smt. Sumitra Devi

ACKNOWLEDGEMENTS

Writing these words of thanks as the final pieces of this dissertation, I am humbled by knowing that I have had the support and good wishes of so many people in my life. This work spread over the past many years has been made possible by the effort, advice, support and encouragement of so many collaborators and friends. Foremost, I am grateful to my thesis advisor Gordon Stacey, who has always supported and motivated me to do my best. Gordon, I am *still* learning to practice, 'The enemy of good is better'. I am fortunate to have your insight and guidance to help me identify the scientifically interesting questions in a lucid way. I consider myself lucky to have found a mentor in Germán Cortés, you have always been there listen to me patiently and provide sound advice. I admire your enthusiasm, far-sightedness, clarity of thought and your design sense. I have learned much about SQUID readout and debugging the MCE through formal and informal interactions with Mike Niemack and his group, thank you for always being willing to help and also letting me use your lab equipment at multiple occasions. I am also grateful to Jonathan Lunine and Don Campbell who shared their personal wisdom and encouraging advice that made the first half of graduate school possible.

I would like to thank from the bottom of my heart the two support pillars of the sub-mm Astrophysics group; Thomas Nikola and Steve Parshley. I am grateful for your help and guidance in the lab, your infinite patience with me on the observing runs, for being the moderating voice and for your scientific and technical acumen. It might have taken me a little bit but I strongly subscribe to the tenet - when in doubt, trust Thomas. Without Steve's work, ZEUS-2 would not be a reality, and for your ability to bring ideas from my flights of imagination to real implementable solutions, you are a wizard. I have to thank Chuck Henderson for teaching me everything I know about soldering and vacuum instruments. You were always enthusiastic about helping me track down a problem in the lab, electronic or mechanical. I am also indebted to Steve, Chuck and George Gull for helping me setup and use the department machine shop and machining help on more than one occasion at a short notice. ZEUS-2's deployment at the telescope would not be possible without Justin Schoenwald's herculean efforts with the ZEUS-2

data acquisition system. I thank you for your unwavering support during observing and thorough testing of the software system that made all the science observations possible. Thanks for being on all night long Skype calls and working with me on-the-fly while we were at the telescope. Thank you Sarah Higdon who selflessly gave her time and energy at times when I was struggling to put my thoughts on paper and for her constant appreciation and encouragement that helped me overcome impostor syndrome. Thank you Jim Higdon for your patience and support during all the observing trips, for your light-hearted humor and finding the flamingos in the desert. I am indebted to Carl Ferkinhoff for showing me the ropes with ZEUS-2, educating me about the ADR, TES bolometers and all the little quirks of ZEUS-2. I thank you for always being my sounding board for ideas with ZEUS-2 and having sharp insights and thoughtful advice for my attempts at exploring the ISM of galaxies in the early Universe.

I am grateful for the work of Sherry Cho on the 200 μm array and backshorts, and the support from Gene Hilton, Johnnaes Hubmayr and the Quantum Sensors group at NIST Boulder for their help with assembly of the new arrays and screening the readout components. I am thankful to Matthew Hasselfield for sharing his knowledge of the MCE to save the day and get the readout system for the new arrays on ZEUS-2 working. Thank You Carole Tucker and Ken Wood for providing us the filters used in ZEUS-2. I'd also like to acknowledge the help of the ACT team for allowing us to borrow a compressor at the high plateau and saving an observing run. Finally, thanks are in order to all of the incredible staff at the APEX telescope that made the deployment on the telescope possible. I'd particularly like to thank Rolf Güsten, Karl Menten, and Axel Weiß for their continued support of ZEUS-2 both in science and at the telescope, and Oriol Arriagada for their tireless help in sometimes difficult situations at the telescope. Thank you Christopher for taking over the instrument from where I left off and your work to use ZEUS-2 to its full potential.

On a more personal side, I could not be more fortunate to have shared my time at Cornell with people who have brought their positive influence in my life and I am proud to have known. Thank you to all the grad students in my year (Luke, Michael,

Mike, Tyler, Sean, ZZ, Jason, Dong and Ryan), I had the good fortune to share an office with Everett and Riccardo, senior grads (Laura, Drew, Ann, Betsey, Manolis, Dan, Ryan and Eva) and good friends (Matt, Paul, Sam, Michelle, Eve, Nic, and Jack). Thank you to the incredible staff of the Astronomy Department, Lynda, Monica, Jessica, Tom, Dave and Bez for always having a solution to whatever problem I had (or created).

Thank you Riccardo for being a loyal friend and a constant pillar of support for me through some tough times and for sharing the good times. Thank you Paul for letting me sleep on your couch while I finished this dissertation. Thank you Michael, Cody, Avani and Daisy for indulging my many impromptu afternoon chats about science, life and everything else. To my roommate Abhinandan and my fellow Villagers, Tanay, Ishita, Mihir and Adarsh, my oldest friends in life, Akriti, Mohit, Aditya, Anand and Sumit - thank you all for being there and never letting us grow old. Your presence in my life is the light that keeps me going. No expression of gratitude is enough to pay my respects to my grandparents and parents, who shielded me from the world and encouraged me to pursue my dreams. To my dearest brother, I love you and I am proud of you. Finally, I thank those elusive LEDs that I couldn't find anywhere, because they led me to the brightest light of my life, Bhargavi – thank you for sharing this journey with me and filling my life with love and happiness, you are my true North.

In my time at Cornell, my research and work on ZEUS-2 was primarily supported by NSF grants including ATI-1105874 and AAG 1109476 and AAG-1716229. I was also partially supported by NASA grant NNX17AF37G, and SOFIA grant SOF04-0179 to undertake science very similar to that with ZEUS-2 but with nearby galaxies. I would also like to acknowledge the support from Cornell graduate school research and conference travel grants and the Einuadi Center international research travel grant. This work was performed in part at Cornell NanoScale Facility, an NNCI member supported by NSF Grant NNCI-1542081. The research presented in this work is primarily made possible with data collected on the APEX telescope. APEX is a collaboration between the Max-Planck-Institut für Radioastronomie, the European Southern Observatory, and the Onsala Space Observatory.

TABLE OF CONTENTS

Biographical Sketch	iii
Dedication	v
Acknowledgements	vi
Table of Contents	ix
List of Tables	xi
List of Figures	xii
1 Scientific Motivation	1
1.1 From the Dark Ages to the Cosmic Noon	1
1.2 Star-formation at high redshift: The diagnostic power of Far-Infrared, Fine Structure lines	4
2 Completing ZEUS-2: Integration of the 200/645 μm TES Bolometer Array and Deployment at APEX	7
2.1 The Second Generation Redshift(z) and Early Universe Spectrometer (ZEUS-2)	7
2.1.1 A Dry Cryostat	12
2.1.2 Detectors and Read out components	18
2.1.3 Optical Filtration	21
2.2 Warm Optics	25
2.3 Grating Optimization to tune Operational Range to Telluric Windows and Maximize Efficiency	27
2.4 Integration of the 215/645 μm TES Bolometer Array in ZEUS-2	31
3 Detection of [O III] at $z\sim 3$: A Galaxy above the Main-Sequence, rapidly assembling its Stellar Mass	41
3.1 Abstract	41
3.2 Introduction	42
3.3 ZEUS-2/APEX Observations and results	46
3.3.1 [O III] line emission: Young stars and Ionized gas mass	48
3.4 Supporting Observations	50
3.4.1 Archival: Hubble Space Telescope WFC3	51
3.4.2 Archival: Spitzer Space Telescope	53
3.4.3 Archival: Wide-field Infrared Survey Explorer	54
3.4.4 Archival: Herschel Space Telescope	55
3.5 Discussion	58
3.5.1 UV-to-mm Spectral Energy Distribution	58
3.5.2 Constraining the Stellar Population	61
3.5.3 Conditions of Interstellar gas and dust	64
3.5.4 Is G12v2.43 strongly lensed?	68
3.6 Results & Conclusions	70

4	Zoom-in to Galaxy Assembly: A Resolved Study of A Highly Magnified Galaxy at $z \sim 4.2$ Through Far-Infrared Radiation	72
4.1	Abstract	72
4.2	Introduction	73
4.3	Observations	79
4.3.1	ZEUS-2/APEX observations of the [O III] $88 \mu\text{m}$ line	79
4.3.2	ALMA Cycle 4 observations	80
4.3.3	Supporting Observations	85
4.4	Results	89
4.4.1	ZEUS-2 detection of the [O III] $88 \mu\text{m}$ line emission	89
4.4.2	Dust Continuum Maps of SPT0418-47	90
4.4.3	ALMA maps of the [C II] and [N II] line emission	91
4.5	Discussion	94
4.5.1	Estimating the Ionized Gas contribution to the [C II] line	96
4.5.2	A Young Starburst and Ionized Gas	98
4.5.3	Optical-to-cm Spectral Energy Distribution	103
4.5.4	Resolved Maps of the Dust Continuum Emission	108
4.6	Conclusions	115
5	Future Work	118
5.1	Discovery of a compact sub-arcsecond Einstein Ring with ALMA	118
5.1.1	Introduction	118
5.1.2	Observations	119
5.1.3	Gravitational Lens Modeling	120

LIST OF TABLES

2.1	Tuning range for all grating orders with corresponding filter cut-offs	24
3.1	Photometry Data for G12v2.43	54
3.2	Far-IR Fine Structure Lines in PACS/SPIRE Observations of G12v2.43	57
3.3	Derived Physical Properties of G12v2.43	62
4.1	Photometry Data for SPT0418-47	84
4.1	Photometry Data for SPT0418-47	85
4.2	Measured Line Properties of SPT0418-47	93
4.3	Calculation of Ionized Gas Mass with various tracers and comparison to other Baryonic components of SPT0418-47	102
4.4	Derived Physical Properties of SPT0418-47	108
4.5	Best-fit Lens Model parameters for 200 μm continuum observations of SPT0418-47 compared with rest-frame 166 μm model from literature	109

LIST OF FIGURES

2.1	An overview of the ZEUS-2 Cryostat and its various sub-systems.	8
2.2	Temperature on the 1 K and 100 mK stages during an ADR cycle	16
2.3	An overview of the cold optics inside ZEUS-2 and the focalplane	19
2.4	Transmission plots of all the filters currently in use inside ZEUS-2.	21
2.5	Atmospheric transmission identifying the telluric windows along with the Filter transmission relevant to individual grating orders	22
2.6	An overview of the warm fore-optics used at APEX to couple the telescope beam to ZEUS-2	26
2.7	Grating efficiency curves for the new grating design used for ZEUS-2	29
2.8	Copper carrier for the 215/645 μm detector array in ZEUS-2 . . .	33
2.9	The PCB and Silicon fanout board that house the readout components and carry the 215/645 μm array before wire bonding all the components.	36
3.1	ZEUS-2/APEX spectrum of the OIII 88 μm emission line observed in G12v2.43	47
3.2	SMA sub-mm continuum contours for G12v2.43 overlaid on the HST/WFC3 near-IR image	52
3.3	Spectral Energy Distribution fit for G12v2.43 using broadband photometry with CIGALE and MAGPHYS	59
4.1	Source integrated spectrum of the the [O III], [C II] and [N II] lines in SPT0418-47	89
4.2	Dust continuum map of SPT0418-47 at rest-frame 160 μm	90
4.3	Dust continuum map of SPT0418-47 at rest-frame 200 μm	91
4.4	Map of the [C II] 158 μm line emission from SPT0418-47	93
4.5	Map of the [N II] 205 μm line emission from SPT0418-47	94
4.6	Spatial variation of the [C II] / [N II] ratio across SPT0418-47 . . .	98
4.7	Best-fit Modified Blackbody Spectral Energy Distribution fit for SPT0418-47	107
4.8	Best-fit gravitational lensing model for the observed emission from SPT0418-47 using <i>uvmmcmcf</i>	110
4.9	Brightness temperature map of SPT0418-47 using high resolution continuum observations	112
4.10	Spectral index map ($S_\nu \propto \nu^\alpha$) as calculated for dust continuum emission seen at 160 μm and 200 μm from SPT0418-47	113
5.1	Best fit gravitational lensing model for the [C II] emission seen from G12v2.43	120
5.2	Residuals between the observed emission and the best fit gravitational lensing model shown above.	121

5.3	Probability distribution of the parameter values used to estimate the best-fit model for the lensing galaxy and the source for observed emission from G12v2.43	122
5.4	Estimates of star-formation rate and mass within the Einstein ring as a function of lens redshift required to reproduce the observed lensing configuration and continuum detection at the center of the ring respectively	124
5.5	Estimates of the mass of the lensing galaxy - within the Einstein ring based on gravitational lensing models and, the ISM based on dust continuum detection	125

CHAPTER 1

SCIENTIFIC MOTIVATION

1.1 From the Dark Ages to the Cosmic Noon

The Cosmic Microwave Background (CMB) is an incredibly powerful tool to observe the veil that the surface of last scattering (at $z \sim 1100$) throws at everything that happened before then and going back to the moment that marks the beginning of the Universe, the Big Bang. It represents the time when free electrons could, for the first time since the birth of the Universe, combine with protons to form neutral hydrogen, allowing photons to decouple from the soup of hot plasma and propagate freely. The CMB is remarkably uniform but has small anisotropies that yield rich information about the formation of the Universe and its current contents and geometry. These anisotropies have been observed in great detail by multiple generations of space- and ground-based experiments (e.g., [Fixsen et al., 1996](#), [Komatsu et al., 2011](#), [Planck Collaboration et al., 2018](#)), ushering the era of 'precision cosmology' (for a recent review see [Staggs et al., 2018](#)). It is the diagnostic power in these details that allows us to constrain the processes at work beyond the veil – from concordance cosmology with Dark Energy and Dark Matter making up most of the observable Universe and understanding the origins of our (perhaps, one of many) Universe by constraining the events of the initial fraction of a second after the Big Bang, that so far remains consistent with the period of rapid inflation.

As this nascent Universe continued expanding, other than the fading light of the CMB, no other sources of light were present, and the Universe was engulfed in what we refer to as the Dark Ages of the Universe. During these dark

ages, the many microscopic fluctuations in the CMB start to evolve and play a formative role for the future of the Universe. As per our current understanding these fluctuations grew for the next many millions of years with the help of an elusive kind of matter (electromagnetically “dark”) and under the influence of gravity until they became massive enough to trigger the formation of the first stars and galaxies.

As hinted above, with time and the help of dark matter and gravity, the pristine neutral hydrogen gas could condense within small regions of space and form objects that were energetic enough to re-ionize the surrounding neutral hydrogen. As the Universe has expanded roughly a factor of 50 in voids, the gas density was diluted by $\sim 50^3$ as compared to before recombination, such that the scattering between photons and electrons in the voids was no longer important. These objects responsible for re-ionization, like stars, galaxies and quasars, spread and evolved and so did the gas being ionized by them. Within less than a billion years of the first sources appearing, in what is now referred to as the era of re-ionization ($6 < z < 20$), the entire Universe was filled with low density, and very high ionized fraction hydrogen gas. This process likely took place quickly and therefore brought an end to the era of re-ionization and the Universe becoming lit up with the light of newly formed stars and galaxies that we are discovering today.

The preceding description is a simplistic understanding of the otherwise intricate, and for many details, still mysterious processes of nature. The assembly and evolution of ordered structure in the Universe, that stars and galaxies are examples of, is accompanied by release of energy across a broad spectrum. In a Universe that has perfect housekeeping and is free of any dust, the overall

extragalactic background light (EBL) could be modeled simply as a sum of all components whose energy spectrum is known. In the presence of dust, the total integrated radiant power remains nearly the same (some energy is used to heat the dust particles) but the spectrum is reprocessed and energy is radiated back at different wavelengths depending on a myriad of factors related to the formation and properties of the dust, and more importantly, on the time evolution of the sources that contribute to the overall background. This background is independent of the CMB whose power arises from the hot plasma of the expansion in the early Universe. The holy grail of galaxy formation and evolution studies is to resolve this background, into its constituent galaxies, and understand the influence of various mechanisms that regulate structure formation, as the Universe evolves from the Cosmic dawn to the epoch of peak star-formation rate density, also referred to as Cosmic Noon, and up to today, where we attempt to piece together this history and understand our place in the Universe.

The familiar sights of the night sky (aka the Cosmic Optical Background) has been of interest and studied well for the past few centuries. It is only in the past 70 years, that discoveries of new materials and their applications to detect mid and far-infrared radiation have picked up pace. This rapid advancement in technology has fueled new instrumentation and the infrared/radio astronomy community has been making the most use of it to grow our knowledge of the cosmos. Back with the COBE satellite, we detected that the Cosmic Infrared Background is energetically equal to or even somewhat stronger than the Optical counterpart. With the help of a growing array of ground, air and space based instruments, we have been able to even resolve this background into bright galaxies out to a redshift of 3 (two billion years after the Big Bang), and discover that the most vigorous star-formation activity in the high -redshift

Universe is almost entirely obscured at optical wavelengths and requires observations at longer wavelengths to uncover it.

1.2 Star-formation at high redshift: The diagnostic power of Far-Infrared, Fine Structure lines

The star-formation rate density is observed to evolve strongly with the age of the Universe, with its peak being around $z \sim 2$. Straddling the peak, between redshifts of $z \sim 1-5$, is the epoch referred to as the cosmic noon of star-formation. This period is when galaxies are thought to have assembled their stellar masses and offers prime testing grounds for our theories of galaxy formation and evolution. Common optical lines arising from stellar atmospheres or the interstellar medium have revealed that the last evolutionary stages of the most massive of the first generation of stars must have seeded the Universe with copious amounts of metals. Observations have not yet convincingly found the epoch before the rise of metals, bright line emission of ionized oxygen has been observed at redshifts ~ 9.1 ([Hashimoto et al., 2018a](#)). Most of the rest-frame optical spectral lines that are traditionally used to constrain stellar populations, and physical conditions such as, radiation field, metallicity, and density, in the interstellar medium (ISM) of galaxies are blocked by the atmosphere at $z > 2-3$. To compound the problem, star-forming regions within galaxies even at their early growth phase are enveloped in a large amount of dust, making the optical lines difficult to detect and interpret even with the largest telescopes.

In order to observe an unbiased star-formation history of the Universe, the far-infrared bands are extremely helpful. The dust emission from these galaxies

typically peaks in the far-infrared ($\sim 30\text{-}200\ \mu\text{m}$) and we reap an added benefit of the negative k-correction, due to which as the redshift (i.e. distance) to a galaxy increases, the observed peak of the dust emission shifts to longer wavelengths, thereby negating the effect of geometric dimming. In addition, strong ground state fine structure transitions of multiple astrophysically important species lie within the far-IR range (like C^+ , C^0 , O^0 , O^{++} , N^+ , N^{++}). Spectral lines originating from these transitions, cool the interstellar medium and can emerge unimpeded by dust. As they are the primary coolants of much of the gas within the galaxies, they provide strong constraints on the intensity and extent of the star-formation activity that remains otherwise obscured.

Rest-frame far-infrared dust radiation from Cosmic Noon is almost entirely absorbed by the water vapor present in the Earth's atmosphere and makes it difficult to observe important tracers of activity and conditions of the interstellar medium in dusty star-forming galaxies. Significant progress in resolving the dust emission from high redshift galaxies has been made in the past decade due to far-IR and sub-mm observations made from the largest telescope ever launched in space (to date), the Herschel Space Observatory that was equipped with a passively cooled 3.5-m mirror. But unfortunately, its supply of cryogenics was exhausted in early 2013, and the instruments on-board are not operational anymore. NASA's Stratospheric Observatory for Infrared Astronomy (SOFIA), a 2.4-m telescope aboard a modified Boeing 747 airplane, flies above most of the Earth's atmosphere to allow observations at short wavelengths otherwise inaccessible to ground based facilities. Observations from SOFIA in the sub-mm band are not very compelling since its 2.5 m aperture means it will be confusion limited at much higher flux levels than Herschel, and it has a much warmer, more emissive telescope with significantly less integration time available.

Here we focus on detecting the diagnostic far-IR fine structure line emission from dusty star-forming galaxies at Cosmic Noon. At these redshift, these lines can be observed from ground-based telescopes at exceptional sites. To pursue this science, we build and use the second generation Redshift(z) and Early Universe Spectrometer (ZEUS-2) at the Atacama Pathfinder Experiment (APEX) Telescope, a 12 m sub-mm quality dish that operates at a high site (at 5104 m) on the Atacama plateau in northern Chile. The plateau and nearby high peaks are the best developed sub-millimeter sites on earth at mid latitudes - regions in Antarctica are likely better still but they are logistically challenged. At these Chilean sites, we can regularly expect the precipitable water vapor to drop below 1 mm, opening up the short sub-mm telluric windows with significant transmission that allows the radiation to pass through the atmosphere and reach our instruments. With our observing program we are building up a suite of observations of far-IR fine structure lines of C, N and O, that are redshifted into these sub-mm bands. These observations form the basis of this work presented in this thesis and will provide important constraints on the physical and chemical conditions of the ISM in dusty galaxies during the epoch of galaxy assembly.

CHAPTER 2
COMPLETING ZEUS-2: INTEGRATION OF THE 200/645 μm TES
BOLOMETER ARRAY AND DEPLOYMENT AT APEX

2.1 The Second Generation Redshift(z) and Early Universe Spectrometer (ZEUS-2)

The second generation Redshift and Early Universe Spectrometer (ZEUS-2) is a high-throughput, long-slit, moderate resolution ($\frac{\lambda}{\Delta\lambda}=R\sim 1000$), direct-detection, sub-millimeter grating spectrometer. The focal plane of ZEUS-2 is populated with two arrays of transition-edge-sensed bolometer pixels that are illuminated by light passing through a long-slit (multiple spatial positions on the sky projected across the array) and spectrally dispersed by an echelle grating (multiple spectral channels at each spatial position along the array). The targeted spectral lines are faint and, for unresolved observations of distant galaxies with a single dish sub-mm/mm telescope, are expected to be several hundred km s^{-1} wide. Therefore a spectral resolution of $\Delta v\sim 300 \text{ km s}^{-1}$ provides a good balance between the high sensitivity required to detect these faint lines, and the finite number of detectors in the spectral domain so as to achieve sufficiently large instantaneous spectral bandwidth.

The predecessor of ZEUS-2, ZEUS was a highly successful 2-band (350 and 450 μm) echelle grating spectrometer (e.g., [Ferkinhoff et al., 2010, 2011](#), [Hailey-Dunsheath, 2009](#), [Hailey-Dunsheath et al., 2010, 2008](#), [Stacey et al., 2010](#)). ZEUS was deployed on the Caltech Sub-millimeter Observatory (CSO) on Mauna Kea. ZEUS-2 is a long slit version of ZEUS, where the 2-dimensional formats of our

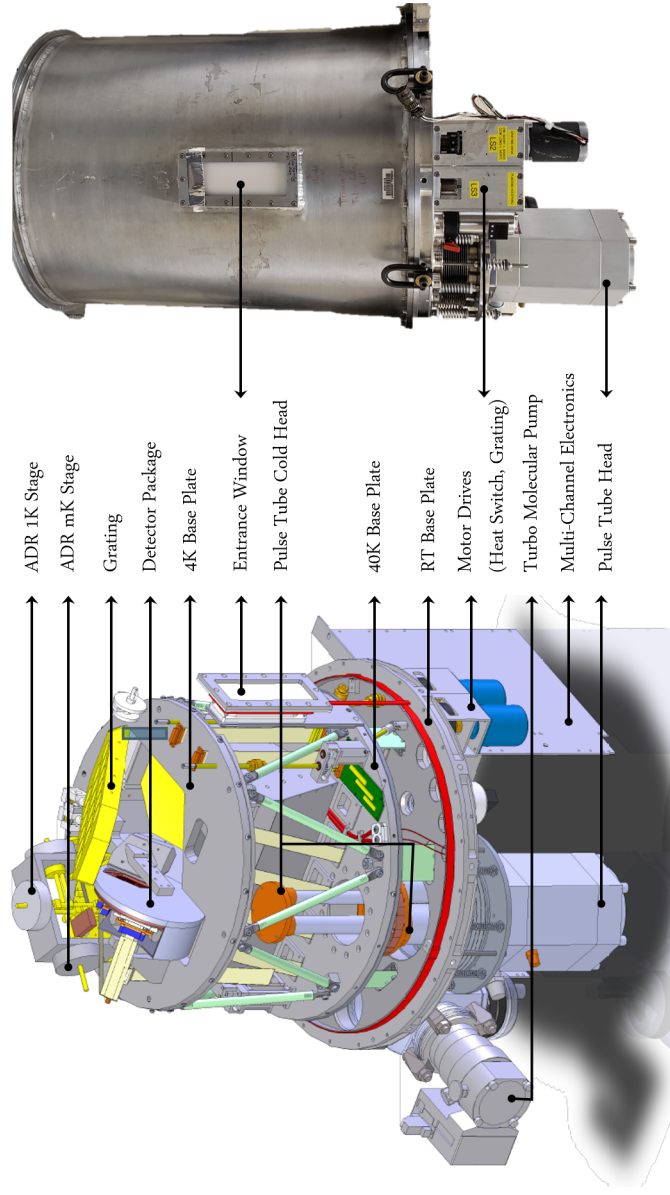


Figure 2.1 An overview of the ZEUS-2 Cryostat identifying the various subsystems: **Cryogenics**— Turbo molecular pump to achieve ultra-low vacuum (10^{-8} mbar). Pulse-tube cold head to cool the instrument to 4 K with a guard stage at 40 K. Adiabatic demagnetization refrigerator to cool the detector package down to 100 mK with a guard stage at 1 K. **Mechanical**— Support structure that keeps the various temperature stages isolated but accommodate differential contraction during thermal cycling of the instrument. Motor drives for operating the heat switches and grating. **Optics**— Most of the cold optics are hidden on the 4 K stage to minimize their exposure to ambient radiation (see Figure 2.3). The entrance window through which light enters the instrument and the grating that disperses the light on to the detectors are visible. **Electronics**— Multi-Channel Electronics instrument rack is mounted directly on the cryostat, it is used to bias and optimally tune the SQUID amplifiers and, bias and readout the detectors arrays. The ADR creates a large magnetic field but the SQUID amplifiers are extremely sensitive to magnetic fields, hence the detector package is enclosed in a 4K Amumetal shell placed inside a Niobium box to shield the readout components from magnetic interference. Just inside the vacuum shell of the cryostat is a cylindrical shell (not seen here) made of high-permeability Amumetal (proprietary alloy by Amuneal Manufacturing Corp.) that provides a layer of shielding from any external magnetic fields.

detector arrays permit simultaneous operation in up to 4 bands with up to 9 spatial positions per spectral row. ZEUS-2 was designed to be deployable on the CSO, James Clark Maxwell Telescope (JCMT) (on Mauna Kea) and the Atacama Pathfinder Experiment (APEX) telescope in northern Chile. Design work for ZEUS-2 began in 2009 (Ferkinhoff et al., 2012, Parshley et al., 2012) and the instrument achieved first light on APEX in 2013 (Ferkinhoff et al., 2014). The first light version of ZEUS-2 was used three more times at APEX and is described in C. Ferkinhoff's PhD thesis (Ferkinhoff, 2014). I took over for the well-being of the instrument starting late 2013 after it arrived back from the APEX. The material described in Section 2.1 and 2.2 provides important background information essential to describe the workings of the instrument. I have specifically mentioned my contributions to the existing system that have improved the characterization and operational capabilities of the instrument. In Section 2.2 and 2.3, I describe in detail the work I did to design a new grating for ZEUS-2 and install a new detector array that adds significantly to the scientific capabilities of the instrument. All mechanical drawings and renderings that are reproduced here (with sincere thanks) were created by Steve Parshley.

The new work described within this thesis includes the design and integration of a new optimized grating, operational improvements and deployment of the $400\ \mu\text{m}$ array at the APEX telescope, and most importantly, the integration of a new $215/645\ \mu\text{m}$ array. I also discuss the new discoveries we have made using ZEUS-2, in particular, exploring the origin of the [O III] $88\ \mu\text{m}$ line in dusty star-forming galaxies at Cosmic Noon. It requires 35 eV to create the O^{++} ion from O^+ , and therefore requires the presence of a hard ionizing source, typically upper main sequence O-stars or potentially an active galactic nuclei. Both these sources are likely related to violent feedback mechanisms that reg-

ulate star-formation activity in these early galaxies. The [O III] line provides a promising avenue to study these short-lived periods of activity that play an important role in building up the stellar masses of galaxies and growing their central super-massive black hole, under conditions that are unlike any that we find in the local Universe.

Our group's heritage is that of far-infrared and sub-mm instrumentation, with instruments like the Kuiper Wide-field Infrared Camera (KWIC) (Latvakoski, 1997, Stacey et al., 1993), the South Pole Imaging Fabry-Perot Interferometer (SPIFI) (Bradford et al., 2002, Oberst, 2009), and the first-generation Redshift and Early Universe Spectrometer (ZEUS) (Hailey-Dunsheath, 2009). The primary science instrument in operation today is ZEUS-2 that provides access to the short sub-mm windows starting $\sim 195 \mu\text{m}$ and up to $650 \mu\text{m}$. In the near future, our group is providing mission critical Fabry-Perot interferometers for the High-Resolution Mid Infrared Spectrometer (HIRMES) for the SOFIA airborne observatory that runs from $25\text{-}122 \mu\text{m}$ (Douthit et al., 2018). We are also developing the Era of Re-ionization Camera and Spectrometer (EoRSpec) for the upcoming CCAT-prime telescope, a 6-m survey telescope with a large instantaneous field-of-view that enables a revolutionary jump forward in sub-mm instruments with a focal plane populated by $10^4\text{-}10^5$ pixels (Stacey et al., 2018).

To our knowledge, ZEUS-2 is the only operational spectrometer at $200 \mu\text{m}$ that has the sensitivity to detect extragalactic line emission. It bridges the gap in spectroscopic coverage between currently available facilities, like SOFIA and ALMA, until a future space far-IR/sub-mm mission comes along. Even in the 450 and $350 \mu\text{m}$ range, ZEUS-2 offers significantly better sensitivity

for broad line detection than heterodyne instruments operating at the same frequencies. On the APEX telescope ZEUS-2 provides an exploratory platform for observations of spatially integrated line luminosities, before attempting to invest high pressure top quartile weather time with ALMA. As designed, ZEUS-2 on APEX is as or up to $3\times$ more sensitive than the SPIRE spectrometer on-board the Herschel Space Observatory, depending on the operating wavelength and atmospheric conditions. For the case of observations of nearby galaxies, ZEUS-2 on APEX offers a factor of two higher spatial resolution. ZEUS-2 offers significant synergies with ALMA. As a reflection of how difficult it is to operate an interferometer at high frequencies with rapidly changing atmospheric conditions, at the end of more than 5 years of operation with ALMA, Bands 9 and 10 (450 and 350 μm atmospheric windows) remain as 'non-standard' modes. Due to the challenges, ZEUS-2 will continue to pave the way for these high frequency observations with ALMA, in order to justify the investment of time that is not only highly competitive, but also scarce.

I will overview the major subsystems that make the second generation Redshift and Early Universe Spectrometer (ZEUS-2). My thesis work focused on helping deploy ZEUS-2 at the Atacama Pathfinder Experiment (APEX) telescope in northern Chile and perform observations of astrophysically important ions of the most abundant metals in the Universe – carbon, nitrogen and, oxygen, in galaxies within the first few billion years of the Big Bang. ZEUS-2 was developed and assembled in house at Cornell University by a group of astronomers, engineers, graduate students with significant exposure to undergraduate students with practical lab and instrumentation experience.

2.1.1 A Dry Cryostat

Dual Stage Pulse Tube Cooler: Cryogen-free cooling to 4 K

The cryostat is cooled using a dual stage, pulse tube cooler, PT407-RM, sold by Cryomech Inc. The pulse tube cooler circulates helium gas through the cryostat to extract heat out of it (at ~ 1.4 Hz). The vibration that can be produced from the operation of the cryo-cooler can contribute significantly to the heat load on the milli-Kelvin stage and be detrimental to the detection of faint signals from the science sources. To minimize the coupling of vibrations from the pulse tube cryo-cooler to the cryostat, we isolate the cold head from the cryostat using spring bellows and use a remote motor to run the pulse tube mechanism. The cold head is mounted directly on the cryostat and the motor is connected to it through a flexible line. In the lab, we isolate the motor from the mechanical mount of the cryostat, but due to the restricted space available at the telescope, we weakly support it by the mechanical structure on which the cryostat rests in the telescope cabin. The remote motor is connected to a CP2870 helium compressor, that requires closed-loop chilled coolant supply. The heat exchanger inside the compressor, through which the helium gas circulates and deposits heat extracted from the cryostat, is cooled with water in the lab and glycol at the APEX telescope. The system is rated to provide 0.6 W cooling power at 4.2 K with 22 W at 55K.

All the optics inside ZEUS-2, readout electronics and the Adiabatic Demagnetization Refrigerator (ADR) that cools the detector to milli-Kelvin temperatures, are mounted on the 4 K stage. It is important to maximize the cooling power, hence minimize the temperature of this stage, since the lower temper-

ature cooling stages “launch” off the “4 K” stage and these lower temperature stages have significantly lower cooling power than the 4 K stage. After the integration of the full set of 4 K readout electronics, house-keeping sensing wires and fully populating the detector package with the 215/645 μm array along with readout cables, we spent a significant effort to properly sink elements, lower background with appropriate filtering, grounding wires, etc. As a net result, we currently achieve stable operating temperatures of under 45 K on the base plate of the first temperature stage and under 3 K on the base plate of the second temperature stage. These temperatures have aided in lowering the starting heat load on the ADR to reach and maintain milli-Kelvin operating temperature for the detector package for an extended period of time.

Dual Stage Adiabatic Demagnetization Refrigerator : 1 K and 100 mK Stages

Dictated by the requirement for the detectors to be background limited and to have sufficient ‘safety factor’ against saturation, the transition temperature for the TES bolometers is ~ 170 mK above absolute zero. The estimated noise equivalent power (NEP) contribution due to fluctuations across the thermal link is a function of the temperature and the thermal conductance of the link (G) as, $\text{NEP}_G = (4 kT_C^2 G)^{1/2} \sim 1.1 \times 10^{-17} \text{W}/\sqrt{\text{Hz}}$ for $T_C = 170$ mK and $G = 80$ pW/K for the 400 μm array. This is at least a factor of 3 smaller than the expected noise due to the background that high opacity atmosphere presents to the detectors while observing and allows ZEUS-2 to remain background limited.

In order to operate the bolometers under optical loading from the sky, we need to cool the detectors below the transition temperature and then externally bias them to bring them to an operating point along the the transition between

their superconducting and normal state. We use a dual stage Adiabatic Demagnetization Refrigerator (ADR) from Janis Research Company LLC., that allows us to cool down the detector to <100 mK. The ADR contains a current carrying superconducting coil that creates a strong (4 Tesla) magnetic field and 2 paramagnetic “salt” pills, containing gadolinium gallium garnet (GGG) and ferric ammonium alum (FAA) that provide a 1 K intermediate stage (3rd temperature stage) and a 100 milli-Kelvin bath for the detector package (4th temperature stage), respectively.

The ADR salt pill is a cold sink with finite cooling capacity so that it must be periodically recycled. To start a cooling cycle, we apply a large, external magnetic field that helps align the magnetic domains within the salt pills, thereby reducing the net entropy of the system. After magnetization, the system is allowed to cool by the pulse tube and rid of any excess heat of magnetization. Once nearing equilibrium, the heat switch between the 4 K stage and the ADR is opened, isolating the ADR so that the detector package is the only remaining connection to the ADR. At this point, the current is withdrawn adiabatically from the ADR coil, removing the magnetic field. As the field is removed the magnetic domains in the salt pills want to reshuffle and the only place where they can withdraw the heat from is the detector package. The energy required to increase the entropy of the salt pills is drawn from the detector package, thereby cooling it down.

Soon after we procured the ADR, we made a test cool-down to measure the cooling capacity of the salt pills. Under no load (no detector package connected to the ADR), the mK salt-pill could cool down to ~ 68 mK and remain below 100 mK for 22-24 hours. Currently in the lab, with the completed ZEUS-2 detec-

tor package, we measure a minimum temperature of $\sim 91-94$ mK on the salt pill and $\sim 97-99$ mK on the detector package. I have identified a notable anomaly upon first opening the heat switch before starting the demagnetization of the ADR. It is evident that an extra bit of heat is released that warms up the ADR pills and the detector package. The reason for this is unclear, but I speculate that it is potentially due to the physical movement of some components of the ADR mount structure that might be relaxed when the heat switch is opened after fully magnetizing the ADR. If we close the heat switch and allow this extra heat to dissipate before demagnetizing the ADR, it results in a net gain of $\sim 5-6$ hours of hold time when operating the detector at 130 mK.

For the ADR cycle, based on the lab tests of multiple ADR cycles, I found it best to ramp the current in the ADR coil from 0 to 9 A in about ~ 40 minutes, with a ramp rate that is between 3-7 mA/sec (specification from manufacturer for the maximum ramp rate is 9 mA/sec) to magnetize the salt pills. It is important to allow the mK salt pill to cool down below 3.6 K before opening the heat switch to release the excess heat followed by closing the heat switch to allow the detector package to cool back down and approach steady state temperature ($\simeq 3.4$ K). In a typical ADR cycle, it takes roughly 4 hours from the start of putting current in the coil to reach this point. We can now open the ADR heat switch to isolate the detector package and the ADR from the 4 K stage and draw the current out from the coil slowly (adiabatically, 1.5-2 mA/sec). Withdrawing the current takes about 80-100 minutes and it is best to start servoing our magnet current PID control loop to maintain the detector package at the desired temperature as soon as the current is completely withdrawn from the ADR. In total, an ADR cycle takes roughly 6 hours from the start of energizing the coil to when we can start servoing the detector package.

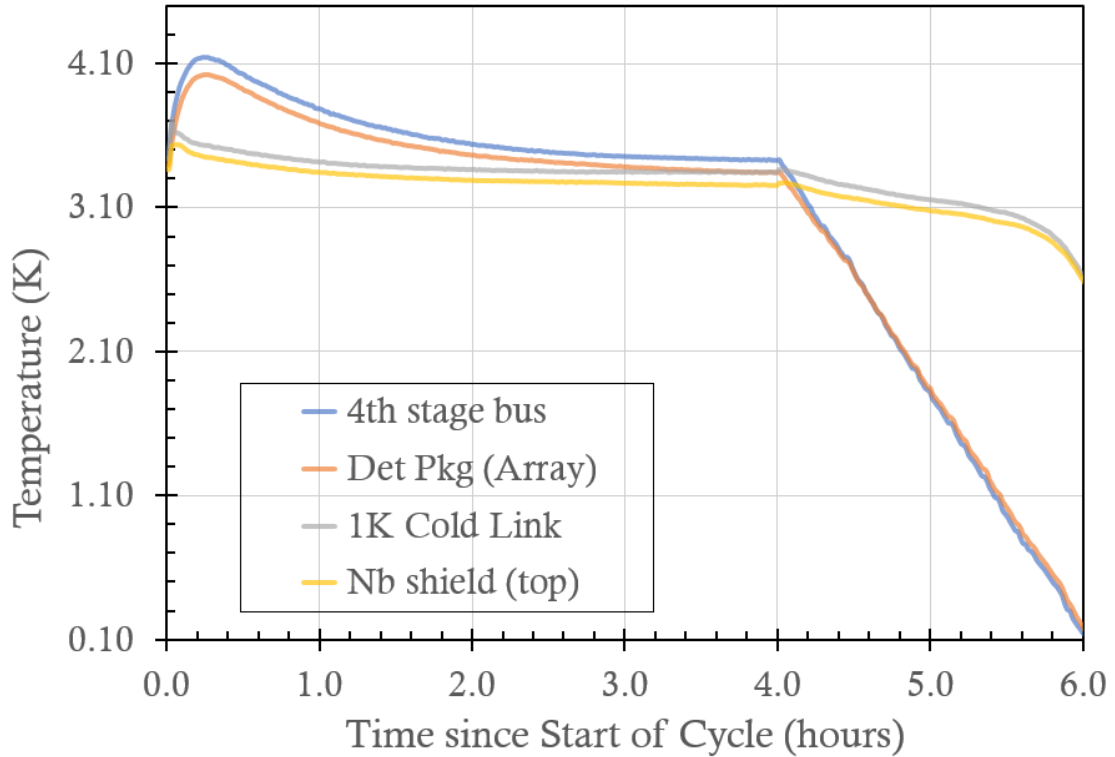


Figure 2.2 Temperature on various sensors on the 1K and mK stages from the start of magnetizing the ADR magnet coil to the end of demagnetization and just before starting the mK operations.

By starting the servo soon after the current in the ADR reaches zero we maximize the cooling power of the ADR cycle. The ADR mK salt pill keeps cooling down slowly for another 2-2.4 hours after the current has been withdrawn. As a result, the PID current in the servo typically increases to 13.5 A from ~ 10 A at the very start of the servo. By the time ~ 2 A of current is left in the PID servo, the ADR has almost exhausted its cooling capacity and it is difficult to maintain the detector temperature stably for more than 40 minutes. In total, the time for which we can hold the temperature of the full detector package, under no load, stable at 130 mK in the lab is currently ~ 18 hours.

An electronically controlled relay, that chooses between a direct path and a current dividing circuit, is used to switch between an ADR cycle and servoing

on the detector package and allow remote operations. The current dividing circuit is used to regulate the current that goes into the ADR based on an input from the PID servo on the detector package temperature. At first, we were limited by this circuit that only allowed a maximum of ~ 100 mA to reach the ADR during the servo. I have since installed a new relay rated at 15 A, and modified the current splitting circuit to allow up to 150 mA to be sent to the ADR. This in turn affords us a higher starting current in the ADR at the start of observing and increases the resolution with which a change is made in the ADR current based on an input from the PID controller to keep the operating temperature stable. To give a sense of the improvement we have achieved with the above changes, when I started work on ZEUS-2, the detector package with only the $400 \mu\text{m}$ array and cables, under no extra heat load, could operate at 120 mK for ~ 8 -10 hours. With all the improvements since, I was able to increase the hold time at 120 mK for the same system to well in excess of 30 hours.

With the implementation of the new array, we have more than doubled the total number of wires going into the mK stage and increased the mass that is at the mK temperature stage. With the new system, in the lab we achieve a hold time of ~ 18 hours operating at 130 mK, under no load. I have identified two avenues for improvement on this hold time value, in particular, one concerning the mount and support structure for the ADR to make it less susceptible to vibrations and, a second concerning the thickness of the wire used for the various readout cables that will reduce the heat load on the mK stage. Addressing these issues will gain us extra operating time at which we can hold the temperature of the detector stable, potentially by as much as 4-6 hours. The effect of vibrations is more pronounced at the telescope – we found that broadband vibrations from a Gifford-McMahon (GM) cryo-cooler for another instrument were being trans-

ferred to the ZEUS-2 mount through the structure in the instrument cabin. The mechanical motion of objects dissipate heat that appears as an extra heat load in the system. The isolation mechanism for the detector package inside the dewar is made of stretched Kevlar and is susceptible to vibrations. The vibrations also affect the stability with which the PID servo can maintain the temperature of the detector. In the lab, the servo stability is $\pm 50 \mu\text{K}$ but worsens by $3\text{-}8\times$ on the telescope. During our last observing run at APEX in 2016, due to a power loss event due to generator malfunction, we were able to verify and measure the affect of the vibration environment that we were otherwise unable to replicate in the lab. While the GM cryo-cooler was turned off, with the detector operating at 130 mK, we were able to achieve a PID servo stability of $\pm 80 \mu\text{K}$ and a total observing time of 14 hours. This was approximately equal to what we can achieve in the lab. With the vibrations present, the total hold time of the ZEUS-2 system while observing (detector and readout biased) was reduced to about 10 hours.

2.1.2 Detectors and Read out components

The transition edge sensed (TES) bolometer detector array and read-out components, including the superconducting quantum interference devices (SQUID) that act as multiplexers and amplifiers to readout the detectors, were fabricated by the Quantum Sensors Group at National Institute of Standards and Technology in Boulder, Colorado.

The detectors in ZEUS-2 are spread over two physical arrays of Transition-edge sensed bolometers. The super-conducting sensors are created with a bi-layer of Molybdenum-Copper (MoCu). The transition temperature is adjusted

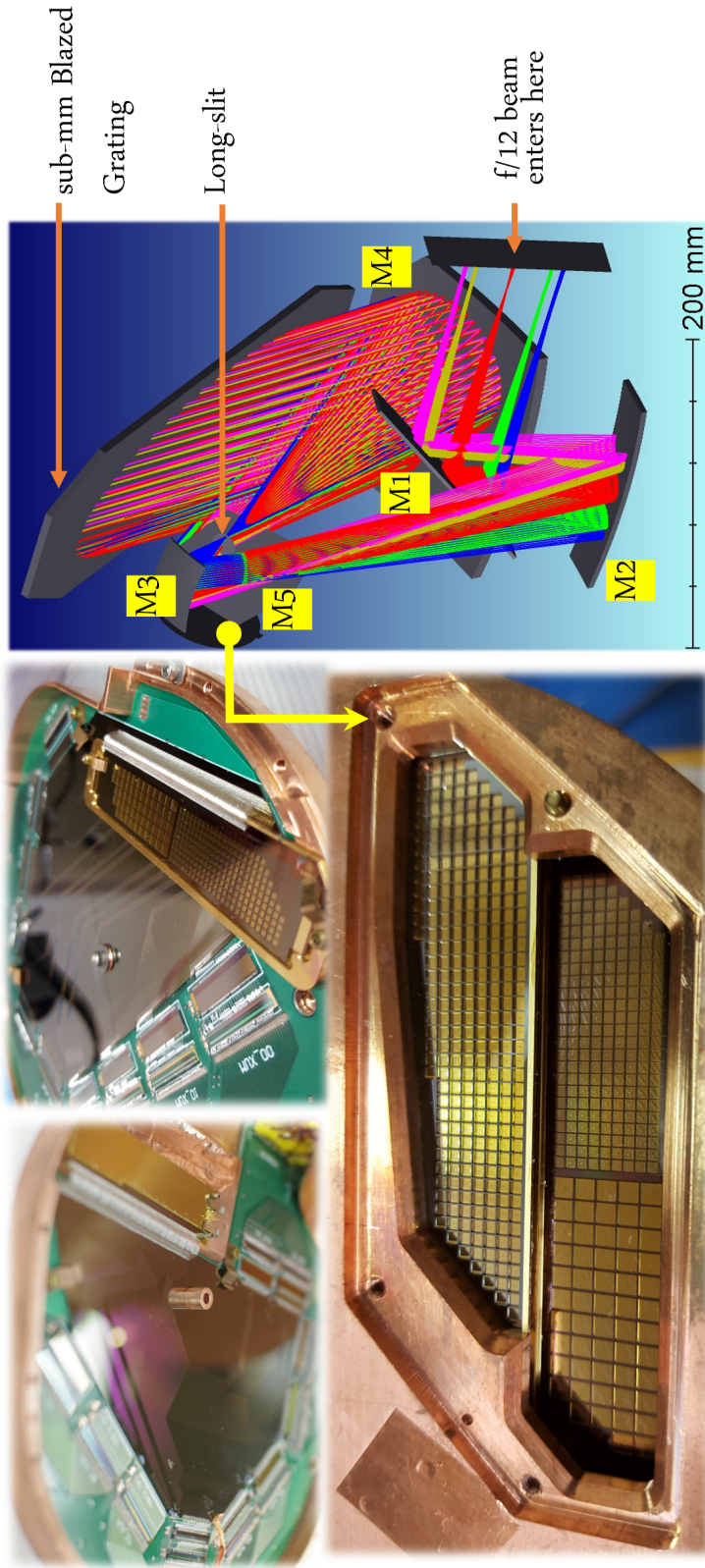


Figure 2.3 (right) An overview of the cold optics inside ZEUUS-2 from the entrance window up to the focal plane. A $f/12$ beam enters the instrument through the entrance window and reaches a focus just behind the window. Various long-pass and scatter filters are placed at 40 K stage to limit the radiation reaching the 4 K stage. Entering the 4 K stage, the diverging beam is reflected by M1 on to the collimating mirror M2. A Lyot stop with a long-pass filter at the pupil is used to limit unwanted thermal radiation from off-axis directions. The collimated beam then hits M3 that focuses it onto the entrance slit of the spectrometer. From here the diverging beam illuminates the right half of M4 that creates a collimated beam incident on the grating. The grating disperses the light and reflects it back to the left side of M4 from where it is reflected and onto the pick-off mirror, M5. M5 is a flat mirror that directs the dispersed light to the focal plane where it is incident on the bandpass filters in front of the detector arrays. These filters are used to select which order of the grating is allowed to pass through and onto the detector arrays. (left) View of the individual detector arrays along with the readout components and from top without the bandpass filters.

as per requirements by changing the relative thickness of the normal (Cu) and superconducting (Mo) layers. Each array is equipped with a $n\lambda/4$ ($n = 1$ or 3) back-short optimized for maximizing detector quantum efficiency for operations at 215 , $400 \mu\text{m}$ and $645 \mu\text{m}$. The back-short allows the detector arrays to achieve greater than 90% detector quantum efficiency at the band center. In the current configuration, the $400 \mu\text{m}$ array is operated with the left half covered with a $350 \mu\text{m}$ bandpass filter and the right half covered by a $450\text{-}\mu\text{m}$ bandpass filter. This effectively shortens the instantaneous spectral coverage in each bands to a fractional bandwidth $\Delta\nu/\nu \sim 2\%$. Each of the telluric windows can be covered by moving the grating to from shallow to steep angle ($\sim 54\text{-}74^\circ$, 19.8° range). This configuration provides us coverage on the short(long) wavelength end of the tuning range provided by tilting the grating in the 5^{th} (4^{th}) order. We can reverse the coverage, if dictated by science requirements, by swapping the location of the bandpass filters.

The multi-channel electronics that provide the interface between readout components within the cryostat and software to bias and tune the SQUID amplifiers and, bias and read out the detector arrays, was procured from Prof. Mark Halpern's group at the University of British Columbia in Vancouver, Canada. A detailed description of its hardware components, firmware and software operations can be found at the [MCE Wiki](#), and a description of the time division multiplexing scheme that is used to read out the detectors is described in [Niemack et al. \(2008\)](#).

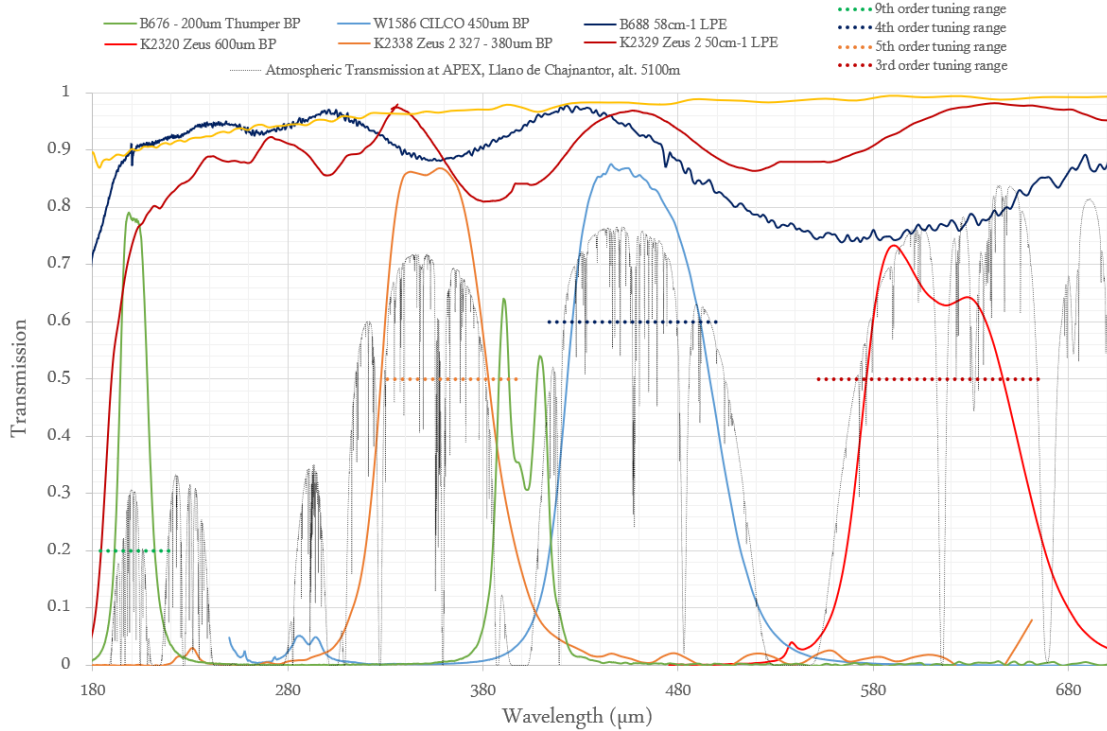


Figure 2.4 Transmission plots of all the filters currently in use inside ZEUS-2. (Yellow) Infrared filter installed just behind the entrance window to filter the peak of the ambient temperature radiation (C15, LPF 500 cm^{-1}). (Dark Blue) Long pass filter used for the $215/645\text{ }\mu\text{m}$ detector array (B688, LPF 58 cm^{-1}). (Dark Red) Long pass filter used for the $350/450\text{ }\mu\text{m}$ detector array (K2329, LPF 50 cm^{-1}). (Green) Bandpass filter used for the $200\text{ }\mu\text{m}$ detectors (B676 Thumper, BPF), (Orange) Bandpass filter used for the $350\text{ }\mu\text{m}$ detectors (K2338, BPF), (Blue) Bandpass filter used for the $450\text{ }\mu\text{m}$ detectors (W1586 CILCO, BPF), (Red) Bandpass filter used for the $645\text{ }\mu\text{m}$ detectors (K2330, BPF). The atmospheric transmission corresponding to rather exceptional conditions with $\text{PWV}=0.25\text{ mm}$ for the APEX site is shown as a dotted black line.

2.1.3 Optical Filtration

As bolometers are sensitive to a broad spectrum of incident light, it is essential to ensure that the light entering the instrument is properly filtered and only the relevant frequencies are allowed to reach the detector. The photon background at sub-mm wavelengths are quite small, $\sim 1\text{ pW}$, therefore we have carefully chosen and installed multiple filters at different points along the optical path inside

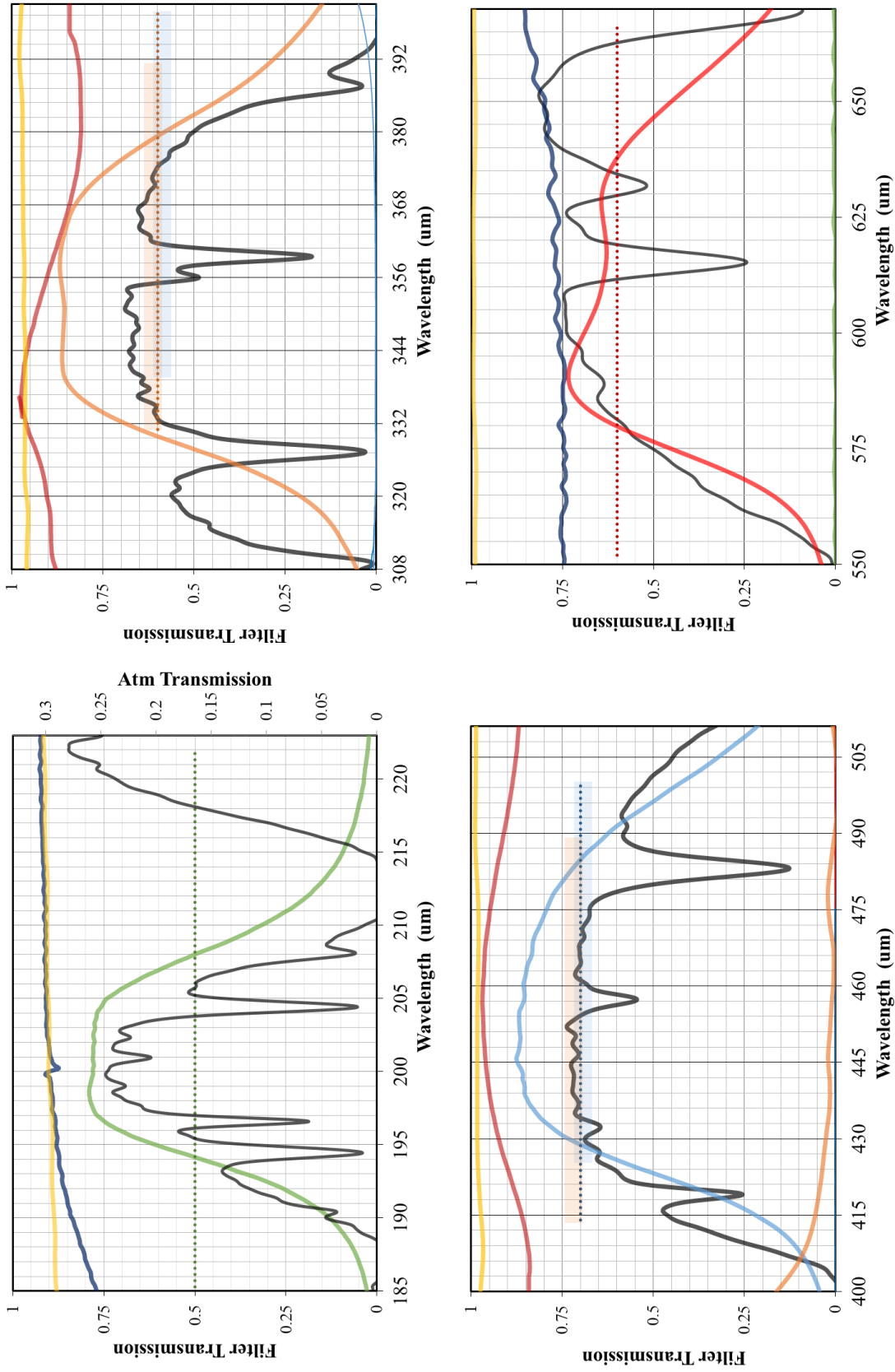


Figure 2.5 Atmospheric transmission (in black), with PWV=0.25 mm, identifying the telluric windows along with the filter transmission relevant to individual grating orders, 9th order (top-left), 5th order (top-right), 4th order (bottom-left), 3rd order (bottom-right) (same colors as Figure 2.4).

the cryostat to avoid spectral leakage and ensure minimum background power reaching beyond the entrance window. These filters were manufactured for us by Prof. Carole Tucker and Peter Ade's group and QMC Instruments Inc.

Light enters the instrument through a rectangular high-density polyethylene (HDPE) window. We were previously using a cold HDPE cover immediately inside the window, intended to act as an absorbing filter in combination with either a Quartz/Zitex filter at 4 K, for infrared radiation coming through the entrance window. The filter is thermally connected to the 45 K temperature stage. I have replaced it with new metal mesh infrared 'heat' filter (QMC Instruments ID C15). The HDPE filter had $\sim 73, 85, 87$ and 88% transmission at $200, 350, 450, 620 \mu\text{m}$ respectively. The new IR filter has greater than 90% transmission at all wavelengths of interest for science operations ($>190 \mu\text{m}$). All objects in the surroundings of the instrument can be approximated as a black body at ambient temperature (~ 288 K inside the telescope cabin, total net emissivity ranging from $\sim 20\%$ to unity) and therefore the radiation from them peaks near $10 \mu\text{m}$. Using this IR filter, we can block and reflect out more than 90% of all radiation between $10\text{-}13 \mu\text{m}$, with a maximum of 97% blocking around $12 \mu\text{m}$. With this new 'heat' filter in place, I was able to significantly reduce the heat load on the 4 K stage. More work remains to be done to quantify if the Zitex filter currently installed before the cold optics elements inside ZEUS-2 at 4 K is redundant given the passband of the new IR filter. Transmission of Zitex is $\sim 75\text{-}95\%$ between 190 and $500 \mu\text{m}$ (Benford et al., 1999). If found appropriate, removing the Zitex filter may be helpful to increase the throughput of the instrument by $15\text{-}25\%$ at shorter wavelengths. We also use an optical/near-IR scatter filter at the 45 K stage, that scatters light that passes through the IR filter into 4π steradians, out of the science beam where it is absorbed by black paint.

Table 2.1 Wavelength tuning range for all orders of interest accessible with the grating in ZEUS-2 and 50% transmission cut-off for currently installed bandpass filters

Grating Order	Grating Tuning Range (μm) ($\alpha=54-74^\circ$)	Bandpass Filter 50% cut-off (μm)	
		Short End	Long End
2	829-1000	—	—
3	552-667	576.0	646.3
4 (short)	414-490	423.4	496.2
4 (long)	425-500		
5 (short)	331-391	327.9	383.3
5 (long)	339-400		
6	276-333	—	—
8	207-250	—	—
9	184-222	194.1	208.0

I have also updated bandpass filters in front of the detectors arrays. These filters allow us to choose a specific order of the grating for observations with each detector array, reflecting back wavelengths from higher and lower orders of the echelle. These bandpass filters were chosen to maximize transmission over the tuning range of the grating in the 3rd, 4th, 5th and 9th orders. The tuning range is optimized to cover a large fraction of the corresponding telluric windows at 645, 450 and 350 and 200 μm . The 200 and 645 μm filters are brand new to the system installed in front of the new detector array. The 350 and 450 μm filters are replacements for the previous filters we used, that had slightly narrower bandpass.

The wider bandpass offered by the updated 350 μm filter created a potential spectral leakage issue at the long-wavelength end of the 350 μm telluric window (due to overlapping 5th and 6th order of the echelle) during our 2016 observing run. This can be easily mitigated by changing back to the original 350 μm bandpass filter that has a narrower bandpass, from 333-385 μm , and

only marginally lower peak transmission of 71% (as compared to 77% for the new filter).

2.2 Warm Optics

In the lab, ZEUS-2 is operated in stand-alone mode with a mechanically controlled chopper blade directly in front of the cryostat entrance window. Depending on the test scenario, we illuminate the entrance window with a cold-load made of a liquid nitrogen bath at 77 K, or glass hot-plate that is heated by a resistor patch that can be regulated with the help of a rheostat and can be operated stably between room temperature and up to 350 K.

For spectral calibration purposes, we can install a gas-cell between the chopper and the hot/cold load. The gas-cell has PTFE windows on each side that allow high frequency radiation to pass through and illuminates multiple spatial positions simultaneously on the detector array.

I also built a beam mapper (with help from Jeremy Hodis), using stepper motors and variable size apertures, to map the f-cone of the pixels projected through the cold optics at a distance and the coupling to an extended source. The effective $f/\#$ of the light through the entrance window is $f/12$. The stepper motors allow accurate and repeatable measurements with a minimum step size of $\Delta L=6$ mm along both axis.

At the APEX telescope, ZEUS-2 resides in the A-cabin which is at one of the two Nasmyth foci. The light received by the telescope, is reflected into the Cassegrain cabin from the secondary mirror. It goes through four reflecting

Warm Fore-Optics for APEX - ZEUS-2 Interface

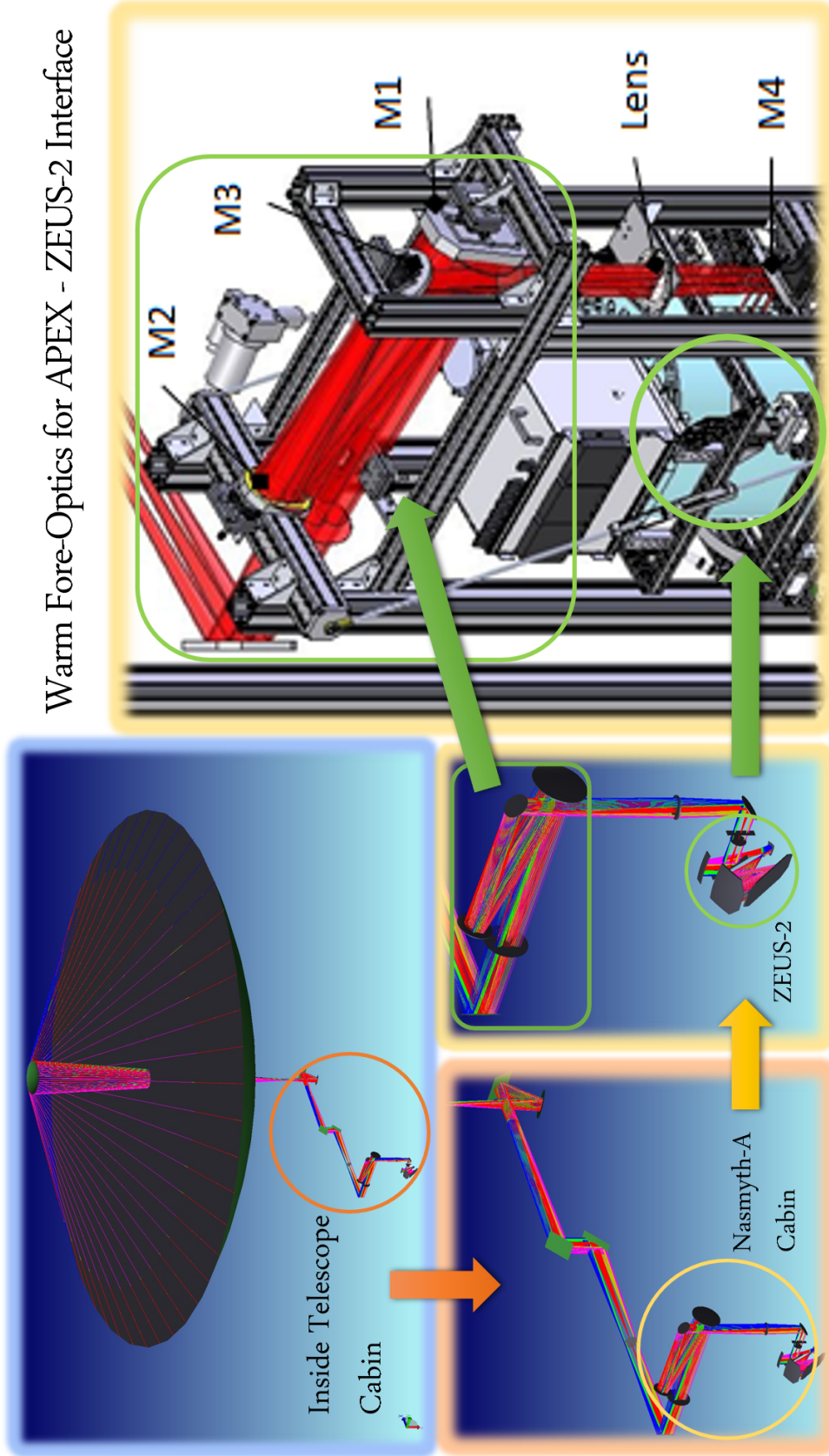


Figure 2.6 An overview of the warm fore-optics used at APEX to couple the telescope beam to ZEUS-2. See text for further details of how the light from the telescope is coupled to ZEUS-2

elements to guide it through an optical tube to one of the two instrument cabins at the Nasmyth focus. ZEUS-2 is located in the Nasmyth-A cabin, where a pick-up mirror at the end of the optical tube receives the light from the Cassegrain cabin and redirects it to one of the three available instrument positions. The beam coming from the telescope through the pick-up mirror is a $f/8$ beam which needs to be converted to a $f/12$ beam before it reaches the entrance window of ZEUS-2.

We use warm fore optics that consist of four mirrors and one HDPE lens, to receive the $f/8$ beam from the telescope, convert it to $f/12$ and direct it to the entrance window of the instrument. Including the primary dish of the telescope and the secondary reflector, the light is redirected through 11 reflecting surfaces and focused through one lens, before it finally reaches the entrance window of ZEUS-2. Initial alignment of the warm optics along with rough alignment of the cryostat entrance window is done with the help of a dual-beam laser mounted between the pick-up mirror and the ZEUS-2 fore optics. Detailed alignment of the beam with the f -cone of the detectors is done later, with the help of measurements using an Eccosorb foam pedal dipped in liquid nitrogen acting as a cold load, and a mask placed in the pupil plane located near the M3 mirror of the fore-optics. The f -cone calibration scheme was designed

2.3 Grating Optimization to tune Operational Range to Telluric Windows and Maximize Efficiency

The only component of the cold optics borrowed from the original ZEUS (ZEUS-1) instrument into ZEUS-2 was the reflecting grating used to disperse the light

before it reaches the detectors at the focal plane of the instrument. ZEUS-1 operated at 350- and 450 μm but the design for ZEUS-2 optimized the optics to allow for operations from ~ 200 to 850 μm with a focal plane allowing access to up to 155'' on sky. The long-slit allows up to 9 simultaneous spatial positions on the sky while keeping the overall volume of the cold optical elements minimal. The grating used in ZEUS-1 was ruled with a sawtooth pattern angled at $\tan^{-1}2 = 63.435^\circ$ (referred to as a R2 blaze) and a groove frequency of 1.008 grooves/mm (groove spacing, $d=992 \mu\text{m}$). The grating in ZEUS-1 could be operated at angles between 59° and 69° .

In ZEUS-2, the mount and the location of the grating allows it to cover a larger angle range, $\sim 17.6^\circ$ (vs 10° in ZEUS-1). At the shallow angle limit, the grating could potentially contact the magnetic shielding box for the detector arrays. After installing the second set of detector arrays and careful adjustment of the location where the principle beam hits the focal plane, we found that the grating angle range could be adjusted on both ends by an additional $\sim 1.1^\circ$. We were able to achieve this by adjusting the limit switches that used to initialize the grating position before operations. A note of caution, in case the principle beam is moved higher towards the 215/645 μm arrays in the future, one must take care to reduce the operating range of the grating to avoid any chance of collision with the detector package. The extended angle range over which the grating can be moved extends the total spectral coverage of the telluric windows. This is particularly useful in the 3^{rd} and the 5^{th} order of operations.

The groove spacing and blaze angle of the grating determine the grating efficiency at any given wavelength, i.e., the fraction of incident power that is diffracted into the desired order of operations. I calculated the grating efficiency

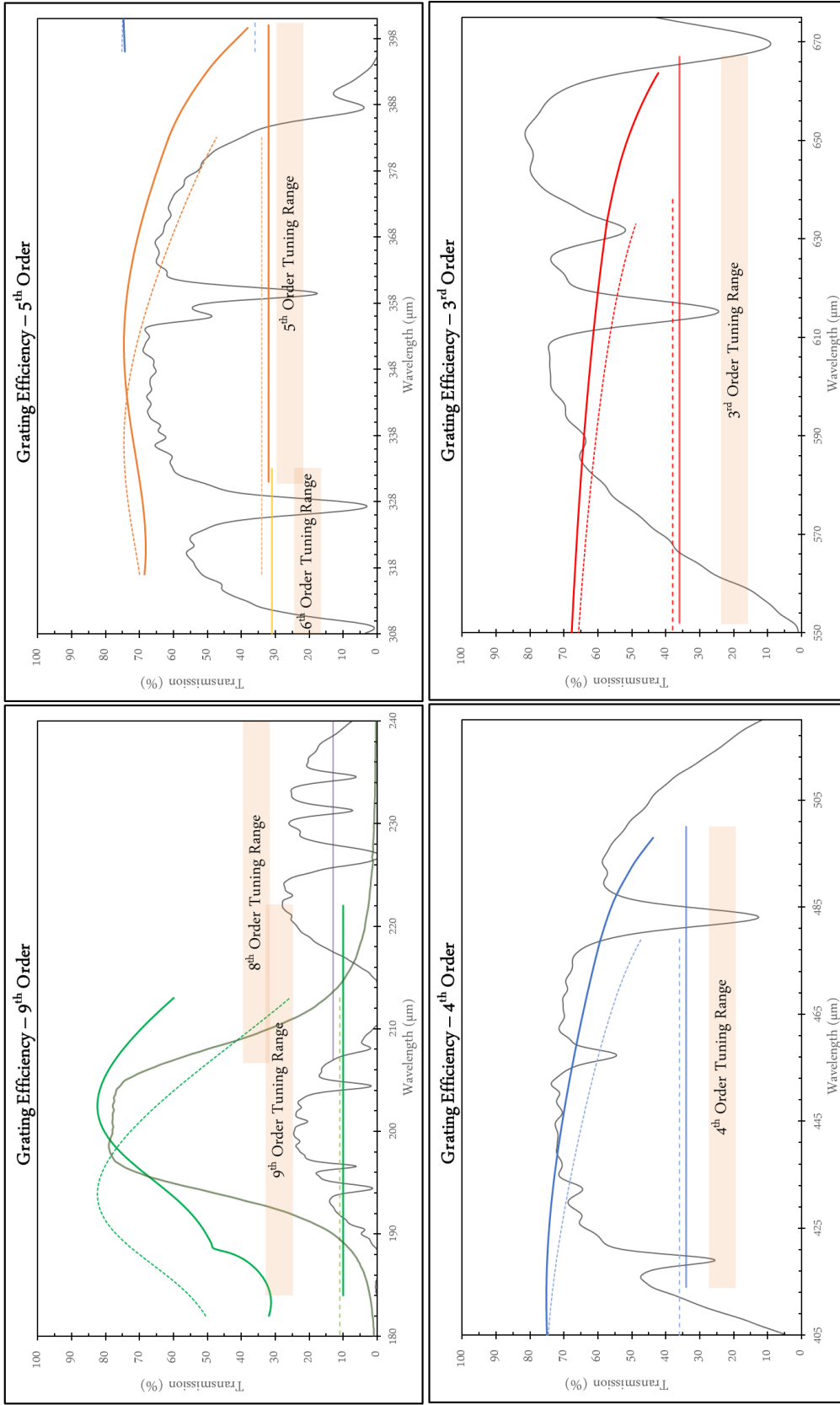


Figure 2.7 Grating efficiency of the individual grating orders for the new grating design used in ZEUS-2, Order 9 (top-left), Order 5 (top-right), Order 4 (bottom-left), Order 3 (bottom-right). We over plot the tuning range of each order and the neighboring orders where appropriate along with the grating efficiency and tuning range that was achieved by the original ZEUS grating in litrow mode (dotted lines) for comparison. Transmission in the telluric window corresponding to the order of the grating is shown in black. Transmission of the order sorting bandpass filter in the 9th order is also shown for reference.

for the ZEUS-1 grating using a specialized software, PC-Grate, that is designed for exact calculations of the efficiency based on input parameters for the grating design and illumination. I found, as expected that the grating efficiency drops fast for steep angles in each order. The groove spacing (frequency) primarily affects the wavelength for which the grating achieves peak efficiency in Littrow configuration. Keeping in mind the aim to expand the operations with this grating from 3rd to 9th order instead of focusing only on the 4th and 5th order of operations, I compared the grating efficiency envelopes to the telluric transmission windows, i.e., wavelengths at which observations are possible from the ground. I found that the efficiency envelope of the ZEUS-1 grating, with a groove frequency of 1.008/mm, did not match well to the telluric transmission windows around both, 200 μm and 645 μm .

I therefore undertook an exercise to calculate the appropriate grating design parameters that would adjust the efficiency envelope to provide coverage across the telluric windows and maximize the grating efficiency over the entire operating range. Due to the operating angles of the grating inside the cryostat, it was most reasonable to retain the R2 blaze, i.e., a blaze angle of 63.435°. We found that a modest \sim 4-5% increase in groove spacing (lower groove frequency), would allow us to position the grating efficiency envelope for all orders around the telluric transmission windows. The grating now have a groove spacing of 1036 μm (groove frequency of 0.96525/mm) and retains a blaze angle of 63.435. This grating was procured through funding sources available to our collaborators James Higdon and Sarah Higdon at Georgia Southern University. In the Littrow mode, the new design achieves upto 20% higher grating efficiency around 200 μm and the grating tuning range is better optimized to cover respective telluric windows in each of the operating orders of the grating.

2.4 Integration of the 215/645 μm TES Bolometer Array in ZEUS-2

The integration of the 215/645 μm array was my major contribution towards completing ZEUS-2. I summarize the most important steps of the integrations here and describe them in some detail.

- To reduce the total mass that would be cooled by the 100mK stage of the ADR, I worked (with Steve Parshley) to create a copper housing for the second half of the detector package that is 20% lighter than the original design without compromising any structural integrity. This lightweight design would help offset the increased heat load on the mK stage due to an increase in the number of wires required to readout the 257 (201+56) pixels on the new arrays.
- To enable the installation and precise registration of the Silicon fanout board on the 100mK package, I machined holes in the silicon fanout boards using a silicon machining setup in the department machine shop (with guidance from machinist at the Cornell High Energy Synchrotron Source laboratory and Chuck Henderson). These holes have to be very precisely drilled in order to avoid any issues due to thermal stresses as the instrument cools from from 300K to 4K and then the repeated cycling during observations between 4K and 100-140mK. The silicon board acts as an interface carrying superconducting signal and return lines (using Niobium) from the individual pixels on the detector arrays to the readout components. It is essential that this 'Si Fanout Board' be securely installed on a printed circuit board (PCB) placed inside a copper housing at the 100mK

stage.

- To create a robust, repeatable and time-saving process for wiring up detector arrays and readout electronics for large arrays, I worked with an external semiconductor packaging firm (Advotech Inc, AZ). I worked with them to implement an automated wire-bonding process for all connections, from the bond pads on the PCB to the read-out multiplexer chips, between the mux to the interface chip and the Si fanout board, and between the detector arrays to the Si fanout board, totaling over 4000 individual aluminum wire bonds.
- To achieve superior thermal uniformity across the array, I deposited a nano-plating of gold on the copper carrier for the detector arrays using a Thermal Evaporator at the Cornell Nano-fabrication Facility (CNF).
- I also designed a new addressing cable to double the number of read-out columns that can be addressed with the Multi-channel Electronics (MCE) (from 10 to 20). The cable was assembled by Universal Cryogenics (AZ) using a 0.0032" gauge wire which can be updated to a 0.002" wire to further reduce the heat load on the 100mK stage.
- I did extensive end-to-end testing of the signal path, from the detector package to the room temperature connectors feeding into the MCE box in order to identify signal lines that are problematic or otherwise can not be addressed using the MCE due to various reasons, like cabling, PCB design issues, etc.

—

The first task in order to assemble the new detector package was to take a critical look at all the components in the 'sandwich' design that allows us to host

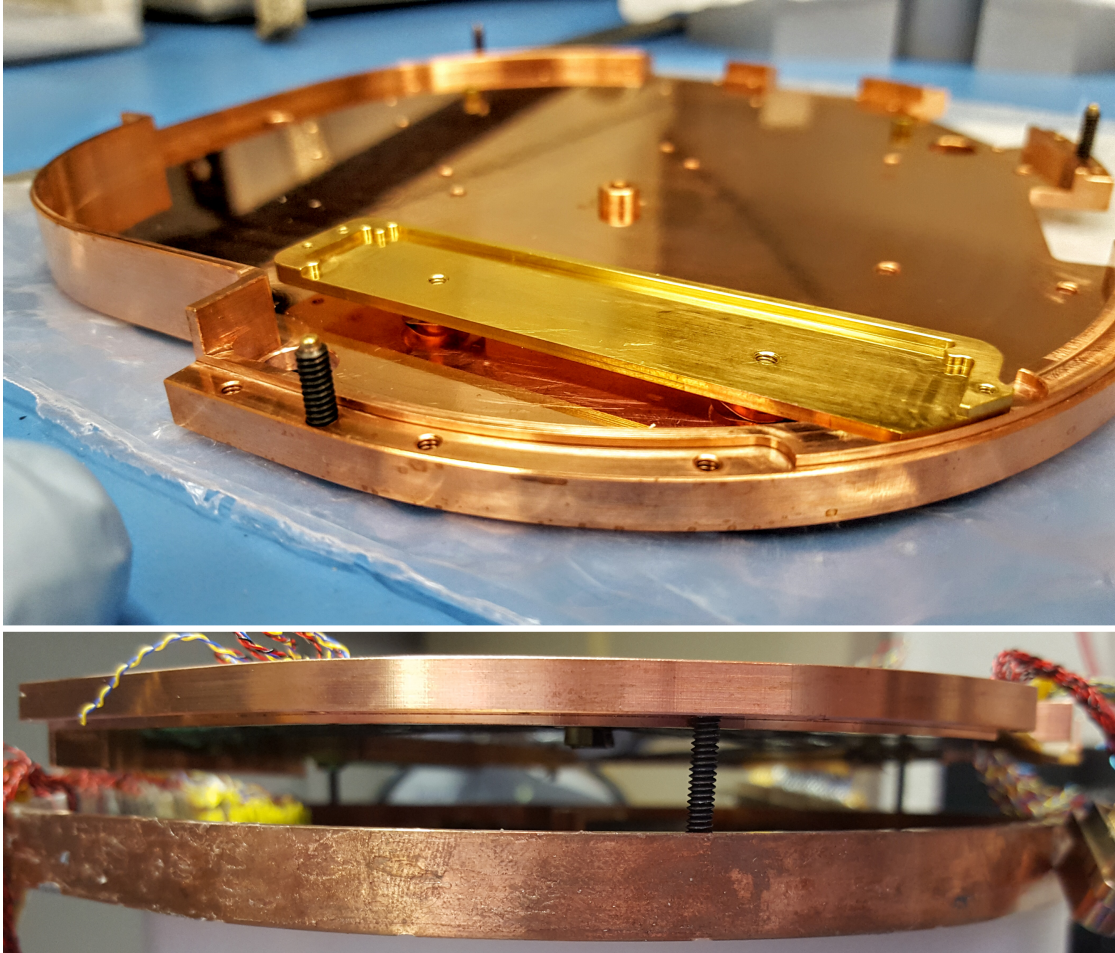


Figure 2.8 New thinned copper housing for the 215/645 μm array and readout components for ZEUS-2. The array carrier is gold plated to increase contact thermal conductance and minimize thermal gradients across the array. Three guide screws placed along the circumference are used to align the two halves of the detector package together, while allowing for safe handling and enough z-clearance to avoid accidents.

multiple detector arrays on ZEUS-2 keeping in mind the lessons learned from deployment of the 400 μm array. One of the primary concerns was to make sure that the hold time of the instrument does not reduce significantly. We could not change the location of the plane on which the detector array was installed as that set the optical alignment for the arrays. We decided that it would be feasible to thin the copper plate from the back side and reduce the mass of the copper package. I altered the length of the various screws, that hold the readout

MDM connectors and the cold finger on to the back plate, to ensure that they do not push on the PCB that hosts the electronics for the new array. This new copper housing for the 215/645 μm array replaced the previously used 'blank' copper piece to assemble the detector package and close the 400 μm array. I also designed a rigid, copper cover that could be installed stably using screws on the detector package and had enough z-clearance to route the readout cables from the 400 μm array to locations where the MDM connectors are mounted on the detector package.

The Silicon fanout board was designed by Carl Ferkinhoff and manufactured by STAR Cryoelectronics LLC (NM) on a 150mm silicon wafer with 600nm Niobium traces that are used to route the connections between different multiplexer and interface chips spread around the PCB and the detector arrays. The PCB has three alignment holes and we needed to create identical, tightly aligned holes on the fanout board to register it with the PCB. To achieve this, I created a jig using an aluminum block that could be held in the milling machine providing a safe platform for the silicon board. Using alignment pins, I aligned two perpendicular edges of the silicon board such that it created a repeatable reference point that could be used as origin for guiding the mill operations and help achieve tight relative tolerances between the three holes. Silicon is a very brittle material and directly machining it is not advised. In order to safely machine the silicon fanout boards, I securely place them between two glass slides using a mounting adhesive, Crystalbond 509. Crystalbond can be easily worked by heating the application surface between 71 and 121°C (160-250F) at which point it can flow and form a uniform layer. I carefully monitored the temperature of the hot plate, maintaining it around 80°C to avoid overheating the Crystalbond and its flow. The adhesive layer should smoothen out after a minute or two

on the hot plate. It is important to ensure no air bubbles are trapped between surfaces and that both glass slides and the silicon board are aligned with the pins before turning off the hot plate. A rogue air bubble can cause fracturing of material during the machining process. I used a diamond core drill to make the required $3 \times 1/4''$ holes. After machining, the silicon board is retrieved from between the glass slides and cleaned in an Acetone bath overnight that dissolves away the Crystalbond adhesive.

The detectors used in ZEUS-2 are cooled below the temperature at which they transition from being resistive to superconducting and then voltage biased to maintain them precisely at an operating point along this transition between the two states. As the detector package is maintained at a fixed operating temperature during operations using a feedback loop, any thermal gradient along the length of the detector array appears as a change in the required operating bias for pixels on the array. We know from experience with the $400 \mu\text{m}$ array that such a gradient exists in both directions, along and across the $400 \mu\text{m}$ array and that it requires significant effort to find proper operating bias with changing sky conditions, source elevation, grating settings etc. The new array is mounted on a separate carrier that is then installed on the detector package. In order to ensure that the entire array is uniformly thermally sunk to the carrier, I coated the copper carrier with gold. The re-entrant back-short for the new array has a gold coated surface on its back and the gold surface on the copper carrier increases thermal contact conductance. We use copper tabs on three corners of the carrier that gently press on the array to maintain proper contact and avoid slippage. In order to secure the gold coat on the copper, I first deposited 30nm of platinum using e-beam evaporation, and then followed it with 300nm of gold deposited on the Pt layer using the same technique. In lab tests under various conditions,

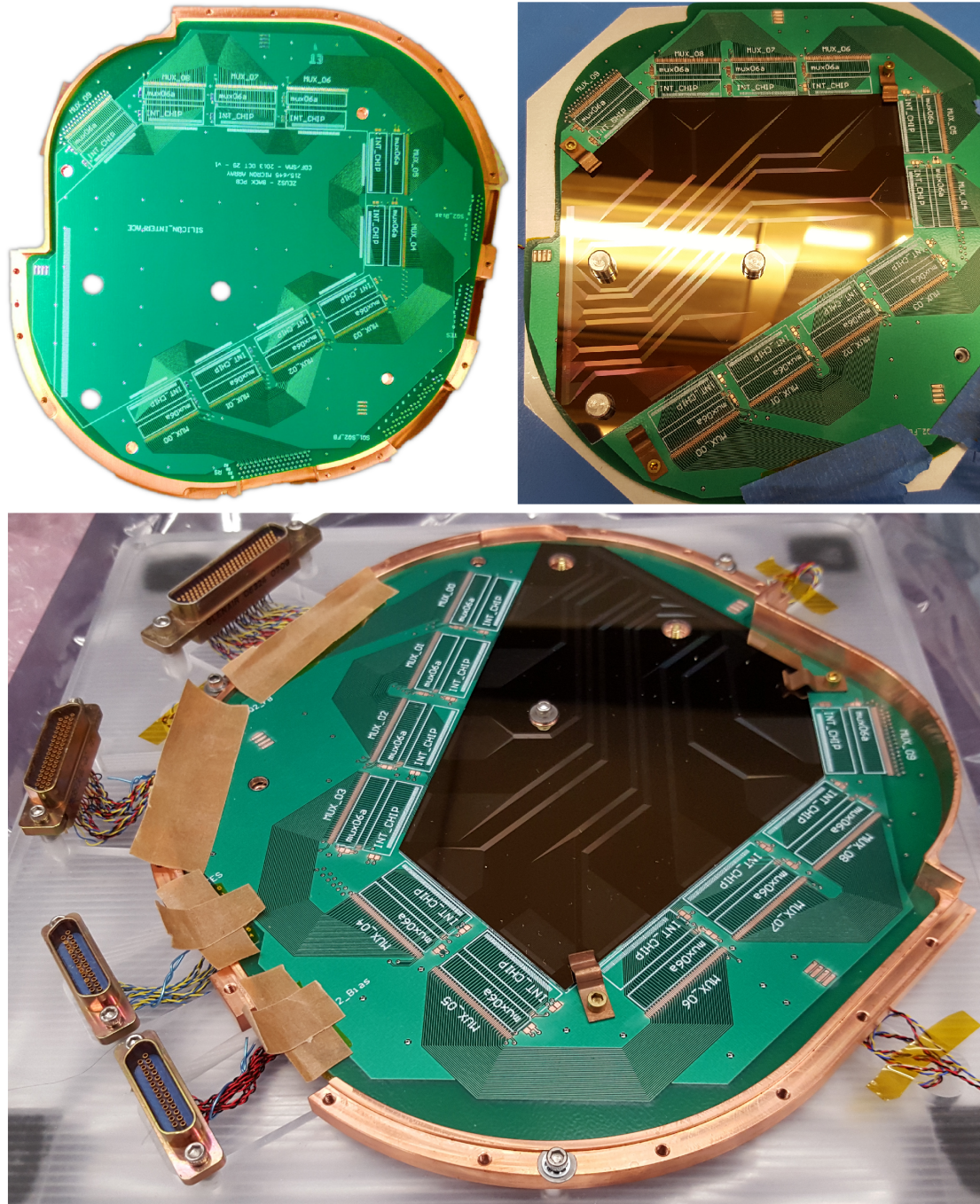


Figure 2.9 (top-left)The PCB that carries the readout components sits flush within the new copper carrier. (top-right) The silicon fanout board has three holes cut out aligned with those on the PCB and is mounted on the PCB using rubber cement and copper tabs. (bottom) Assembled PCB board before installing the detector, multiplexer and interface chips for wire bonding. Micro-D connectors are installed using wire pigtails on the PCB. They carry the connections for bias and feedback for the SQUID multiplexers and bias and readout lines for the detectors.

we find that the operational bias for the detectors across the different columns of the $200\ \mu\text{m}$ array is very uniform for any given scenario with typical variations of $\leq 5\%$.

In order to achieve fast, repeatable and reliable connections between detector arrays with a large number of pixels and the required readout electronics, it was necessary to create a layout that could be programmatically used by a wire-bonding tool to align and place the wire bonds between the various components. I created a functional layout for the bond pads with a basic cell that consists of one multiplexer (mux) chip, one interface chip and the respective bond pads on the PCB and to the Si fanout board. Every alternate mux chip repeats the same pattern of the basic cell. This reduced the amount of effort from creating a layout for each of the ten readout columns to only two basic cells. The bond pads for TES and the second stage squid amplifiers bias are aligned the exact same way for each readout column on the PCB, I leveraged this uniformity to align the chips when installing them on the PCB. A separate layout was made for bonds between the array bond pads and those on the Si fanout board.

The wire bonding machine used by Advotech Inc. was a Large Area Wedge Bonder by Kulicke & Soffa, Model 8090. The XY table has an operating XY-stage that allows the bonding tool to traverse and an area $16.0'' \times 14.0''$. It was programmed using a proprietary interface software and operated by a technician from Advotech Inc. A typical requirement for the wedge bonders is that the z-height of the bond pads should be as close as possible or else the quality of the bonds is compromised. The bond pad material between the chips (niobium) and the PCB (copper) is different and requires different bonding parameters for

either end of the bond. The bond pad heights for bonds between the PCB to the mux chip and from the Si fanout board to the detector arrays were placed at Δz of as large as 2.5 mm. The copper back half on which the PCB, readout components and the detector arrays were mounted was rigidly mounted to a custom machined aluminum block that allowed us to raise the work piece such that the bond pads were at the optimal height required by the wire bonding machine. When dealing with slightly different bond pad heights between the PCB and the chips, we used a 0.5 mm stainless steel spacer and moved the copper bond pads on the PCB to the optimal bonding height as placing a strong bond on the copper bond pads is significantly harder than on niobium bond pads.

The bond pads on the Si fanout board and the detector arrays were misaligned by 5.3 mm at the left-hand end. The angle due to the misalignment and the lip around the array carrier created a situation that would block the wedge of the wire-bonder to travel down to the silicon board and make a connection. Due to these issues, 8 pixels on the $650 \mu\text{m}$ array do not have any connections to the readout components. On experimenting with various bonding parameters to accommodate the large z-height difference between the array and the fanout board, we found best results when we started the first bond at the array (pads slightly higher than the optimal bonding height), reduce the loop height and increasing the bond length so as to reach perfectly the bond pads on the fanout board. For redundancy, each bias and return connection between a pixel and the fanout board has two bonds. We use a multiplexing factor of 28:1 in ZEUS-2, to simplify the readout scheme, we chose to drop 5 pixels (out of 201) on the $215 \mu\text{m}$ array as 196 pixels are read out using 7 multiplexer chips. The 56 pixels (only 48 connected to detectors due to misalignment between bond pads as described earlier) on the $645 \mu\text{m}$ array are read out using additional two mux

chips. The PCB was designed to readout 10 readout columns and multiplexing is achieved by activating one row select line across all column at a time, hence we installed a fully functional pair of mux and interface chip on the last column that has no detectors connected to it to complete the readout loop.

We also installed two bare-chip Ruthenium oxide (Rox) temperature sensors (RX-102A-BR), one right next to the detector array and another diametrically opposite near the readout components, to provide readings of the detector temperature as close to the pixels as possible and help measure any temperature gradient across the detector package. We were using a similar Rox sensor but in a different packaging (RX-102A-CD) and installed on the outer surface of the detector package. The new bare chip sensor in the immediate vicinity of the detector array is now used to servo the PID loop that maintains the detector temperature. The bare chip sensor and the older sensor (still installed on the same spot) measure a $\Delta T \sim 6$ mK.

After completing the wire bonding process, the mK cold finger was attached at the back of the detector package and all the micro-D connectors for bias and readout were mounted on standoffs. As both halves of the detector package are now populated, extra caution has to be exercised whenever handling either of them and specially when closing the detector package. We now use three guide screws that register a single plane will ample initial clearance to safely place the two halves on top of each other. We can then drive the guide screws half turn at a time and mate the two halves of the detector package safely.

We have performed initial tests on the detector array and have disconnected the readout connections for one column on the $215 \mu\text{m}$ array due to shorts that cause runaway heating on the detector package. The TES bias line associated

with the problematic column appears to have a very high impedance short ($\sim M\Omega$) through ground to the feedback line of multiple second stage SQUID amplifiers. Another column has an open feedback line for the second stage SQUID. These issues can be mitigated by identifying a or few row select SQUIDs that may be problematic or replacing the entire mux and/or interface chip for one of the readout columns. The open connection on the feedback line can be fixed by tracing the location of the open connection between the MCE and the detector package. All working detectors show I-V curves with superconducting branches out to 160 mK, suggesting that the transition temperature is close to 170 mK. The noise measurements taken by staring at a cold load of liquid nitrogen for a minute suggest that the mean noise on the 215 μm array is $\sim 1.3\times$ larger than that measured on the 400 μm array. Spectral line observations of various ^{12}CO and ^{13}CO lines, confirm the grating alignment and range. Detailed dark tests to measure the detector properties will take place in the near future, with graduate student Christopher Rooney leading the effort — ZEUS-2 is in safe hands.

CHAPTER 3

DETECTION OF [O III] AT $z \sim 3$: A GALAXY ABOVE THE MAIN-SEQUENCE, RAPIDLY ASSEMBLING ITS STELLAR MASS

3.1 Abstract

We detect bright emission in the far infrared fine structure [O III] $88 \mu\text{m}$ line from a strong lensing candidate galaxy, H-ATLASJ113526.3-014605, hereafter G12v2.43, at $z = 3.127$, using the 2nd generation Redshift (z) and Early Universe Spectrometer (ZEUS-2) at the Atacama Pathfinder Experiment Telescope (APEX). This is only the fifth detection of this far-IR line from a submillimeter galaxy at the epoch of galaxy assembly. The observed [O III] luminosity of $7.1 \times 10^9 (\frac{10}{\mu}) L_{\odot}$ likely arises from HII regions around massive stars, and the amount of Lyman continuum photons required to support the ionization indicate the presence of $(1.2 - 5.2) \times 10^6 (\frac{10}{\mu})$ equivalent O5.5 or higher stars; where μ would be the lensing magnification factor. The observed line luminosity also requires a minimum mass of $\sim 2 \times 10^8 (\frac{10}{\mu}) M_{\odot}$ in ionized gas, that is 0.33% of the estimated total molecular gas mass of $6 \times 10^{10} (\frac{10}{\mu}) M_{\odot}$. We compile multi-band photometry tracing rest-frame UV to millimeter continuum emission to further constrain the properties of this dusty high redshift star-forming galaxy. Via SED modeling we find G12v2.43 is forming stars at a rate of $916 (\frac{10}{\mu}) M_{\odot} \text{yr}^{-1}$ and already has a stellar mass of $8 \times 10^{10} (\frac{10}{\mu}) M_{\odot}$. We also constrain the age of the current starburst to be ≤ 5 million years, making G12v2.43 a gas rich galaxy lying above the star-forming main sequence at $z \sim 3$, undergoing a growth spurt and could be on the main sequence within the derived gas depletion timescale of ~ 66 million years.

3.2 Introduction

Over the past 20 years, wide-field multi-band surveys have demonstrated that the star formation rate per unit comoving volume of the Universe rose quickly soon after re-ionization and peaked at redshifts between $z \sim 3$ and 1 (look-back times of ~ 11.5 to 7.7 Gyr) at rates 10 to 15 times the present-day values (see e.g., [Madau & Dickinson, 2014](#)). Locally, and even back beyond redshift 3, a substantial fraction of star formation within galaxies is obscured by dust. This dust absorbs starlight, and re-radiates its power in the far-infrared continuum. For most high luminosity star-forming galaxies, the far-infrared luminosity exceeds the optical/UV luminosity so we have come to call these dusty star-forming galaxies (DSFGs). DSFGs dominate the rise in star formation rate density looking back in time to at least beyond redshift of 3, so it is important to study DSFGs in their rest-frame far-infrared bands to properly understand the history of star formation in the Universe.

We have constructed two sub-millimeter (submm) grating spectrometers, ZEUS [Hailey-Dunsheath \(2009\)](#) and ZEUS-2 [Ferkinhoff et al. \(2014\)](#), in order to measure far-infrared fine-structure line emission from luminous star-forming galaxies between $z=1-5$. These far-infrared lines (e.g. [C II] 158, [N II] 122 & 205, [O III] 88 & 52 μm) are important coolants of the gas, and excellent probes of both the physical properties of the emitting medium and the dominant sources of luminosity – a burst of star formation activity or accretion onto a super-massive black hole. They have advantages over the optical lines in that they are typically optically thin, insensitive to extinction by dust¹, and for lines arising from ionized gas, they are also insensitive to the ionized gas temperature. In the local

¹Extinction optical depth of unity requires a gas column of $N_{\text{H}} > 10^{24} \text{ cm}^{-2}$ for $\lambda \geq 60 \mu\text{m}$ [Draine \(2003\)](#).

Universe, a full complement of far-IR fine structure lines have been studied in many sources, helping us to constrain the properties of the interstellar medium and the host stellar populations, using airborne and space based instruments (e.g., Brauher et al., 2008, Carral et al., 1994, Colbert et al., 1999, Cormier et al., 2015, Díaz-Santos et al., 2017, Farrah et al., 2013, Graciá-Carpio et al., 2011, Lord et al., 1996, Stacey et al., 1991). At $z > 0.2$, sensitivity of instruments and the Earth’s atmosphere makes measurements of these lines very challenging. Using our ZEUS instruments, we are surveying star-forming galaxies in the redshift 1 to 5 epoch in their far-infrared fine-structure line emission, including the [C II] $158 \mu\text{m}$ line (Brisbin et al., 2015, Ferkinhoff et al., 2014, Hailey-Dunsheath et al., 2010, Stacey et al., 2010).

The far-IR lines of [O III] and [N II] arise in HII regions, and are prominent coolants tracing the physical conditions and excitation mechanism of gas in sites of active star formation. The lines individually allow us to measure the flux of ionizing radiation while, the [O III] $88 \mu\text{m}$ /[N II] $122 \mu\text{m}$ line ratio (modulo abundance considerations) is primarily sensitive to the hardness of the radiation field (e.g. Rubin, 1985). Combined, these constraints provide a luminosity-weighted measurement of the number and type of the of the most massive stars still on the main sequence and hence the intensity and age of the most recent starburst (c.f. Ferkinhoff et al., 2010). To pursue our goal of characterizing the starbursts in high redshift DSFGs, we are surveying the [O III] $88 \mu\text{m}$ and [N II] $122 \mu\text{m}$ lines using our submm grating spectrometers ZEUS (on CSO) and ZEUS-2 (on APEX)². Theoretical modeling of emission regions and observations of local galaxies suggest that the [N II] $122 \mu\text{m}$ line is fainter than the [O III] $88 \mu\text{m}$ line, and only two detections have been reported at $z > 1$, both in composite starburst-

²APEX is a collaboration between the Max-Planck-Institut für Radioastronomie, the European Southern Observatory, and the Onsala Space Observatory.

AGN systems, by (Ferkinhoff et al., 2015, Ferkinhoff et al., 2011). To date, the [O III] 88 μm line has only been reported in five high redshift submm galaxies (SMGs); two detected with ZEUS, two with Herschel-SPIRE in $z\sim 3$ lensed SMGs (Rigopoulou et al., 2018, Valtchanov et al., 2011) and one with ALMA at $z\sim 6.9$ (Marrone et al., 2017). Three additional detections of the [O III] 88 μm line have been reported in clumps associated with Ly- α systems at $z\sim 7-8$, using ALMA (Carniani et al., 2017, Inoue et al., 2016, Laporte et al., 2017). Here, we report observations of the [O III] 88 μm line in a Herschel discovered SMG, G12v2.43 at $z=3.127$ with ZEUS-2 on the APEX telescope in the 350 μm waveband.

G12v2.43 (RA: 11:35:26.3 Dec: -01:46:06.5, J2000) was discovered in the Herschel Astrophysical Terahertz Large Area Survey (H-ATLAS, Clements et al., 2010), and was selected as a candidate high redshift gravitationally lensed source due to its large 500 μm flux density ($S_{500\mu\text{m}} > 0.1$ Jy). It was confirmed as a high redshift ($z=3.1276\pm 0.0005$) system through mm-band spectroscopy using the Green Bank Telescope (GBT, Harris et al., 2012) and the Northern Extended Millimeter Array (NOEMA, Yang et al., 2016). These observations show powerful emission in low-J CO and H₂O rotational lines, thereby confirming G12v2.43's extreme luminosity. In a high spatial resolution study, using the Sub-millimeter Array (SMA), Bussmann et al. (2013) reported the detection of (observed frame) 896 μm continuum. The source was marginally resolved but did not show any extended emission or obvious signatures of gravitational lensing like multiple images or lensing arcs at 0".8 (FWHM) scale. Follow up deep near-infrared imaging to find the foreground lensing galaxy by Calanog et al. (2014) detected no significant emission in the K_s band either from the foreground lens or the background high redshift galaxy. We note that the coordinates reported above are the true centroid of the emission seen in the SMA

map and are offset by $1''.4$ from the those reported in [Busmann et al. \(2013\)](#).

A reasonable explanation for its extreme luminosity, L_{IR} , of $\sim 1.2 \times 10^{14} L_{\odot}$ ([Busmann et al., 2013](#)) could be magnification due to gravitational lensing, as was suggested by [Harris et al. \(2012\)](#) due to the large CO luminosity and small line FWHM. For discussion related to physical quantities in this paper, we adopt a scaling factor of $(\frac{10}{\mu})$, where μ would be the true lensing magnification factor. Within the purview of existing observations, the influence of gravitational lensing for G12v2.43 remains unconstrained. However as a reference for the reader, galaxies with such extreme observed luminosities and well constrained lensing models have a median magnification factor of $\mu \sim 6$ (e.g., [Busmann et al., 2013](#), [Spilker et al., 2016](#)). If confirmed, the apparent brightness of G12v2.43 would allow future observations to study a normal galaxy building up its stellar mass at sub-kpc resolution and study the interplay between star formation and galaxy evolution only 2 billion years after the Big Bang.

In this paper we present the [O III] $88 \mu\text{m}$ line observations and compile broadband photometry from UV to mm wavelengths towards G12v2.43 to study the properties of its ionized gas, dust and stellar populations. In Section 3.3, we present the ZEUS-2/APEX observations and discuss the constraints on its young stellar population and ionized gas mass. In Section 3.4, we compile new observations of G12v2.43 from various archives; namely near-infrared data taken with the Hubble and Spitzer Space Telescopes and far-infrared photometry and spectroscopy with the Herschel Space Observatory. In Section 3.5, we present spectral energy distribution modeling of the photometric data and discuss the ISM properties of G12v2.43 and the potential of it being a gravitationally lensed system. Throughout this paper we assume a flat Λ CDM cos-

mology with a Hubble constant of $70 \text{ km s}^{-1} \text{ Mpc}^{-1}$, $\Omega_M = 0.3$, and $\Omega_\Lambda = 0.7$, giving G12v2.43 a luminosity distance of 26.7 Gpc and a linear scale of $7.6 \text{ kpc arcsec}^{-1}$.

3.3 ZEUS-2/APEX Observations and results

The second generation redshift(z) and Early Universe Spectrometer (ZEUS-2) is a grating spectrometer optimized for detecting broad (few 100 km s^{-1}) spectral lines from distant galaxies as they are redshifted into the short sub-mm telluric windows (Ferkinhoff et al., 2012, 2014, Parshley et al., 2012). We observed G12v2.43 with ZEUS-2 at the Atacama Pathfinder Experiment (APEX) telescope (Güsten et al., 2006) in 2014 October under very good weather conditions. The telescope was pointed at the co-ordinates reported in Bussmann et al. (2013), offset by $1''.4$ from the peak of the sub-mm emission, but well within the ZEUS-2/APEX beam. The precipitable water vapor remained stable between 0.5 and 0.56 mm which corresponds to a line of sight transmission of 31-42% at $365 \mu\text{m}$ during the course of the observations.

The [O III] $88 \mu\text{m}$ line was observed at $364.7 \mu\text{m}$ based on the redshift reported by Harris et al. (2012). The resolving power of the instrument at $365 \mu\text{m}$ (in the 5th order of the echelle grating) is $R \sim 960$. Each spectral pixel covers $\sim 313 \text{ km s}^{-1}$ in velocity space with the array providing an instantaneous coverage of $\sim 3500 \text{ km s}^{-1}$. Data was taken in standard chop/nod mode, with 2 Hz chop frequency and a $30''$ azimuthal chop-throw. The source elevation was between $50\text{-}68^\circ$ during the observations. Three grating settings were used to move the line along spectral pixels to increase total spectral coverage and eliminate gaps due to non-functioning pixels. As a result, the data are sampled at

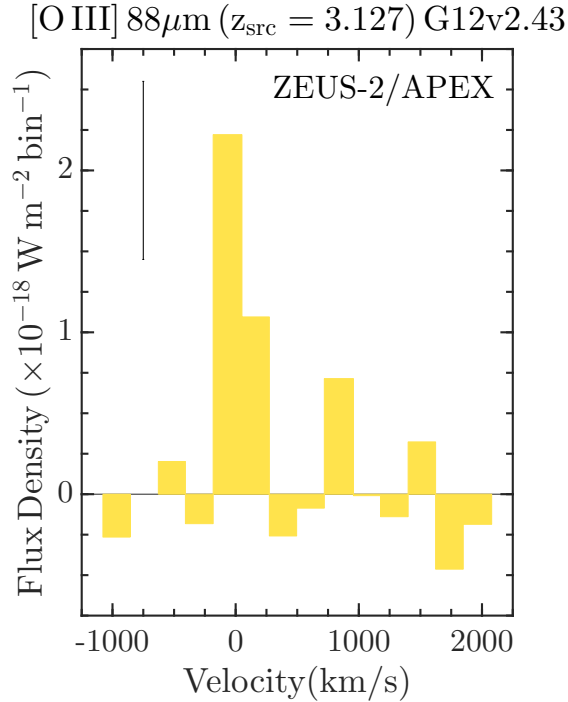


Figure 3.1 ZEUS-2/APEX spectrum of the [O III] $88\mu\text{m}$ emission line observed in G12v2.43 at a redshift of $z = 3.127$. The velocity scale is with respect to the source redshift. Typical per bin $1\text{-}\sigma$ error is shown in top-left.

230 km s^{-1} , finer than our resolution element of 313 km s^{-1} . We obtained 8×10 minute integrations with a chop efficiency of 63% giving a total on-source integration time of 25.2 minutes. Pointing and focus observations were taken on the $^{12}\text{CO}(6\text{-}5)$ line from IRC10216, and were repeated every 20 minutes. Pointing was found accurate to within $2''$ over the duration of the observations. The ZEUS-2/APEX beam at $365\mu\text{m}$ was measured using Uranus as $7''.8 \pm 0''.9$. Gain calibration for spectral pixels was done by chopping an ambient temperature blackbody against cold sky before and after each set of on-source observations and flux calibration was verified with Jupiter and Uranus. The signal we measured from Uranus, indicates that the point source coupling for APEX is $\sim 40\%$ at $365\mu\text{m}$. We detected the [O III] $88\mu\text{m}$ line, shown here in Figure 3.1, at a flux level of $3.2 \pm 0.4 \times 10^{-18} \text{ W m}^{-2}$ ($S/N=7.5$), or equivalently $116 \pm 15 \text{ Jy km s}^{-1}$,

with an estimated calibration uncertainty of 30%. We advise the reader to use the velocity FWHM of 225 km s^{-1} , derived by spectrally resolved observations of [Harris et al. \(2012\)](#) and [Yang et al. \(2016\)](#) for the CO and H₂O lines respectively, to estimate the peak line flux density.

3.3.1 [O III] line emission: Young stars and Ionized gas mass

As the O⁺⁺ ion requires 35 eV to form, it indicates the presence of a very hard ionizing source which could either be upper main sequence stars, with effective temperature $>36,000$, in the vicinity of the emitting region or a nearby Active Galactic Nucleus (AGN). Assuming the star formation dominated scenario, the [O III] line emission can be used to constrain the type of stars producing the ionizing radiation (O8 or hotter) and the line luminosity can be used to estimate the flux of ionizing photons required to support the observed emission. Using theoretical models for upper main sequence stars, we can scale the number of ionizing photons produced by a certain spectral type of O-star to estimate the number of such stars present, on average, in the host galaxy. Also, since the most massive stars spend a relatively short amount of time on the main sequence, up to about 3–10 million years, the observed [O III] line emission places a constraint on the age of the most recent starburst.

Our observations of the [O III] $88 \mu\text{m}$ line flux corresponds to a luminosity of $7.1 \times 10^9 \left(\frac{10}{\mu}\right) L_{\odot}$ at the distance of G12v2.43. In Section 3.5.1, we suggest that the emission seen from G12v2.43 is dominated by star-formation activity and not from an AGN with the help of broadband SED modeling. With the [O III] line flux, we can constrain the number of photons capable of doubly ionizing

oxygen, and estimate the number of O-stars given an upper mass cutoff. We use the HII region models of [Rubin \(1985\)](#) to scale the observed line flux and estimate the number of Lyman continuum photons. The effective stellar temperatures, T_{eff} , used in the models are matched with those of the spectral type of main sequence O-stars using the calibration of [Martins et al. \(2005\)](#). The main sequence lifetime is based on the Hydrogen burning timescale reported by [Ekström et al. \(2012\)](#) for massive stars of solar metallicity. We use Rubin's 'K' models which are based on stellar atmosphere models from [Kurucz \(1979, 1993\)](#) with an [O/H] abundance of 6.76×10^{-4} , to predict the [O III] line luminosity as a function of the effective stellar temperature of the star ($T_{\text{eff}}=31\text{-}45$ kK), the Lyman continuum (LyC) photon rate ($Q_0=10^{49-50} \text{ s}^{-1}$), and the electron number density in the HII regions ($n_e = 10^{2-4} \text{ cm}^{-3}$). The models are set up such that the line intensities scale linearly for models with varying Q_0 , so that the derived number of stars for the model with $Q_0 = 10^{49} \text{ s}^{-1}$ would be 10 times the number of stars derived for models with $Q_0 = 10^{50} \text{ s}^{-1}$. The models with $n_e = 10^3 \text{ cm}^{-3}$ and $T_{\text{eff}}=40,000$ and $45,000\text{K}$ provide the best fit with the derived number of LyC photon rate, $Q_0 \approx 5.7 \times 10^{55} (\frac{10}{\mu}) \text{ s}^{-1}$. This LyC flux level require $(1.2 - 5.2) \times 10^6 (\frac{10}{\mu})$ O3V to O5.5V stars. An estimate using the total bolometric luminosity of such upper main sequence stars present in the galaxy suggests that if all their starlight were absorbed by dust and re-radiated in the far-infrared, that could account for $(0.8 - 1.3) \times 10^{12} (\frac{10}{\mu}) L_{\odot}$, i.e., $\sim 12\%$ of the observed FIR luminosity of $8.3 \times 10^{12} (\frac{10}{\mu}) L_{\odot}$.

Following [Ferkinhoff et al. \(2010\)](#), in the high density, high temperature limit, we can estimate the minimum mass ionized nebula required to support

the luminosity of the observed [O III] line as:

$$M_{\min}^{\text{H}^+} = 4\pi d_L^2 \frac{F_{\text{O III}}}{\frac{g_l}{g_t} A_{ul} h \nu_{ul}} \frac{m_{\text{H}}}{\chi_{\text{O}^{++}}} \quad (3.1)$$

Here, $F_{\text{O III}}$ is the observed line flux (W m^{-2}), d_L is the luminosity distance (m), g_l is the statistical weight ($2J+1$) for the $J=1$ emitting level, $g_t = \sum_i g_i e^{-\Delta E_i/kT}$, is the partition function, A_{ul} is the spontaneous emission coefficient (s^{-1}), h is the Planck's constant (J-s), ν_{ul} is the rest frequency of the line, 3393.00624 GHz ($88.356 \mu\text{m}$), m_{H} is the mass of a hydrogen atom, and $\chi_{\text{O}^{++}}$, is the relative abundance of (O^{++}/H^+). Adopting a nebular gas phase abundance, $[\text{O}/\text{H}] = 5.9 \times 10^{-4}$ and assuming all the oxygen is doubly ionized ($[\text{O}/\text{H}] = [\text{O}^{++}/\text{H}^+]$), we find that the minimum ionized gas mass in G12v2.43 is $(2.0 \pm 0.3) \times 10^8 (\frac{10}{\mu}) M_{\odot}$. The minimum mass of doubly ionized oxygen itself is, $\sim 1.9 \times 10^6 (\frac{10}{\mu}) M_{\odot}$.

3.4 Supporting Observations

Previous observations of G12v2.43 have been reported by [Harris et al. \(2012\)](#), [Bussmann et al. \(2013\)](#), and [Yang et al. \(2016\)](#). However, these authors only discuss emission at wavelengths longer than (observed frame) $200 \mu\text{m}$, so that many of the source properties, including the stellar mass and the total luminosity are not well constrained. We compile published and archival observations to produce a rest-frame near-UV to mm SED which we use to constrain the star formation history, stellar mass, total luminosity and dust properties. As the source is compact and the beam of the various instruments vary from $0'.15\text{-}35''$, flux densities (or limits) were derived via aperture photometry in the recommended manner for each instrument assuming a point source. These data are

summarized in Table 3.1.

3.4.1 Archival: Hubble Space Telescope WFC3

As part of a snapshot program to identify gravitationally lensed galaxies (PI: Negrello, ID: 12488), G12v2.43 was observed with the HST Wide-field Camera using the wide near-infrared filter F110W for 711.7 seconds in 2013 July. In a lensing system, the near-infrared images are typically used to identify the foreground lensing galaxy and the rest frame near-UV to optical light tracing stellar emission in the background higher redshift galaxy. We obtained the pipeline calibrated images from the Hubble Legacy Archive to investigate the presence of either a foreground galaxy, or any structure like arcs or an Einstein ring, that could be characteristic of strong gravitational lensing.

We identify a source in the near-IR WFC3 F110W image at $5.1\text{-}\sigma$ significance that is consistent with the centroid of the emission seen from the high- z galaxy in interferometric observations from SMA (Figure 3.2). The emission is faint ($m_{AB}=24.2$), and another source is seen $1''$ north-west of the location of the high- z galaxy. Previous attempts at identifying the foreground lensing galaxy in the K_s band using deep Keck observations have been unsuccessful (Calanog et al., 2014) and, we cannot say with certainty whether these two sources are actually patchy emission in rest-frame near-UV from G12v2.43 or could be partially attributed to a foreground, perhaps lensing galaxy. As the emission is extended around the two features, to estimate the flux density of the high- z source, we perform photometry with a $1''$ circular aperture centered at the peak of the SMA emission to avoid picking up flux from the nearby source and subtract the me-

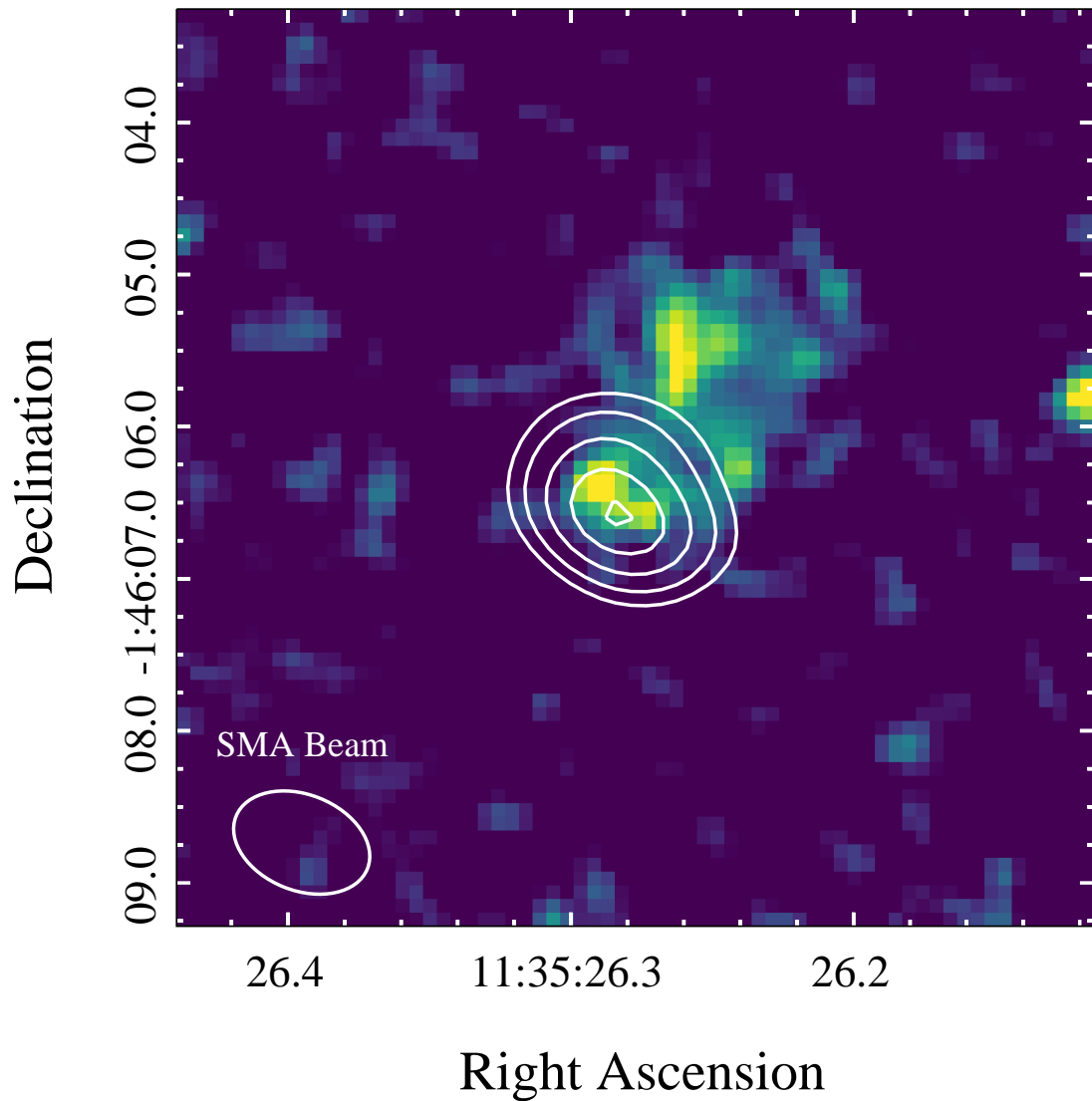


Figure 3.2 (Background: Color map)- A $6'' \times 6''$ stamp of $1.1 \mu\text{m}$ WFC3 image at the position of G12v2.43. The emission in the HST/WFC3 image shows two sources near the expected high-z source location, separated by $\sim 1''$. (Foreground, White Contours) $896 \mu\text{m}$ continuum emission detected at the position of G12v2.43 with the SMA (from [Bussmann et al., 2013](#)). The contours, starting from the center, show the peak of the emission detected at $24\text{-}\sigma$ and moving out to $(17, 12, 8.5, 6)\text{-}\sigma$ levels. The white ellipse in the bottom-left corner indicates the beam size of the SMA observations (FWHM: $0'.93 \times 0'.63$).

dian sky from each pixel.

3.4.2 Archival: Spitzer Space Telescope

We obtained the pipeline calibrated images of G12v2.43 from the Spitzer Heritage Archive. The source was observed using the Spitzer Infrared Array Camera (IRAC) in Cycle 11 (PI: A. Cooray, Program ID 80156) in the 3.6 and 4.5 μm bands. The on-source integration time was 706 seconds. Emission in the IRAC bands traces near-IR light from the high redshift source at the effective rest-frame wavelength of 872 nm and 1090 nm. We find bright emission in both bands at the source location, consistent with the HST F110W image reported in the previous section and with the interferometric SMA imaging, and no signs of extended emission or artifacts. We perform photometry on the Level-2 pipeline products (post-BCD) following the methodology described in the Appendix B of the IRAC instrumentation handbook. Since the data are undersampled and there is no clear evidence for extended emission at the IRAC resolution, we perform source fitting and aperture photometry in the recommended manner using both a 3.6'' and 6'' aperture to estimate the flux density. The uncertainties are estimated from the uncertainty image provided with the science data products from the archive and compared to the background estimated using a large annulus around the source. The uncertainty derived from the uncertainty maps is smaller than the 5% calibration accuracy of IRAC, but the difference between various size apertures is larger, about 10%. We quote this 10% uncertainty for both of the measured flux densities for G12v2.43.

Table 3.1. Photometry Data for G12v2.43

Wavelength (μm)	Frequency (GHz)	Flux Density (mJy)	Instrument
1.15	260689.1	$0.9 \pm 0.2 \times 10^{-3}$	HST/WFC3
3.4	88174.3	$29 \pm 6 \times 10^{-3}$	WISE/W1
3.6	83275.7	$31 \pm 3 \times 10^{-3}$	Spitzer/IRAC1
4.5	66620.5	$45 \pm 4 \times 10^{-3}$	Spitzer/IRAC2
4.6	65172.3	$31 \pm 11 \times 10^{-3}$	WISE/W2
12	24982.7	< 0.49	WISE/W3
22	13626.9	< 3.9	WISE/W4
70	4282.7	19 ± 3	Herschel/PACS
100	2997.9	56 ± 6	Herschel/PACS
160	1873.7	180 ± 12	Herschel/PACS
250	1199.2	296 ± 17	Herschel/SPIRE
350	856.5	306 ± 24	Herschel/SPIRE
500	599.6	214 ± 23	Herschel/SPIRE
896	334.6	50 ± 3	SMA
1064	281.8	36.4 ± 0.3	NOEMA
1252	239.4	22.5 ± 0.5	NOEMA
208900	1.435	< 0.36	VLA/FIRST

Note. — Wavelength/Frequency in observed frame; All upper limits are $3\text{-}\sigma$

3.4.3 Archival: Wide-field Infrared Survey Explorer

We utilized the publicly available All-sky data release from the Wide-field Infrared Survey Explorer (WISE) (Wright et al., 2010) to look for emission from G12v2.43 between 3.4 and 22 μm . We queried the AllWISE point source catalog for entries within $5''$ of the Spitzer position. The source was only detected (5σ) in W1 (3.35 μm) band and we derived 3 sigma upper limits for the flux density in in the W2 (4.6 μm), W3 (11.56 μm) and W4 (22.1 μm) bands based on the magnitudes reported in the catalog, see Table 3.1.

3.4.4 Archival: Herschel Space Telescope

Photometry

Due to the redshift of G12v2.43 ($z=3.127$), the mid-infrared part of the spectral energy distribution, which could help constrain emission from a hot dust component or an obscured AGN, is shifted into the far-infrared bands covered by the PACS and SPIRE instruments on-board the Herschel Space Observatory.

We present observations of G12v2.43 taken in the 70, 100, and 160 μm bands of the PACS photometer (Poglitsch et al., 2010). The observations used here were taken as a part of the observing programs, OT1_rivison_1, Observation ID: 1342224173,74, on OD 792 and OT2_jwardlow_2, Observation ID: 1342257109-112, on OD 1309. The source was observed for 276–558 seconds in each band. This data was processed using HIPE version 15 (Ott, 2010) through pipeline version 14.2. We combined all the observations of G12v2.43 in each PACS band and then perform point-source aperture photometry using the task, sourceExtractorSussexextractor. We detect the source in all three PACS bands. The flux density derived in the 160 μm band is lower by 17% than the value reported by Wardlow et al. (2017) but consistent with that reported in the PACS point source catalog (Marton et al., 2017). Statistical error in the measurement was calculated by estimating the noise level in the map in each band. The SPIRE bands span across the peak of the dust emission at $z\sim 3$ and are critical to estimate dust properties and the far-infrared luminosity. We use the flux density reported in the SPIRE point source catalog (Schulz et al., 2017) at the location of G12v2.43. The color correction required for SPIRE data points is 1.02 at 250 μm , 0.97 at 350 μm and 0.95 at 500 μm . In Table 3.1, the errors reported with the SPIRE flux densities

are the confusion noise in the maps as reported by the point source catalog. The confusion noise is much larger than the 5% calibration uncertainty or the statistical noise derived by the sourceExtractorTimeline task in HIPE (2-3%).

Spectroscopy

G12v2.43 was observed with the SPIRE Fourier Transform Spectrometer (Griffin et al., 2010). The observations used here were taken as a part of the observing program OT1_rivison_1, Observation ID: 1342247744, on OD 1150 in high-resolution mode for 13752 seconds towards the end of the Herschel mission. We reprocessed the data through HIPE 15 with SPIRE calibration version 14.3 and corrected for instrumental artifacts. The spectral shape and absolute flux calibration were verified by comparing the SPIRE photometry with synthetic measurements derived from the corrected spectral data, using the task spireSynthPhotometry within HIPE 15. The inherent instrument response of a Fourier Transform Spectrometer is a sinc function, that has 20% sidelobes associated with each peak. Instead of looking at a single co-added scan and deriving limits for the line fluxes, we improve the noise characterization by creating multiple realizations of averaged scans by randomly selecting 100 out of the 200 available scans. As only half of the available scans were used in each realization, the sensitivity in each scan would, in principle be worse by a factor of $\sqrt{2}$. From these realizations, we estimate the noise in a 5 GHz band centered at the frequency of individual far-IR lines. No lines are detected at high significance and the 3- σ limits are listed in Table 3.2.

The electronic ground state of doubly ionized oxygen is split by fine structure interactions into three levels, ground (3P_0), and two excited states, 3P_1 , and

Table 3.2. Far-IR Fine Structure Lines in PACS/SPIRE Observations of G12v2.43

Line ID	Rest Wavelength (μm)	Line Flux, $3\text{-}\sigma$ ($10^{-17} \text{ W m}^{-2}$)
[O IV] $^2\text{P}_{3/2} \rightarrow ^2\text{P}_{1/2}$	25.91	$<0.7^{\text{a}}$
[O III] $^3\text{P}_2 \rightarrow ^3\text{P}_1$	51.81	<0.6
[N III] $^2\text{P}_{3/2} \rightarrow ^2\text{P}_{1/2}$	57.34	<0.7
[O I] $^3\text{P}_1 \rightarrow ^3\text{P}_2$	63.18	<0.6
[O III] $^3\text{P}_1 \rightarrow ^3\text{P}_0$	88.36	<0.8
[N II] $^3\text{P}_2 \rightarrow ^3\text{P}_1$	121.89	<0.8
[O I] $^3\text{P}_0 \rightarrow ^3\text{P}_1$	145.53	<1.1
[C II] $^2\text{P}_{3/2} \rightarrow ^2\text{P}_{1/2}$	157.74	<1.4

^aLine flux limit from [Wardlow et al. \(2017\)](#)

$^3\text{P}_2$. As the fine-structure states are only a few hundred K above the ground state, ions can be collisionally excited by free electrons in the HII regions (typical temperature ~ 8000 K), to occupy these states. The $3\text{-}\sigma$ limit for the upper transition, $^3\text{P}_2 \rightarrow ^3\text{P}_1$ at $52 \mu\text{m}$, of $L_{[\text{O III}]} < 6.1 \times 10^{-18} \text{ W m}^{-2}$, in conjunction with our detection of the ground state transition, $^3\text{P}_1 \rightarrow ^3\text{P}_0$ at $88 \mu\text{m}$ allows us to constrain the density of the emitting gas by comparing the observed line ratio to the theoretical line emissivity ratio ([Rubin, 1989](#)). The luminosity ratio of the two [OIII] lines, $\frac{L_{[\text{O III}] 52 \mu\text{m}}}{L_{[\text{O III}] 88 \mu\text{m}}} < 1.92$, suggests that the emitting gas has density, $n < 610 \text{ cm}^{-3}$. This is consistent with our choice of HII region models with density, $n=10^{2-3} \text{ cm}^{-3}$, used to interpret the [OIII] $88 \mu\text{m}$ line emission in Section 3.3. Similarly, the $3\text{-}\sigma$ limit for the the [C II] $158 \mu\text{m}$ line flux, $L_{\text{C II}} < 1.4 \times 10^{-17} \text{ W m}^{-2}$, yields a [C II]/FIR luminosity ratio $\leq 0.4\%$, consistent with the ratio observed in other DSFGs at $z \sim 1\text{-}5$. (e.g., [Gullberg et al., 2015](#), [Stacey et al., 2010](#)).

3.5 Discussion

In order to understand the star formation history and properties of the stellar populations and the interstellar medium of G12v2.43, we address the observed properties of the source in the context of synthesized star formation models, and dust emission and spectral energy distribution models.

3.5.1 UV-to-mm Spectral Energy Distribution

Leveraging the broad band coverage we have compiled here for G12v2.43, we perform SED fitting using CIGALE (Code Investigating GALaxy Emission, [Noll et al., 2009](#), [Serra et al., 2011](#)) and the high- z extension of MAGPHYS (Multi-wavelength Analysis of Galaxy Physical Properties, [da Cunha et al., 2008, 2015](#)) with all available photometric data points, described in Section 3.4. As the search for a lensing galaxy has been unsuccessful ([Calanog et al., 2014](#)), it is conceivable that the near-IR emission seen in the HST and IRAC maps is at least in part from the high- z galaxy. As mentioned in Section 3.4.1, to estimate the flux density at $1.15 \mu\text{m}$, we only use the emission co-incident with the centroid of the emission seen in SMA observations. As the Spitzer/IRAC beam is big enough to contain emission from the nearby source, for the purpose of SED modeling we assign an error of 50% on the flux density at 3.6 and $4.5 \mu\text{m}$.

CIGALE builds up galaxy SEDs from UV to radio wavelengths assuming a combination of modules. These allow us to model the star formation history (SFH), the stellar emission using population synthesis models ([Bruzual & Charlot, 2003](#), [Maraston, 2005](#)), nebular lines, dust attenuation (e.g., [Calzetti et al.,](#)

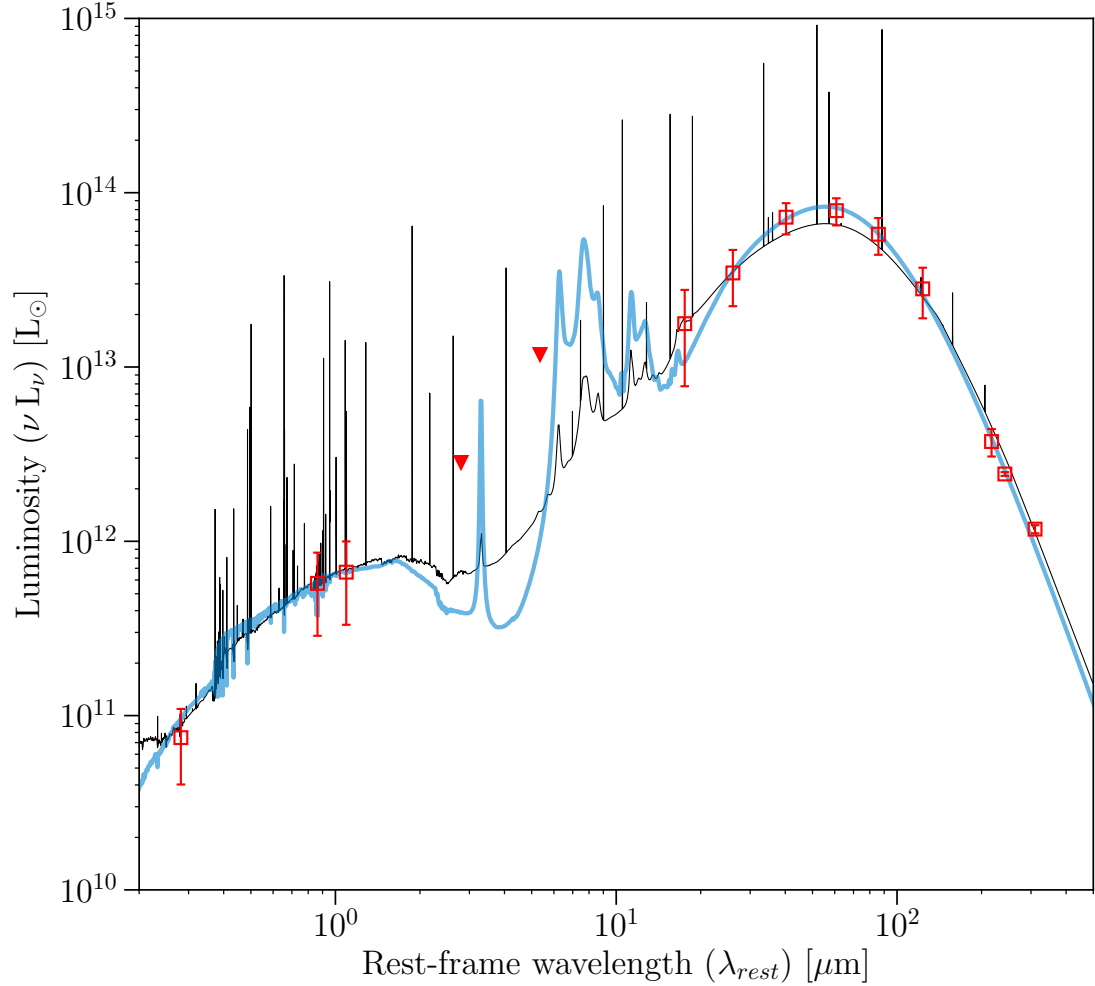


Figure 3.3 Spectral Energy Distribution fit for G12v2.43 using broadband photometry with CIGALE (black) and MAGPHYS (blue). The red squares are the input photometry measurements with associated errorbars. The red solid triangles indicate the upper limits derived from the WISE W3 and W4 bands.

2000), dust emission (e.g., Casey, 2012, Draine & Li, 2007), contribution from an AGN (e.g., Dale et al., 2014, Fritz et al., 2006), and radio emission. The SEDs are built while maintaining consistency between UV dust attenuation and far-IR emission from the dust. To model the star formation history, we employ a delayed star formation history prescription used to model high-z star-forming galaxies (e.g., Ciesla et al., 2016) with the dust attenuation from Calzetti et al. (2000), and the dust emission models from Draine & Li (2007). Finally, CIGALE

performs a probability distribution function analysis for our specified model parameters, and obtains the likelihood-weighted mean value for each parameter.

MAGPHYS uses a Bayesian approach to constrain galaxy-wide physical properties, including the star formation rate, stellar and dust masses, and contributions from both, hot and cold dust components of the ISM. It builds a large library of reference spectra with different star formation histories (using stellar population synthesis models from [Bruzual & Charlot, 2003](#)) and dust attenuation properties (using models from [Charlot & Fall, 2000](#)). Similar to CIGALE, it also ensures energy balance between the optical and UV extinction and the FIR emission. Both CIGALE and MAGPHYS have internal filter libraries, that use instrumental response curves to perform color correction.

However, the MAGPHYS package does not allow for a possible AGN contribution to the overall SED fit. In order to explore the presence of a hidden AGN in G12v2.43, we used the AGN module in CIGALE with templates from [Fritz et al. \(2006\)](#), to estimate a parameter that constrains the fraction of observed emission that could be due to an AGN. We compare the resulting best-fit models and derived parameters from both CIGALE and MAGPHYS. We find that the AGN contribution is negligible in G12v2.43 and the observed SED is well explained by a dust-obscured starburst. For such heavily obscured system, extinction due to a large column of dust may lead to corrections that could be important for deriving physical properties (e.g., [Uzgil et al., 2016](#)). Using a modified blackbody approximation for the dust emission, we estimate the wavelength $\lambda_0 = c/\nu_0$ where the optical depth $\tau_\nu = (\nu/\nu_0)^\beta$ reaches unity for G12v2.43. In doing so, we make the following assumptions, the resolved dust

continuum size from the SMA observations is used to measure the source solid angle, the dust emissivity spectral index β is fixed to 1.5, and that the correction due to contrast against the CMB is negligible. We find $\lambda_0^{rest}=32\pm 8\ \mu\text{m}$ and assuming the dust is well mixed in the medium, the correction to the reported [O III] $88\ \mu\text{m}$ line luminosity in Section 3.3 would be $\sim 11\%$, well within the reported uncertainty. The SEDs and their best fits from both CIGALE and MAGPHYS are plotted in Figure 3.3. Both SED fits are consistent within the errors and the corresponding best fit parameters are listed in Table 3.3. L_{IR} is calculated by integrating under the best-fit SED between $\lambda_{rest} = 8 - 1000\ \mu\text{m}$ and L_{FIR} by integrating over $\lambda_{rest} = 42.5 - 122\ \mu\text{m}$.

3.5.2 Constraining the Stellar Population

We showed in Section 3.3.1 that assuming the [O III] line emission we detect in G12v2.43 arises from HII regions formed by stars, then the young stellar population likely contains $5 \times 10^6 (\frac{10}{\mu})$ upper main sequence stars. In 3.5.1, with the help of the broadband SED, we find that indeed the luminosity of the source is dominated by star formation activity and argue against the presence of an AGN. Also, as a part of the SED modeling exercise, we build a stellar population model to constrain the star formation rate and stellar mass. The best fit models suggest a stellar mass content of G12v2.43 to be $7.7 \times 10^{10} (\frac{10}{\mu}) M_{\odot}$ with about 12% of that mass attributed to an ongoing starburst event with an average star formation rate, $\text{SFR}=916 (\frac{10}{\mu}) M_{\odot} \text{ yr}^{-1}$. As mentioned in Section 3.5.1, the uncertainty of assigning the flux from Spitzer/IRAC photometry to the high redshift source dominates the errors in determining the total stellar mass as reported in Table 3.3. We also find that the predicted [OIII] $88\ \mu\text{m}$ line luminosity from the

Table 3.3. Derived Physical Properties of G12v2.43

Quantity	Value	Unit	Notes/Ref
Stellar Mass (M_{\star})	$7.7^{+1}_{-4} \times 10^{10}$	$(\frac{10}{\mu}) M_{\odot}$	(1)
IR Luminosity (L_{IR})	$1.3 \pm 0.1 \times 10^{13}$	$(\frac{10}{\mu}) L_{\odot}$	(1), (2) ^a
Far-IR Luminosity (L_{FIR})	$8.3 \pm 0.9 \times 10^{12}$	$(\frac{10}{\mu}) L_{\odot}$	(1), (3) ^b
[O III] ₈₈ Luminosity (L_{OIII})	$7.1 \pm 0.9 \times 10^9$	$(\frac{10}{\mu}) L_{\odot}$	(4)
Dust Temperature ($T_{\text{dust,MBB}}$)	$49.6^{+5.6}_{-3.6}$	K	(1)
Dust Temperature ($T_{\text{dust,Draine}}$)	34 ± 1	K	(5)
Star Formation Rate (SFR)	916^{+88}_{-206}	$(\frac{10}{\mu}) M_{\odot} \text{ yr}^{-1}$	(1)
Dust Mass (M_{dust})	$5.4 \pm 0.9 \times 10^8$	$(\frac{10}{\mu}) M_{\odot}$	(1)
Ionized Gas Mass ($M_{\text{min}}^{\text{H}^+}$)	$2.0 \pm 0.3 \times 10^8$	$(\frac{10}{\mu}) M_{\odot}$	(4)
Ionized Gas Density (n_{H^+})	<610	cm^{-3}	(4)
Molecular Gas Mass ($\alpha_{\text{CO}}=0.8$)	$1.2 \pm 0.7 \times 10^{10}$	$(\frac{10}{\mu}) M_{\odot}$	(2)
Molecular Gas Mass (Genzel et al. 2015)	$6.1 \pm 0.7 \times 10^{10}$	$(\frac{10}{\mu}) M_{\odot}$	(6)

Note. — (1) This work, parameter derived from best-fit SED with MAGPHYS; (2) Harris et al. (2012); (3) $L_{\text{FIR}}=8.9 \times 10^{13} L_{\odot}$,^b Wardlow et al. (2017); (4) This work, based on [O III] 88 μm line emission reported in Section 3.3.1 and discussion in Section 3.4.4; (5) This work, based on $U_{\text{min}}=24$, from CIGALE dust emission best-fit model; (6) Based on the method outlined by Genzel et al. (2015) using a variable metallicity dependent α_{CO} .

^a In both cases the IR luminosity is calculated between 8-1000 μm

^b L_{FIR} reported by (3) based on luminosity integrated over 40-500 μm

nebular emission component of the best-fit model, $L_{[\text{OIII}]}=(10 \pm 4) \times 10^9 (\frac{10}{\mu}) L_{\odot}$ is in agreement with the observed line luminosity reported in Section 3.3.1, adding confidence to our interpretation that G12v2.43 hosts a significant young stellar population.

Another way to look at the number and mass of the upper main sequence stars is to estimate them using an initial mass function assuming a star formation rate. Here, we assume a Salpeter IMF of the form $\Phi(M) \propto M^{-2.35}$ with

an upper mass cutoff of $100 M_{\odot}$ and a lower mass cutoff of $1 M_{\odot}$. In a continuous star formation scenario, the equilibrium number for O-stars with mass $> 34.4 M_{\odot}$ (O5.5 or higher) could be estimated as follows:

Total *mass* of stars formed in an year = SFR,

$$SFR = \int_1^{100} M \times k M^{-2.35} dM \quad (3.2a)$$

Here k is an arbitrary constant of proportionality.

$$\Rightarrow k = \frac{SFR}{\int_1^{100} M^{-1.35} dM} = \frac{SFR}{2.287} \quad (3.2b)$$

Total *number* of stars formed per year with $M > M_{low}$,

$$\# \text{ of Stars, } N = \int_{M_{low}}^{100} k M^{-2.35} dM \quad (3.2c)$$

If the main sequence lifetime of star with mass M_{low} is τ_{MS} , then their equilibrium number would be,

$$N_{Eq} \approx \frac{SFR}{2.287} \int_{M_{low}}^{100} M^{-2.35} dM \times \tau_{MS} \quad (3.2d)$$

For an O5.5 star, where the main sequence lifetime for the star is $\tau_{MS} = 4.9 \text{ Myr}$ (Ekström et al., 2012), thus the equilibrium number of O5.5 or higher stars in a continuous star formation scenario with a $SFR=916 M_{\odot} \text{ yr}^{-1}$ would be $\sim (916/2.287) \times 4.76 \times 10^{-3} \times 4.9 \times 10^6 = 9.3 \times 10^6$ or about twice the current number. This simple result demonstrates that the star formation event, if sustained at its present rate, must be less than 5 million years old.

Starburst99 models (Leitherer et al., 1999) for continuous star formation utilize the same constraints and provide an independent comparison for the quantities derived here. The Starburst99 models count the number of O-stars as those with $T_{eff} > 30,000 \text{ K}$, which would correspond to all stars above

$\sim 15.6 M_{\odot}$ (Martins et al., 2005). But, a star of spectral class O5.5 or earlier has a mass $M > 34.4 M_{\odot}$, and such stars account for only about 28% of the total number of stars considered to be O-stars by the Starburst99 models. In the continuous star formation scenario forming $1 M_{\odot} \text{ yr}^{-1}$, Starburst99 reports 20,800 O-stars after 4.9 Myrs. To get the estimated number of O-stars, $(5 \times 10^6 / 0.28) \sim 1.8 \times 10^7$, the Starburst99 models would require an effective star formation rate of $859 M_{\odot} \text{ yr}^{-1}$, which is consistent with our estimated SFR of $916 M_{\odot} \text{ yr}^{-1}$ within errors.

3.5.3 Conditions of Interstellar gas and dust

Here we will compare the interstellar dust and gas content of G12v2.43 using available data, particularly gas mass reported by Harris et al. (2012) using $^{12}\text{CO}(1-0)$ line observations, the dust mass estimate from the SED, and the molecular gas mass estimates using the method described in Scoville et al. (2016) and Genzel et al. (2015). The continuum measurements on the Rayleigh-Jeans (R-J) tail can be used to independently estimate total molecular gas mass using the method described in Scoville et al. (2016). The main caveat for using the continuum to derive molecular gas mass estimates using this technique is that the continuum data point should be well on the R-J tail and not near the peak of the dust blackbody emission. Here, we only use the continuum points longward of $890 \mu\text{m}$ (observed frame) or $> 210 \mu\text{m}$ rest-frame at $z=3.127$ (see Table 3.1). We use the relationship between total molecular gas mass in the galaxy

and continuum flux density observed on the R-J tail by [Scoville et al. \(2016\)](#),

$$M_{\text{mol}} = 1.78 \left(\frac{S_\nu}{\text{mJy}} \right) \left(\frac{d_L}{\text{Gpc}} \right)^2 \left(\frac{\nu_{\text{obs}}}{\nu_{850\mu\text{m}}} \right)^{-3.8} (1+z)^{-4.8} \left(\frac{\Gamma_0}{\Gamma_{\text{RJ}}} \right) 10^{10} M_\odot, \quad (3.3a)$$

$$\text{where, } \Gamma_{\text{RJ}}(z, T_d, \nu_{\text{obs}}) = \frac{h\nu_{\text{obs}}(1+z)/kT_d}{e^{h\nu_{\text{obs}}(1+z)/kT_d} - 1}, \quad (3.3b)$$

$$\text{and, } \Gamma_0 = \Gamma_{\text{RJ}}(0, 25 \text{ K}, \nu_{850\mu\text{m}}) = 0.7$$

It has been often suggested that the temperature of the cold dust component in galaxies derived using modified Blackbody models tends to be biased higher when compared to the expected temperature of the bulk of the dust mass present in the ISM (e.g., [Draine & Li, 2007](#), [Scoville et al., 2016](#)). As part of the SED modeling we used the dust models from [Draine & Li \(2007\)](#) to constrain the distribution of the ambient interstellar radiation field intensity (U). The models further estimate an average dust temperature based on the minimum intensity of radiation field as $T_{\text{dust}} = 20 U_{\text{min}}^{1/6} \text{ K}$ ([Draine, 2010](#)), which for G12v2.43 results in $T_{\text{dust}} = 34 \text{ K}$ based on $U_{\text{min}} = 24 \pm 4$.

In order to be closest to the calibration derived by [Scoville et al. \(2016\)](#), we use the above dust temperature along with the $896 \mu\text{m}$ continuum observations in Eq(3.3a), to estimate the molecular gas mass in G12v2.43 to be $M_{\text{mol}} = 1.8 \times 10^{11} \left(\frac{10}{\mu} \right) M_\odot$. For comparison, [Harris et al. \(2012\)](#) reported a total molecular gas mass, $M_{\text{mol}} = (1.2 \pm 0.7) \times 10^{10} \left(\frac{10}{\mu} \right) M_\odot$ based on observations of the $^{12}\text{CO}(1-0)$ line luminosity and assuming a CO-to- H_2 conversion factor, $\alpha_{\text{CO}} = 0.8 M_\odot (\text{K-km s}^{-1} \text{ pc}^2)^{-1}$. This choice of α_{CO} is typically used for local ULIRGs and to compare molecular mass estimates between high-z SMGs. Even if we use the ‘‘luminosity-weighted’’ dust temperature derived from the SED fit, $T_{\text{dust}} = 49.6 \text{ K}$ in Eq(3.3a), we estimate a molecular gas mass of $1.3 \times 10^{11} \left(\frac{10}{\mu} \right) M_\odot$.

We also verify that we get similarly high molecular gas mass estimates using the continuum data points reported by [Yang et al. \(2016\)](#) at 1 and 1.25 mm (240 and 300 μm respectively in the rest frame of G12v2.43). We apply the appropriate correction factors Γ_{RJ} as defined in Eq(3.3b), that accounts for deviation from the default calibration at 850 μm due to redshift and dust temperature, and estimate the molecular gas mass as $(1.6 - 2) \times 10^{11} (\frac{10}{\mu}) M_{\odot}$. Therefore, using the submm dust continuum method outlined by [Scoville et al. \(2016\)](#), we find the estimated molecular gas mass to be 10-16 times larger than the molecular gas mass derived using the $^{12}\text{CO}(1-0)$ line observations with a ULIRG-like conversion factor of $0.8 M_{\odot} (\text{K-km s}^{-1} \text{pc}^2)^{-1}$.

We derive a total dust mass of, $M_{\text{dust}} = (5.4 \pm 1) \times 10^8 (\frac{10}{\mu}) M_{\odot}$ from the best-fit SED model. [Genzel et al. \(2015\)](#) provide a relationship to estimate the dust mass using star formation rate and modified dust blackbody temperature,

$$M_{\text{dust}} = 1.2 \times 10^{15} \left(\frac{\text{SFR}}{M_{\odot} \text{ yr}^{-1}} \right) \left(\frac{T_{\text{dust}}^{\text{MBB}}}{\text{K}} \right)^{-5.5}, \quad (3.4)$$

Using, $T_{\text{dust}}=49.6 \text{ K}$ and $\text{SFR}=916 M_{\odot} \text{ yr}^{-1}$ in Eq(3.4), we find $M_{\text{dust}}=5.1 \times 10^8 M_{\odot}$ which is consistent with the total dust mass derived from the best fit SED. Now, we compare the dust-to-gas mass ratio using the different molecular gas mass estimates with a metallicity dependent dust to gas ratio from [Leroy et al. \(2011\)](#),

$$\log_{10} \delta_{dg} = \log_{10} \left(\frac{M_{\text{dust}}}{M_{\text{mol}}} \right) = -2 + 0.85 \times (12 + \log_{10}[\text{O}/\text{H}] - 8.67), \quad (3.5)$$

If we use the $^{12}\text{CO}(1-0)$ measurement along with a ULIRG like conversion factor, we find that G12v2.43 has a metallicity, $12+\log[\text{O}/\text{H}]=9.4$, whereas, us-

ing the estimate of the molecular gas mass using the R-J continuum, we find a metallicity, $12+\log[\text{O}/\text{H}]=8.2$. In contrast, using a fitting function for metallicity by combining the stellar mass-metallicity relation at different redshifts as given in Eq(12) by [Genzel et al. \(2015\)](#), we find a metallicity, $12+\log[\text{O}/\text{H}]=8.6\pm 0.1$. Using this estimate of metallicity in Eq(3.5), we find a $\delta_{dg}=(0.8-1)\times 10^{-2}$. This would imply a total molecular gas mass of $M_{\text{mol}}=6.1\pm 0.7 \times 10^{10} \left(\frac{10}{\mu}\right) M_{\odot}$ and an implied $\alpha_{\text{CO}} \approx 4 M_{\odot} (\text{K-km s}^{-1} \text{pc}^2)^{-1}$, quite similar to that observed in the Milky Way. For a galaxy undergoing a vigorous starburst event of the likes we suggest for G12v2.43, the filling fraction of star-forming, denser, gas could be higher than the typical local ULIRG values. [Downes et al. \(1993\)](#) parametrized the conversion factor, $\alpha_{\text{CO}} \propto \sqrt{n}/T_b$, where n is the the average H_2 density of the gas clouds and T_b is the intrinsic brightness temperature of the $^{12}\text{CO}(1-0)$ line. A higher volume-averaged density of the medium could account for the relatively high α_{CO} value suggested here. We use this estimate of the molecular gas mass for further discussion.

Even though the various molecular gas mass estimates vary significantly, the implied baryonic gas fraction $\left(f_{\text{gas}} = \frac{M_{\text{mol}}}{M_{\text{mol}}+M_{\text{stellar}}}\right)$, is $f_{\text{gas}}=0.44_{-0.30}^{+0.23}$, is similar to observed gas fractions in gas-rich high- z SMGs (e.g., [Tacconi et al., 2013, 2017](#)). The high gas fraction and yet a relatively short gas depletion time-scale of 66 Myrs, along with the enormous star formation rate, agree with our understanding of the star formation activity in G12v2.43. Specifically, that it is undergoing a star formation episode building up its stellar mass and is currently above the star-forming main sequence at $z\sim 3$ ([Speagle et al., 2014](#)).

3.5.4 Is G12v2.43 strongly lensed?

With the high signal-to-noise, SMA continuum observations (FWHM: $0''.93 \times 0''.63$), we derive the de-convolved source size of the dust emitting disk as $(0''.7 \pm 0''.1) \times (0''.6 \pm 0''.1)$, which corresponds to a physical size of (5.6×4.5) kpc or $r_{\text{dust}} \sim 5$ kpc. In terms of area, this is about 7 times larger than the typical size of the dust disk, $r_{\text{dust}} \sim 1.8$ kpc, found by [Hodge et al. \(2016\)](#) in a resolved study of sixteen $z \sim 2.5$ SMGs. As gravitational lensing spreads the intrinsic source over a larger area, a lensing magnification factor of $\mu \sim 7$ could make G12v2.43's dust disk consistent with those observed in other high- z SMGs.

The observed line widths for spectral lines tracing various transitions of CO and H₂O in G12v2.43 are about $\sim 225 \text{ km s}^{-1}$. As a comparison, in a study of $J > 2$ CO line observation in DSFGs presented in [Bothwell et al. \(2013\)](#), the mean value for CO line widths was found to be $(510 \pm 80) \text{ km s}^{-1}$. This might indicate that G12v2.43 is either an almost face-on disk or not an intrinsically massive galaxy. As the CO line emission has been used to study the mass and kinematics of galaxies, [Harris et al. \(2012\)](#) suggested that there should be a ‘‘Tully-Fisher’’-like relationship between the CO line width and the intrinsic line luminosity. Based on the bright ¹²CO(1-0) line detection and the small line width they suggested a lensing magnification factor $\mu \sim 17 \pm 11$ for G12v2.43.

We can also estimate the CO emitting size, even without spatially resolved observation, assuming that the CO emission is optically thick. Following Eq(2) from [Solomon & Vanden Bout \(2005\)](#),

$$L'_{\text{CO}} = 1.13 (T_{\text{ex}} - T_{\text{CMB}}(z)) \Delta v_{\text{FWHM}} r_{\text{CO}}^2 \quad (3.6)$$

The temperature of the CMB at $z=3.127$ is $T_{\text{CMB}} = 11.2\text{K}$. The first rotational transition of the ^{12}CO line only lies about 5.51K above ground and the molecules can be easily excited by the ambient radiation field and by collisions in the gas. We apply an excitation temperature of $T_{\text{ex}}=30\text{K}$, assuming that it should be higher than the background CMB temperature and perhaps lower than the dust temperature, $T_{\text{dust}}=50\text{K}$. Now, with the observed line luminosity, $L'_{\text{CO}}=1.5\times 10^{11}\text{K}\cdot\text{km s}^{-1}\text{pc}^2$ and measured line FWHM, $\Delta v_{\text{FWHM}}=225\text{km s}^{-1}$, we derive a $r_{\text{CO}} = 5.6\text{kpc}$, which is about the same as the size of the dust emitting region derived above. We note that the CO emitting size estimate is weakly dependent on our choice of T_{ex} .

For a simple rotating disk model following [Neri et al. \(2003\)](#), the dynamical mass of the system can be estimated as,

$$M_{\text{dyn}} \sin^2 i = 2.33 \times 10^5 \left(\frac{\Delta V}{\text{km s}^{-1}} \right)^2 \left(\frac{r}{\text{kpc}} \right) M_{\odot}, \quad (3.7)$$

where $i=\cos^{-1}(\frac{4.5}{5.6})=36.5^\circ$ is the inclination angle estimated from the resolved dust continuum, ΔV is the CO line velocity dispersion in km s^{-1} ($=\text{FWHM}/2\sqrt{2 \ln 2}$), and r is the disk radius in kpc as derived above. We estimate the dynamical mass of the galaxy to be, $M_{\text{dyn}}=3.4\times 10^{10} M_{\odot}$. Since this estimate of the dynamical mass is at least 2 times smaller than either our estimates for the stellar mass or the gas mass, our assumption that the observed ellipticity reflects inclination is suspect. In order to make a fair comparison between the estimates of dynamical mass, molecular gas mass, and stellar mass, we need to consider how the lensing magnification factor (μ) and the choice of CO-to- H_2 conversion factor (α_{CO}) affect our measurements. We expect the dynamical mass of the system to be larger than the estimates of either the stellar

mass or the molecular gas mass. The apparent spatial size scales as $r \propto \sqrt{\mu}$, but the apparent luminosity (CO and stars) scales as $L \propto \mu$. The choice of the CO-to-H₂ conversion factor (α_{CO}) only changes the estimate for the molecular gas mass, $M_{\text{mol}} \propto \alpha_{\text{CO}}$. If we assume the source is unlensed (largest r , M_{dyn}) and use $\alpha_{\text{CO}}=0.8$ (lowest estimate of the molecular gas), this still results in $M_{\text{mol}} \sim 3.5 \times M_{\text{dyn}}$. Without changing the α_{CO} (increasing α_{CO} , widens the discrepancy), in order to match the dynamical mass to the molecular gas mass, we would need to increase the magnification factor to $\mu=12.5$. A less inclined orientation would bring the estimates closer together, but a simpler explanation for the observed line and continuum luminosities could be amplification due to the affect of gravitational lensing.

3.6 Results & Conclusions

We have presented sensitive ground based THz spectroscopy with ZEUS-2 at the APEX Telescope, detecting the [OIII] 88 μm line in G12v2.43, a high redshift sub-millimeter galaxy at $z=3.127$. The luminosity in the line is, $7.1 \times 10^9 (\frac{10}{\mu}) L_{\odot}$, which indicates the presence of a large number of upper main sequence O-stars and allows us to constrain the number of ionizing photons available. In the high density, high temperature limit, we derive that the minimum mass of ionized gas required to support the observations would be $2.8 \times 10^8 (\frac{10}{\mu}) M_{\odot}$ or about 0.33% of the estimated total molecular gas, $M_{\text{mol}} = 6.1 \times 10^{10} (\frac{10}{\mu}) M_{\odot}$.

The upper limit from the SPIRE spectrum on the [CII]/FIR ratio, $\leq 0.4\%$ would be consistent with a compact starburst, but the small velocity width and single Gaussian profile in CO and H₂O lines argue against a major merger as

the source of the observed [CII]/FIR line to continuum ratio. We also constrain the ionized gas density to be, $n_{\text{H}^+} < 610 \text{ cm}^{-3}$ using the limit for the [OIII] $52 \mu\text{m}$ line from the SPIRE spectrum along with our detection of the [OIII] $88 \mu\text{m}$ line.

Using rest-frame UV to mm wavelength observations, we constrain a broadband SED for the source and rule out any significant contribution by an obscured AGN. We find, using both the SED and extrapolating the equivalent number of $5 \times 10^6 \left(\frac{10}{\mu}\right)$ O5.5-O3 stars estimated using the the observed [OIII] line emission, that the on-going star formation event in G12v2.43 has contributed up to $0.55-1 \times 10^{10} \left(\frac{10}{\mu}\right) M_{\odot}$ to its stellar mass, i.e., up to 7-12% of the total stellar mass, $M_{\text{stellar}} = 7.7 \times 10^{10} \left(\frac{10}{\mu}\right) M_{\odot}$.

A gas fraction of $f_{\text{gas}} = 0.44_{-0.30}^{+0.23}$, indicates that the galaxy has an abundant supply of gas to sustain star-formation over the next 66 million years, effectively doubling its stellar mass and end up on the star-forming main sequence at $z \sim 3$.

We also detect rest-frame near-UV emission in the $1.1 \mu\text{m}$ HST/WFC3 image, consistent with the centroid of the dust emission seen in the SMA $896 \mu\text{m}$ continuum image, it appears patchy and there is another source $\sim 1''$ away along the NE-SW axis but no obvious signature of gravitational lensing like extended arcs or an Einstein ring are seen. The apparent brightness of the galaxy suggests that it could be lensed and the low dynamical mass estimate is consistent with the lensing scenario. Higher resolution observations are required to reveal the true nature of this otherwise apparent gargantuan, specifically to understand the role gravitational lensing plays in amplifying the observed emission and uncovering the intrinsic nature of G12v2.43.

CHAPTER 4

ZOOM-IN TO GALAXY ASSEMBLY: A RESOLVED STUDY OF A HIGHLY MAGNIFIED GALAXY AT $z \sim 4.2$ THROUGH FAR-INFRARED RADIATION

4.1 Abstract

We present a comprehensive study of the physical conditions of the star-forming interstellar medium of a highly magnified galaxy, SPT-S J041839-4751.8, hereafter SPT0418-47, at a redshift, $z=4.225$ using far-infrared, fine-structure lines of [O III], [C II] and [N II] observed with the 2nd generation Redshift (z) and Early Universe Spectrometer (ZEUS-2) on the Atacama Pathfinder Experiment (APEX) Telescope and the Atacama Large Millimeter/sub-millimeter Array (ALMA). The source averaged $L_{[\text{OIII}]} / L_{[\text{NII}]}$ of ~ 55 , can be reproduced by an ionization parameter, $\log U \sim -2$ based on modeling of emission from ionized gas and the average $L_{[\text{CII}]} / L_{[\text{NII}]}$ ratio of ~ 22 across the source, suggests that on average, only about 14% of the [C II] emission is associated with ionized gas. This ratio varies significantly across the source, between $\sim 13-39$ ($f_{[\text{CII}]}^{\text{PDR}} \sim 77-92\%$). We find a high dust temperature for SPT0418-47, $T_{\text{dust}} = 59 \pm 2$ K. Based on a modified blackbody fit to the source integrated mid-infrared to millimeter dust spectral energy distribution, we conclude the dust emission is optically thick out to $200 \mu\text{m}$. Our lens model for the $200 \mu\text{m}$ dust continuum is in remarkable agreement with previous models and we find the dust emitting source to be, $r_{\text{FWHM}} = 1.2 \pm 0.01$ kpc ($0''.18 \pm 0''.002$) in size. The [C II] and [N II] line emission shows significant structure in velocity profiles azimuthally and radially around the ring, with the N-W part of the ring showing a clear double-horned profile,

suggesting ordered rotation. A third velocity component, peaking at velocity of the dip in the double horn profile, is distinctly present only in the N-E part of the ring, which might be originating from an interacting component. Combined together these observations present an interesting scenario for SPT0418-47 with the presence of vigorous star-formation in a well-developed ordered 2 kpc wide rotating disk and perhaps hints at the presence of an interacting companion.

4.2 Introduction

The study of formation and evolution of galaxies in the Universe has seen major progress in the last two decades. Observational evidence has allowed us to confidently characterize the time evolution of the stellar mass assembly as the cosmic star formation rate density evolved by two orders of magnitude from within the era of reionization ($6 < z < 10$) to the era of galaxy assembly ($1 < z < 4$) (Madau & Dickinson, 2014). It is now well understood that the increased star-formation rate density during the epoch of galaxy assembly is created and sustained by the presence of massive gas reservoirs. The nature of star-formation, whether triggered due to a major merger or secular across the entire disk of a galaxy, is intricately related to the time-scales, efficacy, and coupling of feedback due to massive star formation, injection of energy from supernova explosions, and mechanical and radiative feedback from an active galactic nuclei. However, the mechanism to build-up and replenish the gas reservoirs fueling star-formation is not well understood. It is not unreasonable to suggest a scenario in which, as the host galaxies assemble their dark matter halos, they would funnel gas from the cosmic web into the circum-galactic medium, which in turn would allow replenishment of the gas required to sustain the prodigious

amounts of star-formation observed. The most massive of these galaxies might assemble the most massive halos in the early Universe and could reside in an over-dense environment, forming nodes along the structure of the cosmic web. Such an environment would be ripe for merger activity to follow and lead to the hierarchical scenario of galaxy assembly.

Within this broad brush picture of galactic assembly and evolution, spectroscopic observations provide vital constraints on the physical conditions of the interstellar medium (ISM) in host galaxies. The role of massive stars in galaxies is crucially important and has been the focus of many studies historically. In the current day Universe, these stars are few and form only a small fraction of the stellar populations, but their influence on the environment in which they reside and the observed spectrum of host galaxies, forms the basis of nebular diagnostics used to characterize star-formation activity in galaxies near and far. Most metals are created in the cores of these massive stars, and as these stars evolve off the main sequence they disperse the products of the fusion furnace into the neighboring interstellar medium through stellar winds and supernova explosions. In turn, this injection of energy, through radiative and mechanical feedback, and the presence of metals and their ions themselves directly affect subsequent star-formation in the vicinity.

These stars are also the dominant sources of ionizing radiation and power the HII regions and the leakage of ionizing radiation is thought to sustain the extended diffuse ionized medium in galaxies. The strength of the emission lines depends directly on the properties of the emitting gas, like abundance (of various ions) and density, and the source of ionizing radiation, like luminosity and spectral energy distribution of photons. Using ratios of various such lines aris-

ing from different metals, their ionization states, abundances and densities can be quantitatively studied to probe the input stellar flux sustaining the observations and constrain the upper mass end of the stellar populations in the host galaxies. As we go back in cosmic time towards the epoch during which galaxies assembled most of their stellar mass, the relative importance of the stellar population arising from on-going starformation activity will grow in importance and be less susceptible to the old stellar populations that could potentially increase the intensity of the radiation field but can not provide enough high energy photons.

The far-infrared lines of important metal ions present in the interstellar medium (e.g. [C II] 158, [N II] 122 & 205, [O III] 88 & 52 μm) are important coolants of the gas, and excellent probes of physical conditions like the density of the emitting gas and the incident radiation field and hence the source powering the observed luminosity of the lines – a burst of star formation activity or accretion onto a super-massive black hole. Studies of these lines from a variety of physical conditions in our own Galaxy and in the nearby Universe (e.g., [Brauhert et al., 2008](#), [Carral et al., 1994](#), [Colbert et al., 1999](#), [Cormier et al., 2015](#), [Díaz-Santos et al., 2017](#), [Farrah et al., 2013](#), [Graciá-Carpio et al., 2011](#), [Herrera-Camus et al., 2018](#), [Lord et al., 1996](#), [Stacey et al., 1991](#)) provides a stepping stone to their application to high-redshift galaxies. Opaqueness of the Earth's atmosphere to THz radiation has significantly limited our study of the far-IR fine structure line emission beyond $z > 0.2$ but at $z > 1$ the lines are redshifted to longer wavelengths and can fall within telluric windows that allow sub-mm/mm radiation to pass through the Earth's atmosphere and make observations with state-of-the-art ground-based receivers on sub-mm/mm telescopes possible. The advent of ALMA has propelled the pace of such studies, with the [C II] line being the pri-

mary work horse for discovery. We are still limited to a handful galaxies where multiple far-infrared lines have been observed providing insights to both the host stellar populations, and the physical conditions of the gas.

Leveraging the rapid advancement in sensitivity and the ability to multiplex the readout of a large number of transition-edge sensing (TES), direct detection bolometers, we have constructed the second generation redshift(z) and Early Universe Spectrometer (ZEUS-2). ZEUS-2 is a long-slit, grating spectrometer optimized for detecting broad (few 100 km s^{-1}) spectral lines from distant galaxies as they are redshifted into the sub-mm telluric windows (Ferkinhoff et al., 2012, Parshley et al., 2012). The long slit on the sky allows for up to nine spatial positions to be observed simultaneously, while the grating, operating in the 3rd, 4th, 5th and 9th order allows simultaneous access to the the telluric windows around $600 \mu\text{m}$, $450 \mu\text{m}$, $350 \mu\text{m}$ and $200 \mu\text{m}$ respectively. ZEUS-2 houses two physical arrays ($350+450 \mu\text{m}$, $215+645 \mu\text{m}$) of superconducting Transition Edge Sensed (TES) bolometer pixels with backshorts optimized for achieving very high detector quantum efficiency at the operating wavelengths. The blazed grating provides a resolving power, $R \sim 500$ for the third order, $R \sim 1000$ for the fourth and fifth order and $R \sim 1300$ for the ninth order and an instantaneous bandwidth of $\sim 4000 \text{ km s}^{-1}$ for each spatial row of detector pixels. Using ZEUS-2 and its predecessor, ZEUS we have detected more than two dozen galaxies in far-IR fine-structure line emission at redshifts from 1 to 5 primarily focusing on $158 \mu\text{m}$ [C II] line studies (Brisbin et al., 2015, Ferkinhoff et al., 2014, Hailey-Dunsheath et al., 2010, Stacey et al., 2010).

The [O III] lines are nearly as bright as [C II] in most nearby galaxies, and can be even brighter in low metallicity systems (Cormier et al., 2015) so it can be a

readily observed astrophysical probe in the early Universe. Its brightness also makes it a good tool for determining redshifts of galaxies at $z > 8$, as was successfully demonstrated by a recent confirmation of a suspected lensed source at $z = 9.11$ (Hashimoto et al., 2018a). It takes 35 eV photons to photo-ionize O^+ to O^{++} , so this line is used to track the numbers of early-type stars in star-formation dominated systems. The line was first detected in high redshift systems with ZEUS (Ferkinhoff et al., 2010). The current sample of [O III] detections in high redshift dusty star-forming galaxies consists of three detections between $z \sim 2.8-4$ using ZEUS and ZEUS-2 (Ferkinhoff et al., 2010, 2011, Vishwas et al., 2018), three more systems between $z \sim 1.7-3$ have reported detections with Herschel-SPIRE (Lamarche et al., 2018, Rigopoulou et al., 2017, Valtchanov et al., 2011) and in five $z > 6$ (3/5 quasar host galaxies) with ALMA (Hashimoto et al., 2018b, Marrone et al., 2017, Walter et al., 2018).

Since it only takes 14.5 eV photons to photo-ionize N to N^+ , the [N II] lines, when combined with the [O III] lines can be a strong indicator of the hardness of the stellar radiation fields if one assumes an N/O ratio (e.g., Ferkinhoff et al., 2011). Here, we report observations of bright far-infrared fine-structure lines of [O III] at $88 \mu\text{m}$, [C II] at $158 \mu\text{m}$ and [N II] at $205 \mu\text{m}$ lines in a lensed star-forming galaxy, SPT0418-47 at $z = 4.2248$. Each of the lines tracks the physical conditions of the emitting gas and is an important coolant of the corresponding phase of the ISM. The combination of the three lines tracks the radiation fields from 11.3 to 35 eV so that stellar radiation fields are constrained as well. We observed the [O III] line with ZEUS-2 on the APEX telescope in the $450 \mu\text{m}$ waveband, and also present here ALMA observations of the [C II] and the [N II] line revealing line emission spread across a spatially resolved Einstein ring.

SPT0418-47 (RA: 04:18:39.683 Dec: -47:51:52.711, J2000) was selected as a candidate high redshift source based on the observed flux density at millimeter wavelengths as detected in a large scale survey of the southern sky by the South Pole Telescope (SPT [Carlstrom et al., 2011](#)). The Atacama Large Millimeter/submillimeter Array (ALMA) confirmed the lensed nature of the source with 870 μm interferometric imaging, showing emission extended in a near-complete Einstein ring [Vieira et al. \(2013\)](#), and the background galaxy was confirmed to be at high redshift ($z=4.2248\pm 0.0007$) through mm-band spectral scans [Weiß et al. \(2013\)](#). The massive, foreground lens was confirmed to be at a redshift, $z=0.265$ with an optical long-slit grism spectrum taken with the Focal Reducer/low dispersion Spectrograph-2 on the Very Large Telescope (VLT/FORS2). A gravitational lensing model accounting for the galaxy-galaxy lensing based on the observed dust continuum with ALMA was presented by [Hezaveh et al. \(2013\)](#) and later refined with higher resolution observations by [Spilker et al. \(2016\)](#). Along with the large apparent infrared luminosity, SPT0418-47 has been confirmed to host a significant reservoir of molecular gas through $^{12}\text{CO}(2-1)$ observations with the Australia Telescope Compact Array (ATCA) by [Aravena et al. \(2016\)](#) and the First Light APEX Submillimeter Heterodyne (FLASH) receiver on the Atacama Pathfinder Experiment (APEX) telescope [Gullberg et al. \(2015\)](#) showed that it is also a bright emitter in the astrophysically important [CII] 158 μm line.

The organization of this paper is as follows: In Section 4.3 we describe the observations for the far-infrared fine structure lines of [O III], [N II], and [C II] line and the underlying dust continuum. In Section 4.3.3, we compile new and previously reported observations of SPT0418-47 from various archives and the literature. In Section 4.5, we discuss the line ratios of the far-infrared lines and

the derived constraints on the young stellar population, gas density and ionization parameter. We also estimate the fractional contribution of ionized gas to the observed [C II] luminosity and for the first time present a map of the [C II]/[N II] ratio in a high-redshift source. Removing this contribution from the ionized regions to the [C II] line allows us to trace the spatial variation of the interstellar radiation field, G_0 , that is pervasive throughout the molecular and neutral gas. We summarize our results in Section 4.6.

Throughout this paper we assume a flat Λ CDM cosmology with a Hubble constant of $70 \text{ km s}^{-1} \text{ Mpc}^{-1}$, $\Omega_M = 0.3$, and $\Omega_\Lambda = 0.7$, resulting in a luminosity distance of 38.2 Gpc and a linear scale of $6.79 \text{ kpc arcsec}^{-1}$ for SPT0418-47.

4.3 Observations

4.3.1 ZEUS-2/APEX observations of the [O III] $88 \mu\text{m}$ line

We observed SPT0418-47 with ZEUS-2 at the Atacama Pathfinder Experiment (APEX) telescope (Güsten et al., 2006) in 2014 September under excellent weather conditions. The source elevation during the observation was between $60\text{-}65^\circ$ and the precipitable water vapor (PWV) remained stable between 0.29 and 0.3 mm which corresponds to a line of sight transmission of 67% at the line center with a few telluric features in the vicinity of the line.

We observed line emission from the ground state, fine structure transition ($^3\text{P}_1 \rightarrow ^3\text{P}_0$) of doubly ionized oxygen (O^{++}) ions, at $\nu_{rest} = 3393.00624 \text{ GHz}$ ($88.356 \mu\text{m}$) redshifted to $461.6 \mu\text{m}$ based on the redshift, $z = 4.2242$, reported by

Wei et al. (2013). The resolving power of the instrument at 461 μm (in the 4th order of the echelle grating) is $R \sim 1120$. Each spectral pixel covers $\sim 270 \text{ km s}^{-1}$ in velocity space with the array providing an instantaneous coverage of 3700 km s^{-1} . Data was taken in standard chop/nod mode, with 2 Hz chop frequency and a 30'' azimuthal chop-throw. In total, we obtained 1×30 , 2×20 minute integrations with a chop efficiency of 63% giving a total on-source integration time of 22 minutes. To increase spectral coverage, sample the line profile fully and fill-in gaps due to non-functioning pixels, we used three grating settings to move the line center to a different spectral pixel, one for each set of integrations. One spectral pixel at -900 km/s was flagged due to higher noise, which is due to a deep telluric feature.

Pointing and focus observations were taken on the $^{12}\text{CO}(6-5)$ line on NGC 7552 that is $\sim 5^\circ$ from the same track but transits 4 hours earlier than SPT0418-47. The ZEUS-2/APEX beam was measured on Mars at 434 μm as $10''.2 \pm 0''.6$ (FWHM). Gain calibration for spectral pixels was done by chopping an ambient temperature blackbody against cold sky before and after each set of on-source observations and flux calibration was verified with Mars and Jupiter

4.3.2 ALMA Cycle 4 observations

Band 7: [NII] 205 μm line and 200 μm Dust Continuum

We observed line emission from the ground state, fine structure transition ($^3\text{P}_1 \rightarrow ^3\text{P}_0$) of singly ionized nitrogen (N^+), at $\nu_{rest} = 1461.1314 \text{ GHz}$ (205.178 μm), as part of a project, targeted to study the variation of the [C II]/[N II] ratio as a probe of the diffuse, ionized gas in the interstellar medium of high-redshift

galaxies (Brisbin et al. in prep). SPT0418-47 was observed with ALMA on 2016 December 20, under good observing conditions with PWV between 1-1.3 mm during the course of the observations. The correlator was setup such that the expected frequency of the [N II] line center ($\nu_{obs}=279.685$ GHz) would be covered by the two spectral windows, each spanning 1.875 GHz, in the lower sideband of the receiver. The spectral windows overlap each other covering ± 120 km s⁻¹ around the center frequency and provide velocity coverage of ± 1900 km s⁻¹ around the line center. The spectral windows in the upper sideband cover a bandwidth of 3.75 GHz around the continuum at rest-frame 200 μ m.

A total of 44, 12 m antennas were spread over baselines ranging from 15.1 m to 492 m with a maximum recoverable scale of up to $\sim 5''$. The nearby quasar J0439-4522 was observed regularly for amplitude and phase gain calibration. J0538-4405 was used for pointing and as the bandpass calibrator, and J0519-4546 was used for flux calibration for these observations. The flux calibration accuracy is measured within 5% on the phase calibrator but is higher at $\sim 19\%$ for the bandpass calibrator. The total observing time was 31.5 minutes with 15.4 minutes spent integrating on source.

We downloaded the raw data from the ALMA archive and reduced it using the Common Astronomy and Software Application (CASA) version 4.7.2. We ran the data reduction and calibration pipeline manually to avoid automatic flagging of overlapping channels at the edge of the spectral windows covering the spectral line, and carefully flagged baselines that had worse data quality. A single round of phase-only, self-calibration was performed and applied to the data. We created the dust continuum map by collapsing the line-free channels

covering a bandwidth of 6.5 GHz and using natural weighting for imaging. The resulting image had a beam size of $0''.85 \times 0''.60$ (FWHM) with a position angle of 74.8° and a $1-\sigma$ sensitivity of $54 \mu\text{Jy beam}^{-1}$. The line channels were imaged separately to produce a spectral cube $\pm 1850 \text{ km s}^{-1}$ around the line peak, with an average beam size of $0''.89 \times 0''.64$ (FWHM) with a position angle of 71.3° and an average $1-\sigma$ sensitivity of 0.33 mJy/beam in a 50 km s^{-1} bin.

Band 7: [C II] 158 μm line and 160 μm Dust Continuum

Deep ALMA observations to study the presence of dark matter sub-structure through strong lensing measurements targeting SPT0418-47 were available in the ALMA archive (PI: Hezaveh). Here, we include a single execution block of these observations that covers the ground-state, fine structure transition (${}^3\text{P}_{3/2} \rightarrow {}^3\text{P}_{1/2}$) of the singly ionized carbon (C^+) ion, at $\nu_{rest}=1900.5369 \text{ GHz}$ ($157.741 \mu\text{m}$), and the underlying dust continuum. The source was observed with ALMA on 2016 October 25, under good observing conditions with PWV ranging between 0.65-0.75 mm over the duration of the observations. Two spectral windows, each spanning 1.875 GHz, in the upper sideband of the receiver cover the center frequency of the [C II] line ($\nu_{obs}=363.794 \text{ GHz}$), with an overlap of $\pm 50 \text{ km s}^{-1}$, and a total velocity coverage of $\pm 1450 \text{ km s}^{-1}$, around the line center. The spectral windows in the lower sideband cover a bandwidth of 3.75 GHz around the continuum at rest-frame $160 \mu\text{m}$.

A total of 43, 12 m antennas were available with baselines ranging from 18.6 m to 1.4 km with a maximum recoverable scale of $\sim 1''.7$. Nearby source, J0455-4615 and J0439-4522 were observed for amplitude and phase calibration. J0538-4405 was used as the bandpass calibrator and J0519-4546 was used as the

flux calibrator. The total observing time for the execution block was 1 hour out of which 32.5 minutes were spent on the science source.

The data reduction and calibration was carried out in a manner identical to that described in the previous section including a single round of phase-only, self calibration. We created the dust continuum map by collapsing the line-free channels covering a bandwidth of 5.47 GHz and using natural weighting for imaging the raw visibilities. The resulting image had a beam of $0''.18 \times 0''.17$ (FWHM) with a position angle of -87.6° and achieved a $1-\sigma$ sensitivity of $46 \mu\text{Jy beam}^{-1}$ near the phase center. We imaged the line channels separately to create a spectral cube covering $\pm 1400 \text{ km s}^{-1}$ around the line center. The average beam size over the spectral cube was $0''.19 \times 0''.17$ (FWHM) with a position angle of -79.3° . Each channel in the spectral cube is 50 km s^{-1} wide and the $1-\sigma$ noise achieved ranges from $0.49 \text{ mJy beam}^{-1} \text{ ch}^{-1}$ on the long wave end to $\sim 0.70 \text{ mJy beam}^{-1} \text{ ch}^{-1}$ on the short wave end, near the phase center. We'd like to note here that the field center specified for the observations was offset by $4''.9$ from the location of the target on sky. A primary beam correction, ranging from a factor of 1.1 to 1.5 (primary beam sensitivity drops from 91% to 66% over the extent of the source, $\sim 2''.5$), was applied on the flat noise map created after imaging the data in order to estimate the line and continuum flux.

Table 4.1. Photometry Data for SPT0418-47

Wavelength (μm)	Flux Density (mJy)	Instrument
0.472	$22.1 \pm 0.3 \times 10^{-3}$	DECam/g
0.641	$88.4 \pm 0.4 \times 10^{-3}$	DECam/r
0.783	$138.1 \pm 0.7 \times 10^{-3}$	DECam/i
0.926	$180.5 \pm 1.7 \times 10^{-3}$	DECam/z
1.009	$210.2 \pm 4.6 \times 10^{-3}$	DECam/Y
1.39	$275.4 \pm 5.1 \times 10^{-3}$	HST/WFC3 F140W
3.4	$234.7 \pm 6.6 \times 10^{-3}$	WISE/W1
3.6	$223.1 \pm 22.6 \times 10^{-3}$	Spitzer/IRAC1
4.5	$191.8 \pm 20.9 \times 10^{-3}$	Spitzer/IRAC2
4.6	$182.3 \pm 7.4 \times 10^{-3}$	WISE/W2
12	$206 \pm 55 \times 10^{-3}$	WISE/W3
22	< 3.6	WISE/W4
100	< 27	Herschel/PACS
160	45 ± 12	Herschel/PACS
250	127 ± 14	Herschel/SPIRE
350	210 ± 20	Herschel/SPIRE
500	206 ± 20	Herschel/SPIRE
838	114 ± 3	ALMA/Band-7 (357.69 GHz)
870	106 ± 12	APEX/LABOCA

Table 4.1 (continued)

Wavelength (μm)	Flux Density (mJy)	Instrument
1049	72 ± 2	ALMA/Band-7 (285.85 GHz)
1400	33.5 ± 6.4	SPT
2000	7.2 ± 1.5	SPT
2800	2.3 ± 0.4	ALMA/Band-3 (107.03 GHz)
6971	0.145 ± 0.20	ATCA (43 GHz)

Note. — Wavelength/Frequency in observed frame and reported flux density is integrated over the source; All upper limits are $3\text{-}\sigma$; All optical and near-infrared photometry is expected to be dominated by the foreground lensing galaxy, and limits on its sub-mm/mm emission are placed at <0.2 mJy at $838 \mu\text{m}$ and <0.15 mJy at $1049 \mu\text{m}$ based on non-detection in the ALMA data. The DECam observations were retrieved from the Dark Energy Survey Data Release 1, (Abbott et al., 2018); *Herschel* PACS and SPIRE photometry is based on reprocessed data previously reported by Weiß et al. (2013); LABOCA and SPT photometry adopted from Weiß et al. (2013); ATCA flux density adopted from Aravena et al. (2016)

4.3.3 Supporting Observations

The observations included here enable us to create a panchromatic picture of the emission from both the foreground lensing galaxy and the background, high-redshift, lensed source. These observations were taken with various instruments whose beam size on the sky varies from $0''.15\text{-}35''$. The reported flux densities (or limits) are either queried from the official data release products or derived via aperture photometry in the recommended manner for each instrument. These data are summarized in Table 4.1. We will discuss the relative contribution of the individual galaxies to the observed photometry in Section 4.5.3, particularly where the lensing galaxy dominates the emission or where the spatial resolution does not allow us to measure the two separately.

Archival: Hubble Space Telescope WFC3

The field near SPT0418-47 was observed with the Wide-field Camera (WFC3) using the wide near-infrared filter, F140W, centered at $1.4 \mu\text{m}$ for 2811.7 seconds in 2014 May (PI: Vieira, ID: 13614). We obtained the pipeline calibrated images from the Hubble Legacy Archive to investigate the morphology of the lensing galaxy whose redshift was reported by [Hezaveh et al. \(2013\)](#) to be at $z=0.265$. We identify a foreground galaxy co-incident with the center of the Einstein ring seen in sub-mm emission ([Spilker et al., 2016](#), e.g.,) as a massive elliptical galaxy that dominates the emission out to $5''$ and the center of the Einstein ring seen in sub-mm dust emission is co-incident with the peak of the emission from the foreground galaxy to within $0''.05$. We fit a point source+Sérsic model for the galaxy and inspected the residuals for any emission from the background, high-redshift source. The residuals are spread in a ring geometry that is slightly smaller in radius as compared to the dust emission seen in long wavelength observations. However, they also show bright knots that are aligned with the point source response function (PRF) as recovered from a nearby star. Although offsets between UV-starlight and sub-mm dust emission have been observed in past observations of high-redshift galaxies ([Wong et al., 2017](#), e.g.,), given the suspicious alignment of the knots in the residuals with the PRF, we do not make any astrophysical interpretations from the residual emission seen at $1.4 \mu\text{m}$ at this point.

Archival: Spitzer Space Telescope

SPT0418-47 was observed using the Spitzer Infrared Array Camera (IRAC) in Cycle 13 (PI: Vieira, Program ID: 10094) in the 3.6 and $4.5 \mu\text{m}$ bands. We ob-

tained the pipeline calibrated images of SPT0418-47 from the Spitzer Heritage Archive. The source was observed for 100 seconds. The foreground galaxy is expected to dominate the emission in the near-infrared bands tracing mostly emission from old stars but the H- α line at the redshift of SPT0418-47 is shifted into the 3.6 μm band. We only make photometric measurements using standard aperture photometry techniques and use them to constrain the spectral energy distribution of the (foreground) lensing galaxy.

Archival: Wide-field Infrared Survey Explorer

We queried the publicly available All-sky data release ([Wright et al., 2010](#)) from the Wide-field Infrared Survey Explorer (WISE) to look for emission from SPT0418-47 between 3.4 and 22 μm . We queried the all-sky point source catalog for entries within 5'' of the Spitzer position. A source at the co-ordinates of SPT0418-47 was significantly detected in W1 (3.35 μm) and W2 (4.5 μm) bands, and at 4- σ in the W3 band (12 μm). We also report the 3- σ limit for the non-detection in W4 (22.1 μm) band, see Table [4.1](#).

Archival: Herschel Space Telescope

We reprocessed the observations taken with the Spectral and Photometric Imaging Receiver (SPIRE: ([Griffin et al., 2010](#))) under the program, OT1_jvieira_5, Observation ID 1342240101 on OD 1024. The source was observed for 445 seconds in the three SPIRE Photometer bands at 250, 350 and 500 μm . We use the source-ExtractorTimeline task in Herschel Interactive Processing Environment (HIPE) v15.0.1 ([Ott, 2010](#)) with the final mission calibration products v14.3 to estimate

the source flux density in each SPIRE waveband. The source is strongly detected in all three bands. Although our measurements are within the errors reported by Weiss et al. 2013, the values in each band are consistently higher by ~ 12 mJy. The statistical error for the fit is about 5 mJy in each band. We queried the SPIRE point source catalog (Schulz et al., 2017) at the location of SPT0418-47 but, for reasons that are not clear, there are no detections reported. The point source color correction required for SPIRE data points is 1.02 at $250 \mu\text{m}$, 0.99 at $350 \mu\text{m}$ and 0.96 at $500 \mu\text{m}$ for the estimated dust temperature and β (see Section 3.5). In Table 4.1, the errors reported with the SPIRE flux densities are the confusion noise in the maps as reported in the point source catalog. The confusion noise is expected to be much larger than the 5% calibration uncertainty or the statistical noise derived by the sourceExtractorTimeline task in HIPE ($\sim 2\%$). We also verified the reported flux densities at 100 and $160 \mu\text{m}$ from the Photodetector Array Camera and Spectrometer (PACS: (Poglitsch et al., 2010)) with the latest calibration products. The source is detected in the $160 \mu\text{m}$ waveband and we derive a $3\text{-}\sigma$ limit at $100 \mu\text{m}$, there are no observations available in the $70 \mu\text{m}$ waveband of PACS. The derived flux densities are consistent with those reported in the literature (Weiß et al., 2013).

Archival: ALMA Band-3 Spectral Scans

We queried the ALMA archive for observations of the SPT0418-47 and utilize the spectral scan observations in Band 3 that were used to secure the redshift of the SPT0418-47 as part of an observing campaign presented in Weiß et al. (2013). These scans include the CO(4-3), CI(1-0), and CO(5-4) lines that are redshifted to the 3mm band (reported by Bothwell et al. (2016)). We use the pipeline reduced

Far-IR Fine Structure lines in SPT0418-48 ($z_{src} = 4.225$)

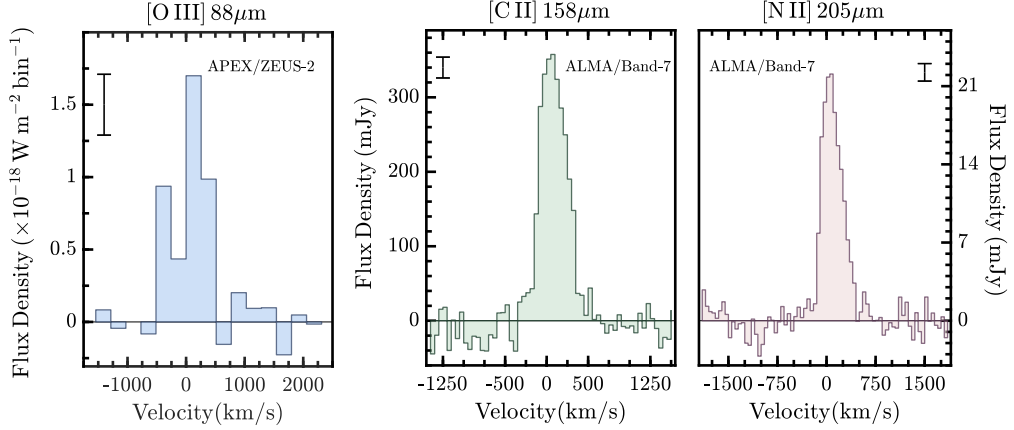


Figure 4.1 Source integrated spectrum of the (left) [O III] $88 \mu\text{m}$, (center) [C II] $158 \mu\text{m}$, and (right) [N II] $205 \mu\text{m}$ lines observed in SPT0418-47 at a redshift of $z = 4.225$. The velocity scale is with respect to the source redshift. Typical per bin $1\text{-}\sigma$ error is represented by the error bar in the upper corner of each panel.

data products delivered by the observatory through the data archive. To avoid potential contamination to the continuum from line emission and maximize the S/N, we measure the continuum at the highest frequency end of the spectral scan around 107 GHz which does not appear to contain any spectral features.

4.4 Results

4.4.1 ZEUS-2 detection of the [O III] $88 \mu\text{m}$ line emission

We detect the [O III] $88 \mu\text{m}$ line, shown here in Figure 4.1(left), at a flux level of $(4.0 \pm 0.8) \times 10^{-18} \text{ W m}^{-2}$, or equivalently $184 \pm 37 \text{ Jy-km s}^{-1}$, with an estimated calibration uncertainty of 20%. The reported line flux is derived by summing the power observed in four bins around the line center. The per pixel noise is estimated to be at $4.2 \times 10^{-19} \text{ W m}^{-2} \text{ bin}^{-1}$ and the rms error in the baseline

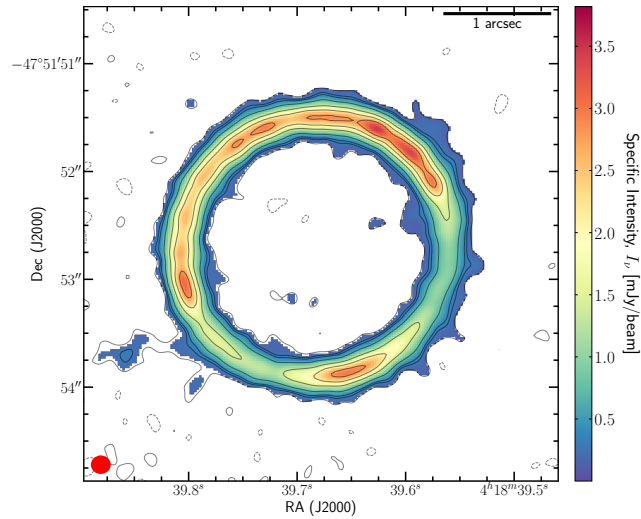


Figure 4.2 Dust continuum map at rest-frame $160\ \mu\text{m}$. Synthesized beam (FWHM: $0''.18 \times 0''.17$) is shown in the lower left. Overlaid contours at $[-3, 3, 6, 10, 15, 30, 45, 60] \times 46\ \mu\text{Jy/beam}$.

around the line is $1.3 \times 10^{-19}\ \text{W m}^{-2}$.

4.4.2 Dust Continuum Maps of SPT0418-47

We detect dust continuum emission at $838\ \mu\text{m}$ ($160\ \mu\text{m}$ rest-frame) from SPT0418-47, spread in a ring geometry over ~ 110 beams. The total continuum flux density detected at $838\ \mu\text{m}$ over the source is $114\ \text{mJy}$ with a statistical uncertainty of $0.8\ \text{mJy}$ derived by propagating the noise per beam near the middle of the Einstein ring. As mentioned before, the phase center of the observations is offset by $4''.9$ from the center of the observed ring, while the ring itself has a radius, $r_E = 1''.22$. This causes significant variation in the noise field over the extent of the source and we use a conservative estimate for the error to the measured continuum flux density as $\pm 3\ \text{mJy}$. The high resolution $160\ \mu\text{m}$ (rest-frame) continuum map is shown in Figure 4.2.

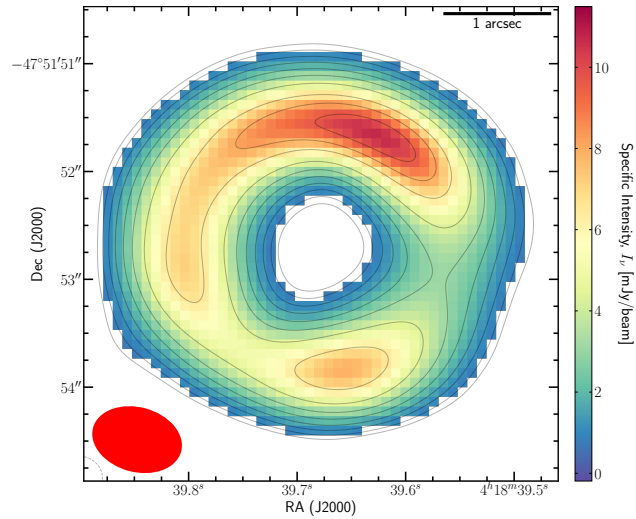


Figure 4.3 Dust continuum map at rest-frame $200\ \mu\text{m}$. Synthesized beam (FWHM: $0''.85 \times 0''.60$) is shown in the lower left. Overlaid contours at $[10, 14, 20, 28, 40, 56, 80, 120, 150, 180] \times 54\ \mu\text{Jy}/\text{beam}$

The dust continuum is also well detected at $1,048\ \mu\text{m}$ ($200\ \mu\text{m}$ rest-frame) from SPT0418-47. The overall morphology remains the same as that seen in the higher resolution map but due to the coarser spatial resolution, the individual sub-components are no longer distinguishable as seen in Figure 4.3. The continuum emission is spread over ~ 19 beams and the source-integrated continuum flux density at $1,048\ \mu\text{m}$ is $72 \pm 0.3\ \text{mJy}$, with the peak intensity detected at $190\text{-}\sigma$.

4.4.3 ALMA maps of the [C II] and [N II] line emission

To extract the line fluxes from the spectral cubes created for both the [C II] and [N II] lines, we follow two approaches - 1) Create a moment-0 map by collapsing all pixels detected at a significance of greater than $-3\text{-}\sigma$ in each velocity channel within $\pm 700\ \text{km s}^{-1}$ of the line center, and 2) Extract line profiles directly from

the line cube and fit multiple Gaussian components. By including a -3σ cutoff to create the moment-0 map, instead of a cutoff that includes pixels detected at $+1(+3)\sigma$, we avoid over(under)-estimating the line flux and make sure that the individual statistical fluctuations would cancel each other out rather than keep adding up. Next, we place apertures centered on the Einstein ring, ranging from $r=0''.4-2''.2$ and extract the integrated line flux in each aperture from the moment-0 map and the line profile within each aperture from the line cube. Decreasing the cutoff to include lower significance pixels increases the noise for the [C II] observations but does not affect the [N II] observations. Of course a larger aperture contains more flux, but the rate at which the signal (from the science target) increases slows down as the aperture grows. As the target is of finite size, at some point by increasing the aperture size, there is no appreciable increase in the signal contained within the aperture and the added noise worsens the signal to noise ratio of the measurement.

We utilize this curve of growth method to extract the spectrum shown in Figure 4.1 and the source integrated line fluxes are reported in Table 4.2. We find that the line profile varies significantly over the spatial extent of the source with at least three velocity components. A single Gaussian profile does not fit the line profile well for either of the spectrally well resolved lines, [C II] and [N II]. Therefore in Table 4.2, we only report the frequency at which the peak flux density of the integrated line profile is observed, the corresponding peak flux density in the velocity bin, the observed total line flux and the intrinsic line luminosity corrected for a lensing magnification factor of $\mu=32.3$.

We detect the [C II] $158\mu\text{m}$ line resolved over ~ 120 beams in the high-resolution ALMA observations. We report that the integrated line flux as

Table 4.2 Measured Line Properties of SPT0418-47

	[O III] 88 μm	[C II] 158 μm	[N II] 205 μm
ν_{peak} (GHz)	649.4	363.819	279.667
S_{peak} (mJy)	305 \pm 70	361.9 \pm 13	24.1 \pm 1.2
Observed Line Flux, I (Jy km s $^{-1}$)	184 \pm 37	130 \pm 5	7.7 \pm 0.3
Intrinsic Line luminosity ($\times 10^9 L_{\odot}$)	5.6	2.2	1.0

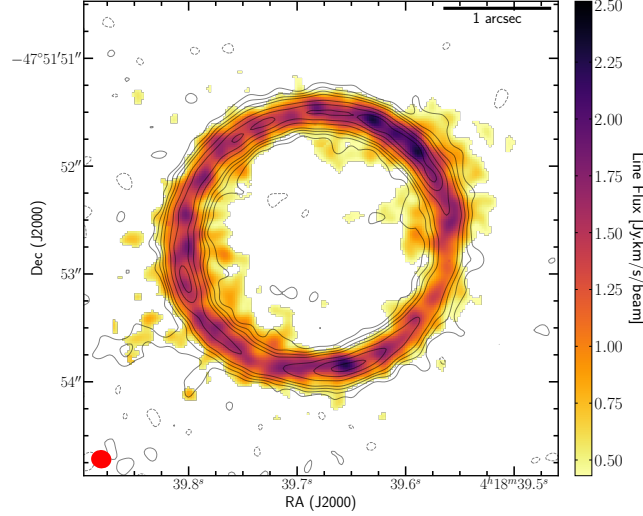


Figure 4.4 Map of the [C II] 158 μm line emission from SPT0418-47 . Synthesized beam (FWHM: $0'.19 \times 0'.17$) is shown in the lower left.

extracted over the moment-0 map for the [C II] 158 μm line is, $F_{\text{CII}}=130\pm 5$ Jy-km s $^{-1}$ or equivalently $(1.58 \pm 0.06) \times 10^{-18}$ W m $^{-2}$. This is consistent with the line flux reported for SPT0418-47 by [Gullberg et al. \(2015\)](#), $F_{\text{CII}}=127\pm 5$ Jy-km s $^{-1}$ based on observations with the APEX telescope.

We also clearly detect the [N II] 205 μm line in SPT0418-47 with emission spread over ~ 15 beams. The area from which the line emission originates appears to be smaller than that over which continuum is well detected ($\geq 10\text{-}\sigma$) at 200 μm , but this may be biased simply due to the surface brightness sensitivity of our observations combined with the depth of the continuum observations. We find that integrated over the entire source, the [N II] 205 μm line

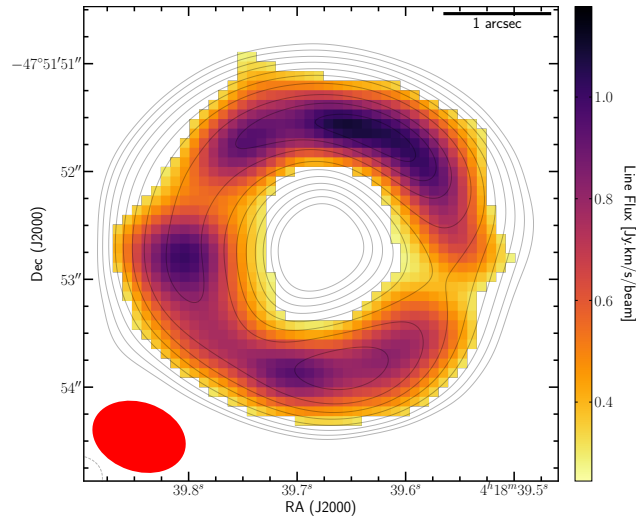


Figure 4.5 Map of the [N II] 205 μm line emission from SPT0418-47. Synthesized beam (FWHM: $0''.89 \times 0''.64$) is shown in the lower left.

flux is, $F_{\text{NII}} = 7.7 \pm 0.3 \text{ Jy} \cdot \text{km s}^{-1}$ or equivalently, $(7.2 \pm 0.3) \times 10^{-20} \text{ W m}^{-2}$. The [N II] 205 μm line is typically an order of magnitude fainter than the [C II] line and hence lensed sources would remain prime targets for resolved observations. Few previous observations have even marginally resolved [N II] emission in $z \sim 5$ galaxies (e.g. [Lu et al., 2017](#), [Pavesi et al., 2016](#)). The only significantly resolved observations of the [N II] 205 μm line that we could find in the literature are for a lensed SMG, MM 18423+5938 ([Decarli et al., 2012](#)). The observations presented in this paper are only the second well resolved map of the [N II] 205 μm line for a high-redshift source and the very first one made with observations using the ALMA telescope.

4.5 Discussion

Of the lines we have detected from SPT0418-47, the ionization potential to form the various ions are as follows: Atomic carbon is converted to the singly ionized

C^+ ion with an ionization energy of only 11.26 eV and the second ionization energy of carbon is 24.38 eV. To create N^+ requires 14.2 eV and another 29.6 eV to form N^{++} from N^+ , and the first ionization energy of atomic oxygen is almost exactly the same as neutral hydrogen at 13.62 eV and it takes 35.12 eV to form the O^{++} ion. For reference, the first ionization energy of helium, the second most abundant element, is 24.58 eV, so the harder ionization states of metal coexist with the ionized He bubble within HII regions. For the most massive stars, helium is ionized throughout the HII region and hence the species with lower ionization potentials like, N^+ and C^+ exist in a thin envelope near the edge of the Strömngren sphere. As the ionization potential of carbon is slightly less than that of hydrogen, carbon is also in the form of C^+ in an enveloping molecular cloud. The penetration depth of photons capable of ionizing carbon is usually determined by extinction of these photons by dust - typically at $A_V \sim 3$ (cf. [Tielens & Hollenbach, 1985](#)). Along about half this column, hydrogen molecules are photo-dissociated. These photo-dissociation regions are heated by the photo-ejection of hot electrons from dust and by the collisional de-population of photo-excited hydrogen molecules. Up to about 1% of the total FUV (6 to 13.6 eV) photon flux from the ionizing star can be converted into PDR gas heating by these processes. The PDR gas cooling is dominated by [C II] and [OI] fine-structure line emission, so that the [C II] line in particular has long been known to be among the brightest emission lines from star forming galaxies (e.g., [Crawford et al., 1985](#), [Stacey et al., 1991](#)).

We take advantage of this ionization structure and compare our observations with models of line emission from HII regions to interpret the conditions of the interstellar medium of SPT0418-47, specifically the hydrogen-ionizing photon flux and the density of the ionized gas. Although simplistic, as we are operating

under the assumption that the emission is dominated by HII regions and PDRs and ignoring other potential influences in the ISM like shocks and cosmic rays that have the potential to influence some tracers more than others, our interpretation of the observations provides a good first step towards understanding the conditions from which these lines arise in the ISM of SPT0418-47 and could provide important constraints if future observations require the need to include more complicated physics. There is little evidence for the predominance of any FIR fine-structure line emission on galactic scales coming from ‘exotic’ sources, except in one extreme case, PDRs compressed by shocks in Stephan’s Quintet ([Appleton et al., 2013](#)).

4.5.1 Estimating the Ionized Gas contribution to the [CII] line

Following the method outlined by ([Oberst et al., 2011, 2006](#)), one can estimate the fractional contribution of the [C II] line that comes from ionized regions using the ratio of the [C II] and the [N II] lines. With an ionizing potential of 14.2 eV, N⁺ only exists within regions where hydrogen is also ionized but the C⁺ ion (IP=11.2 eV) could be present in both ionized and neutral gas. Therefore, the total observed [C II] line emission would be the sum of emission from ionized gas as well as neutral gas:

$$L([\text{CII}])_{tot} = L([\text{CII}]_{ion}) + L([\text{CII}]_{neutral})$$

The transitions that the [C II] 158 μm and the [N II] 205 μm lines arise from are 91 and 70 K above ground so unlike optical lines their level excitation is only very weakly dependent on the gas temperatures in HII regions ($T_e \sim 8,000$ K). Since their critical densities for thermalization by electron impacts in HII re-

gions are nearly identical at $n_{\text{crit}} \sim 45 \text{ cm}^{-3}$ and the species are found in similar ionization zones, this means that the $[\text{C II}]/[\text{N II}]$ 205 line intensity ratio in HII regions is only dependent on the $[\text{C}/\text{N}]$ gas phase abundance ratio.

Using the abundances used in the ‘K’ models from [Rubin \(1985\)](#) and an electron temperature of 8000 K, $[\text{C}/\text{H}] = 3.7 \times 10^{-4}$ and $[\text{N}/\text{H}] = 1.15 \times 10^{-4}$, the $L_{[\text{CII}]} / L_{[\text{NII}]}$ ratio is predicted to be 5.26 within $\pm 14\%$ for densities between 5 and 500 cm^{-3} . While keeping everything else the same, if we change the absolute abundances to be similar to that of diffuse gas in the Milky Way, $[\text{C}/\text{H}] = 3.7 \times 10^{-4}$ and $[\text{N}/\text{H}] = 1.15 \times 10^{-4}$, the $L_{[\text{CII}]} / L_{[\text{NII}]}$ ratio is predicted to be 2.9 within $\pm 15\%$. Any observed excess above the predicted line ratio from ionized gas, suggests a contribution to the $[\text{C II}]$ luminosity from other phases of the ISM, likely PDRs. This method has since been used to measure the diffuse ionized gas contribution to the $[\text{C II}]$ line, locally in the Milky Way and all the way up to galaxies within the first billion years since the Big Bang (e.g., [Combes et al., 2012](#), [Díaz-Santos et al., 2017](#), [Goldsmith et al., 2015](#), [Herrera-Camus et al., 2018](#), [Oberst et al., 2011](#), [Pavesi et al., 2016](#)).

In the case of SPT0418-47, the measured average $L_{[\text{CII}]} / L_{[\text{NII}]}$ ratio is 22. Using the above estimates, and the measured ratio, it implies that about 24% (or 14% of slightly different $[\text{C}/\text{N}]$) of the $[\text{C II}]$ line arises in ionized gas, assuming abundances from ‘K’ models (diffuse gas). Therefore, the ionized gas contribution to the total observed $[\text{C II}]$ luminosity from SPT0418-47 would be $L([\text{CII}]_{\text{ion}}) = 1.7 \times 10^{10} L_{\odot}$.

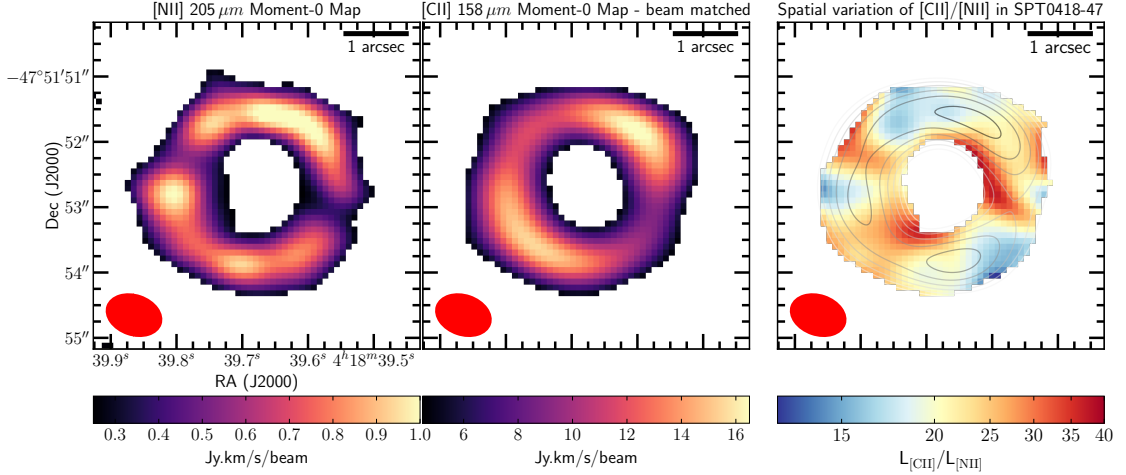


Figure 4.6 (left) [N II] 205 μm moment-0 map.(center) The higher resolution [C II] moment-0 map is smoothed to the exact same beam size and orientation as the [N II] map (right) Pixel-by-pixel line luminosity ratio across SPT0418-47 as calculated using the [C II] and [N II] moment-0 maps. Contours are overlaid for the continuum at 160 μm

4.5.2 A Young Starburst and Ionized Gas

In this section we discuss the constraints on the massive star population that could support the ionization in the gas to power the observed line luminosities, and the corresponding minimum mass of the ionized gas through the emitting species, C^+ , N^+ , and O^{++} .

The presence of the O^{++} ion requires photons at least as energetic as the ionization potential of 35.12 eV. The luminosity of such high energy photons is dominated by stars more massive than $20 M_{\odot}$. For a given starburst event, the ionizing photon flux that can result in creation of the O^{++} ion will fade away quite rapidly, as the most massive stars evolve off of the main sequence within 3-10 Myr. The overall spectrum of the ionizing photon flux changes drastically once these massive stars fade away - B-stars that last for $\mathcal{O}(100 \text{ Myr})$ can maintain the ionization state of hydrogen due to their sheer numbers but the supply

of harder photons drops precipitously. The observations of the [O III] line provide a unique constraint on the upper mass end of the current day stellar main sequence, and in turn on the time since the last major star formation event. Such information is difficult to gauge using emission lines from species with lower ionization potentials.

We combine the observed line luminosities and the line ratios to match model stellar populations under the constraint that the total luminosity of the modeled (young) stellar populations be less than or equal to the total infrared luminosity of the system. As we will discuss in more detail in Section 4.5.3, SPT0418-47 is a heavily obscured source that likely emits almost all or a large fraction of its total luminosity at long wavelengths. The dust in the source will absorb far-UV radiation from the young stars and radiate it back at far-IR wavelengths, as seen by the peak of the dust SED (see Figure 4.7). All three of the line species under discussion here arise, at least in part from within ionized gas, therefore it is appropriate to use all of them for constraining the stellar population. Assuming the starburst is headed by a certain spectral type of star, we can convert the estimate of the ionizing photon flux to a number and type of such stars. We can then extrapolate the total stellar mass assembled in the ongoing star-formation episode assuming an initial mass function along with the measured star-formation rate.

The various line luminosities are tabulated in Table 4.2. From the discussion in Section 4.5.1, we estimated the ionized gas contribution to the total [C II] line luminosity as $L_{\text{CII,ion}} \sim 1.4 \times 10^{10} L_{\odot}$. As we do not yet have resolved observations of the [O III] line, we will make the simplifying assumption that gravitational lensing affects all the lines in an identical manner, so that the line ra-

tios are devoid of systematic uncertainty due to differential lensing. This is a common assumption for infrared fine-structure lines in unresolved star-forming sources and has generally been borne out well by further resolved observations (Serjeant, 2012). We calculate the following integrated line luminosity ratios, $L_{\text{OIII}}/L_{\text{CII,ion}} = 13$, $L_{\text{OIII}}/L_{\text{NII}} = 55$ and $L_{\text{CII,tot}}/L_{\text{NII}} = 22$.

We employ models of HII region around massive stars (Rubin, 1985) and compare them with the observed emission from SPT0418-47. The spectral type classification for massive stars is adopted from the calibration of Martins et al. (2005) and is used to match the effective stellar temperatures, T_{eff} , from the models. We adopt the hydrogen burning timescale for massive stars of solar metallicity from Ekström et al. (2012) as the main sequence lifetime of the respective stars. In particular, we use the ‘K’ model grid of the HII region models, to carry out the fitting exercise here. These models are based on stellar atmosphere models from Kurucz (1979, 1993) with an [O/H] abundance of 6.76×10^{-4} . The parameter space for the models used here covers a broad range of the effective stellar temperature ($T_{\text{eff}}=31\text{-}45$ kK), the Lyman continuum (LyC) photon rate ($Q_0=10^{49-50} \text{ s}^{-1}$), and the electron number density in the HII regions ($n_e = 10^{2-4} \text{ cm}^{-3}$).

We find two sets of consistent solutions by simultaneously fitting the three lines fluxes and their ratios across the grid of parameters. The first favors a low density solution with $n_e=10^2 \text{ cm}^{-3}$ and T_{eff} from 37,000 to 39,000 K, and the other prefers a high density solution that fits equally well for $n_e=10^3$ and 10^4 cm^{-3} but suggests a slightly cooler $T_{\text{eff}} = 36,000$ K. However, the total number of stars required to maintain the supply of ionizing photons and sustain the ionization state increases rapidly for the high density solution. So much so that the bolo-

metric luminosity of the required stars at high densities far exceeds the total infrared luminosity of the whole galaxy. Therefore, we reject the high density solutions and suggest that the emission observed from SPT0418-47 is coming from moderate density ionized gas with $n_e \sim 100 \text{ cm}^{-3}$ and hosts a recent or on-going starburst event dominated by O7 stars.

We repeat the above exercise with only the [O III] and [N II] lines and their ratio as input and compare the [C II] emission predicted from the best fit models to what we derived in the previous section. We find that the best fit parameters are identical and the fraction of [C II] line arising from the models for HII regions, i.e., ionized gas is $\sim 20\%$. This matches the estimate between 14 and 24%, we made in the previous section and further adds confidence to our result.

The line fluxes originating in ionized gas can be used to estimate the minimum mass of the ionized nebula that could power the observed emission. The N^+ and O^{++} ions are iso-electronic and the [N II] 205 μm and [O III] 88 μm lines both are transitions into the ground state from the first excited level that are only 70 and 160 K above ground respectively. C^+ only has one excited level in its fine-structure splitting, about 91 K above ground. As the ionized gas in HII regions is heated up to 8,000-10,000 K, we can make the approximation of being in the high-temperature limit, such that $e^{-\Delta E_i/kT} \sim 1$ within a few%. The one major difference between the various lines are their critical density, the [N II] line (& [C II] in ionized regions) has $n_{\text{crit}} \sim 45 \text{ cm}^{-3}$ whereas the the [O III] line has a critical density, $n_{\text{crit}} \sim 510 \text{ cm}^{-3}$. As the estimated density from the best-fit models above is $\sim 100 \text{ cm}^{-3}$, we expect the [N II] 205 μm and [C II] 158 μm lines to be thermalized but making that assumption for the [O III] line will only provide an upper limit. Following the method of [Ferkinhoff et al. \(2010\)](#), but to make a

Table 4.3 Calculation of Ionized Gas Mass with various tracers and comparison to other Baryonic components of SPT0418-47

Quantity	[O III]	[C II] _{ion}	[N II]
Apparent Line Luminosity ($\times 10^{10} L_{\odot}$)	18	1.4	0.33
ν_{rest} (GHz)	3393.0624	1900.5369	1461.1314
Elemental Abundance ($\sum_i \chi^{i+}/H^+ \simeq [\chi/H]$) ($\times 10^{-4}$)	6.76	3.70	1.14
Fraction in Relevant ionization state (χ^{i+}/χ)	0.29	0.54	0.62
Fraction in Emitting level, J_{em} (for $n_e=100 \text{ cm}^{-3}$)	0.212	0.576	0.473
A_{line} ($\times 10^{-6} \text{ s}^{-1}$)	26	2.29	2.06
Estimated Ionized Gas Mass ($\times 10^8 M_{\odot}$) (corrected for lensing, $\mu=32.3$)	4.6 ± 0.9	3.6 ± 0.2	7 ± 0.3
Estimated Mass of the Young Stellar Population ($\times 10^9 M_{\odot}$, corrected for lensing)	2.7		from Section 4.5.2
Molecular Gas Mass ($\times 10^9 M_{\odot}$) ($\alpha_{CO}=0.8$, corrected for lensing)	5		(Aravena et al., 2016)
Estimated Total Stellar Mass ($\times 10^9 M_{\odot}$, corrected for lensing)	70_{-60}^{+20}		from Section 4.5.3

more robust measurement, we add an estimate of the fractional abundance in the detected ionization state from the models, and solve for the exact level populations in the emitting levels using the estimated density of the emitting gas. This way, we avoid making the high density, high temperature limit approximation, that only allows us to estimate the minimum mass ionized nebula required to support the luminosity of the observed line from an ionized species. Since the line emissivity, $j = A_{ul} h \nu_{ul} n_u$. The estimate of the mass can be obtained using:

$$M_{\min}^{\text{H}^+} = 4\pi d_L^2 \frac{F_{\text{ion}}}{\frac{n_u}{n_e} A_{ul} h \nu_{ul} \chi_{\text{ion}}} \frac{m_{\text{H}}}{\chi_{\text{ion}}} \quad (4.1)$$

but, we use the constraints obtained from the best-fit density and radiation field instead of approximating the terms in the denominator of Equation 4.5.2. We use the observed line flux, F_{ion} in W m^{-2} , where F_{ion} is the observed line flux of the [O III], [N II] and [C II]_{ion}, d_L is the luminosity distance (m), A_{ul} is the spontaneous emission coefficient (s^{-1}) for the line transition, h is Planck's constant (J-s), ν_{ul} is the rest frequency for the line transition, m_{H} is the mass of a hydrogen atom, and χ_{ion} is the relative abundance of ion being traced by the line transition ($X^{i+}(J_{em})/H^+$).

First we quantify the fraction of the total elemental abundance that is in the ionization state from which we detect the line. The HII region models provide us that information for each model, and we look up the relevant fractions for the

best fit models. We find that only 49-58% of the carbon is in C^+ state, 59-64% of the nitrogen is in N^+ state and only about 26-32% of oxygen is in the O^{++} state. Further using a density of 100 cm^{-3} and the principles of detailed balance, we can estimate the fractional population in the emitting levels. We tabulate each of these quantities in Table 4.3 for all three of the ions discussed here. We find that about a fifth of the oxygen ions are in the first excited state and about half of the carbon and nitrogen ions are in the emitting levels – this is in contrast with the estimate we would have made with the assumption of the high density limit, where a one third of the oxygen and nitrogen ions and two thirds of the carbon ions would be expected to be in the emitting levels.

Using Equation 4.5.2, and the parameters for the various lines tabulated in Table 4.3, we calculate the (lensing-corrected) minimum mass of ionized gas in SPT0418-47 to be $\sim 3\text{-}7 \times 10^8 M_{\odot}$. Our estimate of the ionized gas mass accounts for about 10% of the total molecular gas mass estimated from observations of the CO(2-1) line in SPT0418-47 by Aravena et al. (2016). We’d like to point out that the estimates using the [C II] and the [O III] lines are similar but those using the [N II] line are off by almost a factor of two. This might be correlated to the spatial variation of the [C II] / [N II] ratio or be a direct consequence of an elevated [N/O] abundance.

4.5.3 Optical-to-cm Spectral Energy Distribution

Our compilation of photometric measurements ranges from observed-frame, optical to cm-waveband, with the foreground lensing galaxy dominating the optical-to-near-infrared part of the spectral energy distribution (SED) and the

high-redshift, lensed galaxy dominating the far-IR to the cm wavebands. We employ model SEDs based on emission seen from a variety of nearby galaxies and a modified black body fit to explore the best fit to the observed emission from both sources. We use the models from [Polletta et al. \(2007\)](#), which provide templates for typical local-ULIRGs, AGNs, as well as star-forming and elliptical galaxies. We use the extensive coverage from the far-IR to cm wave-band for SPT0418-47, which adequately samples the peak of the dust emission, that is important to constrain the dust temperature (T_{dust}), as well as the Rayleigh-Jeans tail, that is essential to estimate the dust emissivity index (β). Combined with an independent estimate of the dust emitting source size from lens modeling, we can break the degeneracy between β , T_{dust} and λ_0 , the wavelength at which the dust optical depth reaches unity $\tau_\nu=1$.

To model the foreground galaxy ($z=0.265$ ([Hezaveh et al., 2013](#))) we only fit a scale parameter to measure the goodness of fit for various SED templates. The foreground galaxy appears to be a massive elliptical from appearance at optical wavelengths. With a well sampled optical SED, we can estimate the age of the dominant stellar population in the galaxy and hence estimate the epoch during which it assembled most of its stellar mass. With a good understanding of the foreground galaxy's emission, we can calculate the fractional contribution of the lensing and the lensed galaxy to the observed flux towards SPT0418-47 in bands where we have no hope of spatially resolving the two components.

Out of the 20 templates available from [Polletta et al. \(2007\)](#), the optical emission fits remarkably well to the Elliptical galaxy model with a stellar population age of 5 Gyr (see [Figure 4.7](#)). We rule out the model with a 2 Gyr old stellar population and the fit to the 10 Gyr old model is good in the optical wavelengths but

shows significant departure at near-infrared wavelengths. The age of the Universe at $z=0.265$ is ~ 10.6 Gyrs and a dominant stellar population that is 5 Gyr old would imply a formation epoch at $z\sim 1.1$, a 10 Gyr old population is technically feasible but pushes the formation epoch to $z\sim 8$. The non-detection of dust in the ALMA maps also allows us to estimate an upper limit on the ‘ISM’ mass of the elliptical galaxy using the method of [Scoville et al. \(2016\)](#). The $3\text{-}\sigma$ upper limit from the continuum at 286 GHz, $S_\nu < 0.16$ mJy, places a strong limit on the rest-frame $825\ \mu\text{m}$ emission from the central ~ 3 kpc of the elliptical galaxy. We estimate a total ISM mass of $< 7.8 \times 10^8 M_\odot$ and, assuming a Milky Way like gas-to-dust mass ratio of 100, we get a limit on the dust mass, $M_d < 7.8 \times 10^6 M_\odot$. Using the light profile of the elliptical galaxy from the HST/WFC3 $1.4\ \mu\text{m}$ image, we estimate a stellar mass surface density approaching $10^{10} M_* \text{ kpc}^{-2}$ in the central kpc. This matched well with the mass estimate within the Einstein ring based on the gravitational lensing model.

Despite the presence of the old stellar population in the the foreground massive elliptical galaxy, the observed near-infrared emission could have significant amounts of contamination from (rest-frame) optical light from the background high-redshift galaxy. In Section 4.3.3, we attempted to measure such contribution by subtracting a point+Sérsic model from the HST $1.4\ \mu\text{m}$ image but to no avail. Now, with a good handle on the emission expected from the elliptical galaxy, we can subtract the contribution of the foreground galaxy at $\lambda_{\text{obs}} > 3\ \mu\text{m}$ and estimate the fraction of emission that could be due to the high-redshift source. At $3.5\ \mu\text{m}$ (rest-frame 670 nm), we estimate the potential contribution of the high-redshift galaxy to be $\leq 12\%$ ($\leq 30\ \mu\text{Jy}$) but increasing to about $\sim 30\%$ ($\sim 55\ \mu\text{Jy}$) at $4.5\ \mu\text{m}$ (rest-frame 860 nm). The emission seen by WISE at $12\ \mu\text{m}$ (rest-frame $2.3\ \mu\text{m}$), is expected to be dominated by the high- z

source with as much as $\sim 80\%$ (~ 0.17 mJy) of the observed emission attributed to SPT0418-47.

A rough estimate of the stellar mass can be obtained by using the relationship between the K-band rest-frame magnitude to stellar mass suggested by [Magdis et al. \(2010\)](#):

$$\log\left(\frac{M_*}{M_\odot}\right) = 2.01(\pm 0.65) - 0.35(\pm 0.03) \times M_{2\mu\text{m}} \quad (4.2)$$

where, $M_{2\mu\text{m}}$ is the absolute magnitude of the galaxy at $2\mu\text{m}$. At the distance of SPT0418-47, its absolute magnitude at (rest-frame) $2\mu\text{m}$, based on the flux we estimated above, would be $M_{2\mu\text{m}} = -29.58$, and the estimated apparent stellar mass would be $M_* \sim 2 \times 10^{12} M_\odot$. If we assume that the sub-mm lensing magnification factor ($\mu = 32.3$) applies similarly to the stellar component, then the intrinsic stellar mass for SPT0418-47 would be $\sim 7 \times 10^{10} M_\odot$. As is clear from the coefficients of the equation above, this estimate has an uncertainty of up to an order of magnitude. Our estimate is consistent with those obtained for a subsample of SPT-galaxies by [Ma et al. \(2015\)](#), $M_* \sim 3\text{-}15 \times 10^{10} M_\odot$, based on fluxes extracted for the high-z sources after subtracting foreground lens emission in near-infrared images.

With bright detection at various sub-mm/mm wavelengths, it is clear that the dust emission from the high-redshift galaxy dominates the long wave end of the SED. Leveraging our high resolution maps at $838\mu\text{m}$ and 1 mm presented in Section 4.4.2, and which show no hint of a detection within the Einstein ring, we can rule out any significant contributions to the unresolved continuum fluxes obtained with Herschel, APEX, SPT and the ATCA (see Figure 4.2 and Figure 4.7).

The best fit parameters for the modified black body are listed in Table 4.4. L_{IR}

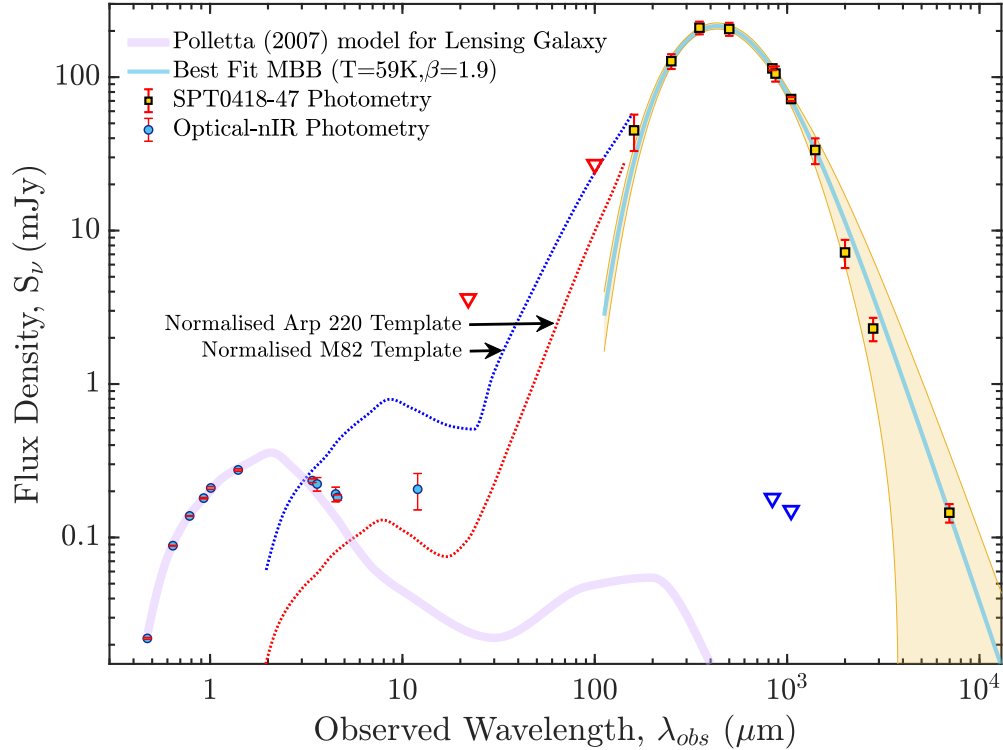


Figure 4.7 Spectral Energy Distribution fit for SPT0418-47: The solid blue line (shaded yellow patch) represents the best fit modified blackbody fit (68% confidence bound) to the far-IR-mm dust photometry from SPT0418-47 (filled yellow squares with red error bars). The red triangles mark upper limits based on non-detections in the WISE 22 μm and PACS 100 μm bands. The blue triangles are upper limits on sub-mm/mm emission from the foreground lensing galaxy based on no detections at the center of the Einstein ring in the ALMA maps. The optical photometry (filled blue circles with red error bars) is dominated by emission from the foreground galaxy and is well fit by a 5 Gyr old elliptical galaxy model (purple line). We plot a scaled version of the mid-infrared SED from two IR bright local galaxies, Arp220 (heavily obscured) and M82 (less obscured), to highlight the effect of dust obscuration on the observed near-to-mid-infrared emission from the background high redshift galaxy. The WISE 12 μm detection is expected to be dominated by the background galaxy hints that SPT0418-47 is indeed heavily obscured out to rest-frame 2 μm .

is calculated by integrating under the best-fit SED between $\lambda_{rest} = 8 - 1000 \mu\text{m}$ and L_{FIR} by integrating over $\lambda_{rest} = 42.5 - 122 \mu\text{m}$.

Table 4.4. Derived Physical Properties of SPT0418-47

Quantity	Value	Unit	Notes/Ref
IR Luminosity (L_{IR}) ^a	$1.2 \pm 0.4 \times 10^{14}$	L_{\odot}	
Far-IR Luminosity (L_{FIR}) ^a	$6.7 \pm 0.4 \times 10^{13}$	L_{\odot}	
Dust Temperature ($T_{\text{dust,MBB}}$)	59.3 ± 1.3	K	
Dust Emissivity Index (β)	1.9 ± 0.1		
λ_0	200 ± 16	μm	

^aIR luminosity is calculated between 8-1000 μm

^bFIR luminosity is calculated between 42.5-122.5 μm

4.5.4 Resolved Maps of the Dust Continuum Emission

We present high resolution maps of the dust continuum emission at (rest-frame) 200 μm , with a beam FWHM of $\sim 0''.7$, and, at (rest-frame) 160 μm , with a beam FWHM of $\sim 0''.17$. The 200 μm map is comparable in spatial resolution to the data presented by Spilker et al. 2016 (at rest-frame 166 μm). The beam sizes achieved in the interferometric observations correspond to ≤ 1 kpc at $z=4.2$ and the gravitational lensing magnification affords us access to even smaller physical scales. The 160 μm image resolves the dust continuum in great detail and reveals small scale structure through the lensed image that appears on the sky as a ring. Multiple knots are detected with peak intensities detected at 45–60- σ around the ring forming five sets of images, indicating that the source has at least four bright components all within ~ 1 kpc of each other.

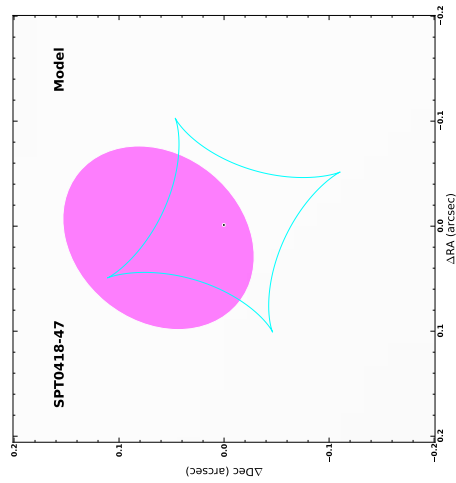
First, we create a gravitational lensing model for the dust emission seen at 200 μm with the help of the lensing code, *uvmcmcfits*. Details about the code are presented in [Bussmann et al. \(2015\)](#). We briefly review the exercise to recover

Table 4.5 Best-fit Lens Model parameters for 200 μm continuum observations of SPT0418-47 compared with rest-frame 166 μm model from literature

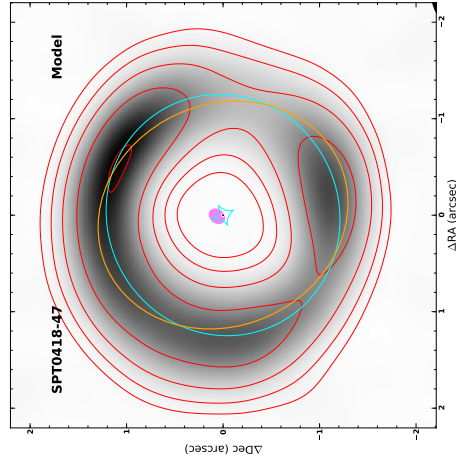
Parameter	Value		Spilker et al. (2016) model
Lens RA Initial Guess	$-47^{\circ}51^m52.742^s$	(1)	
Lens Declination Initial Guess	$04^h18^m39.679^s$	(2)	
Einstein Radius	1.2325 ± 0.0004	arcsec	1.247 ± 0.003
Δ RA	-0.0014 ± 0.001		
Δ Dec	0.0003 ± 0.001		
Lens Axial Ratio	0.8673 ± 0.0013		0.888 (Ellipticity=0.112)
Lens Position Angle	24.49 ± 0.12	$^{\circ}$	0.01 ± 23.7
Source Intrinsic Flux	1.71 ± 0.02	mJy	2.58 ± 0.23
Source Effective Radius	0.0752 ± 0.0008	arcsec	0.092 ± 0.008
Source Physical Radius (FWHM)	1202 ± 14	pc	(Sersic, $n = 0.74 \pm 0.18$)
Source Δ RA	0.0123 ± 0.0003	(relative to 1)	
Source Δ Dec	0.0622 ± 0.001	(relative to 2)	
Source Axial Ratio	0.809 ± 0.003	$^{\circ}$	0.859 ± 0.03
Source Position Angle	140.7 ± 0.9	$^{\circ}$	133.9 ± 10.2
μ_{tot}	32.3 ± 0.4		32.7 ± 2.7

the best-fit parameters for the lensing geometry and the source for the observed emission. The code uses a ray-tracing algorithm to create a model with parameters that allow us to vary the position, orientation and Einstein radius for the lens and the source size and orientation with respect to the lens. We use an elliptical Gaussian as the source model. The code uses as input the complete uv-plane sampling with which the observations were made and creates a simulated observation of the model using them. The resulting complex visibilities are then compared to the observed visibilities to measure a goodness-of-fit for a given set of parameters. In this sense, the `uvmcmcfits` code allows us to fully make use of the redundant spatial information encoded in the visibilities. To avoid biased estimates from local minimum in the parameter space, we sample each parameter from a uniform distribution and calculate the maximum-likelihood estimate for the best-fit parameters.

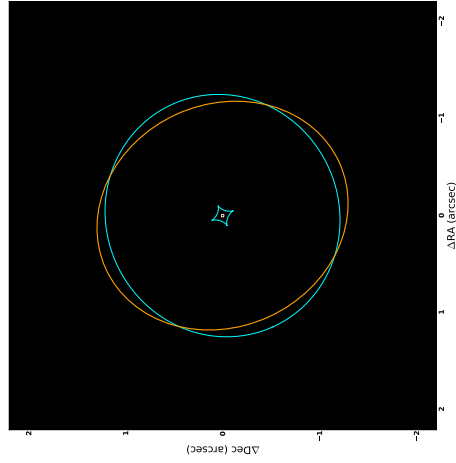
We list the best fit model parameters in Table 4.5 and show the model and the residuals in Figure 4.8. The lens models required to faithfully recover the



(a) Best-fit source-plane configuration for the observed emission from SPT0418-47. The tangential lensing caustic is drawn in cyan and the half-power shape of the source is shown as a magenta ellipse



(b) Best-fit model imaged after convolution with the observed visibilities. Image plane emission is shown in grayscale, overlaid with red contour (starting at $+3\text{-}\sigma$ and increasing in increments of $\sqrt{2}$)



(c) Residuals between the best-fit model and the observed emission for SPT0418-47. Solid (dashed) contours represent $+(-)$ $3\text{-}\sigma$ confidence

Figure 4.8 Best-fit gravitational lensing model for the observed emission from SPT0418-47 using *uvmmcmfit*

structure seen in the high resolution data are beyond the scope of the software used here and would be presented in a future publication.

Gravitational lensing conserves surface brightness, therefore the observed intensity (Jy/sr) in the dust continuum map can be directly converted to the thermal temperature of the emitting dust (K), if the source is completely resolved. For high signal to noise detection, like the data at hand, we can estimate the emitting source size, even if the emission is only marginally resolved. From the gravitational lensing model above, we can see that the source overlaps a fold caustic as well as crosses a cusp. We can only marginally distinguish multiple images in the $200\ \mu\text{m}$ (rest-frame) map but the $160\ \mu\text{m}$ (rest-frame) shows multiple bright images spread in an arc. These are the multiple images of the unresolved source seen (and modeled) in the $200\ \mu\text{m}$ data.

As a first estimate of the size of the source, we measure the thickness of the Einstein ring at various locations on the $160\ \mu\text{m}$ map and de-convolve it from the beam to estimate the intrinsic emitting size. We measure that the thickness of the Einstein ring varies between $0''.088$ and $0''.115$, where the beam of the continuum observations is $0''.18 \times 0''.17$. For a completely resolved source, the brightness temperature measured within a beam would provide the equivalent temperature of a thermal source. However, our measurements show that SPT0418-47 is only marginally resolved in the observations presented here. This corresponds to a beam dilution factor of $\frac{\Omega_{beam}}{\Omega_{src}}$ of 3.95-2.3. Assuming an average beam dilution factor of 3, the peak observed brightness temperature (see Figure 4.9) is $\sim 33\text{K}$. This agrees with our estimate of the dust opacity in Section 4.5.3 as the correction due to opacity would bring the brightness temperature in agreement with the dust temperature estimated from the SED.

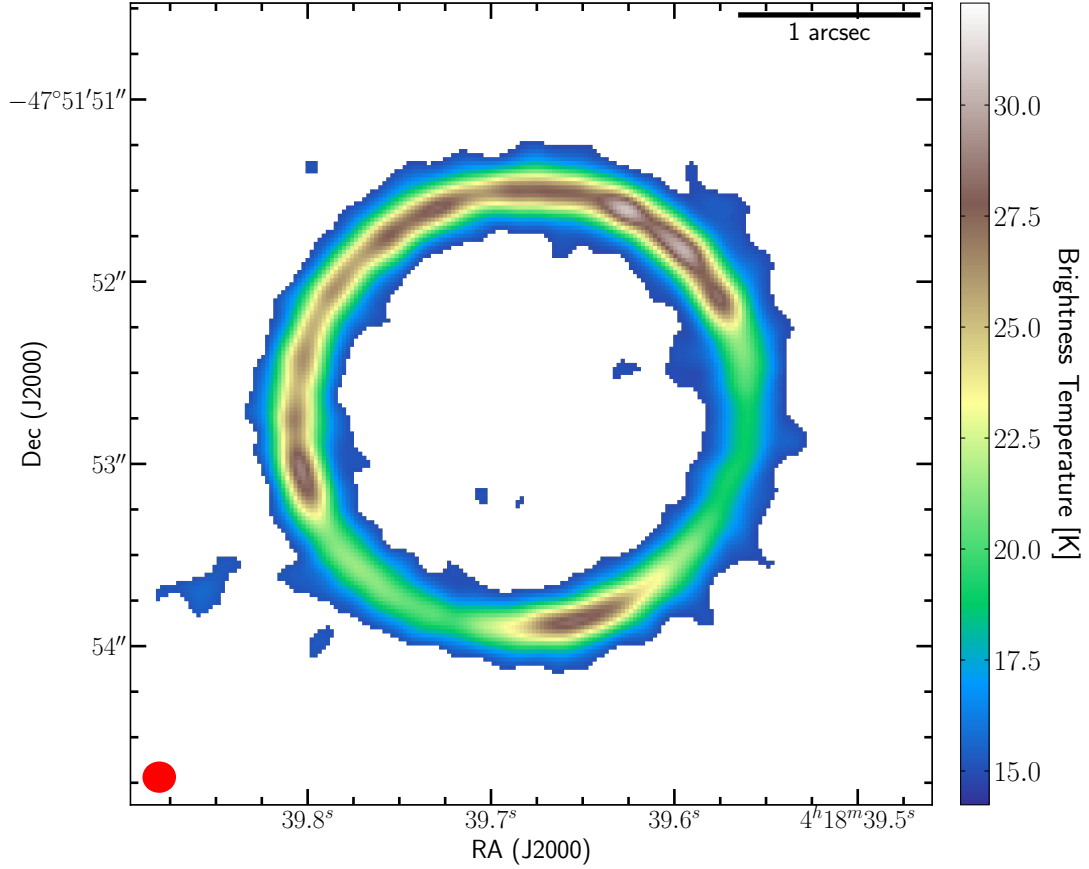


Figure 4.9 Brightness temperature estimated from the high resolution continuum map at $838 \mu\text{m}$. An average beam dilution factor of 3 has been applied before calculating the brightness temperature. The lower limit on the temperature is close to the temperature of the CMB at the source redshift.

In order to compare the two continuum maps and avoid artifacts due to different synthesized beams with the interferometer, we use the CASA task `imsmooth` to smooth the high resolution $160 \mu\text{m}$ continuum to the exact same beam as the $200 \mu\text{m}$ continuum. The resulting continuum maps are shown in Figure 4.10, with the native $200 \mu\text{m}$ map on the left panel and the smoothed $160 \mu\text{m}$ map in the central panel. We then proceed to calculate a pixel-by-pixel spectral index using these maps, following a functional form, $S_\nu \propto \nu^\alpha$ such that $\alpha = \log(\frac{S_{\nu_1}}{S_{\nu_2}}) / \log(\frac{\nu_1}{\nu_2})$, for the dust emission in SPT0418-47. We apply a hard cut-

off on the intensity in each of the beam-matched continuum maps, such that only pixels detected at a significance of $10\text{-}\sigma$ or more were used to create the spectral index map. The resulting spectral index map is shown in the right-most sub-panel of Figure 4.10. We over plot the contours from the smoothed $160\ \mu\text{m}$ map to guide the eye for variation in brightness of the continuum emission. It shows clear variation in the spectral index across the source. If the emission was squarely on the Rayleigh-Jeans tail then a modified blackbody form, $S_\nu \propto \nu^{2+\beta}$, would result in a spectral index $\alpha = 2 + \beta$. We find that the median spectral index is $\alpha \sim 2.1\text{-}2.2$ that is found along the regions where the lensing arcs are the brightest.

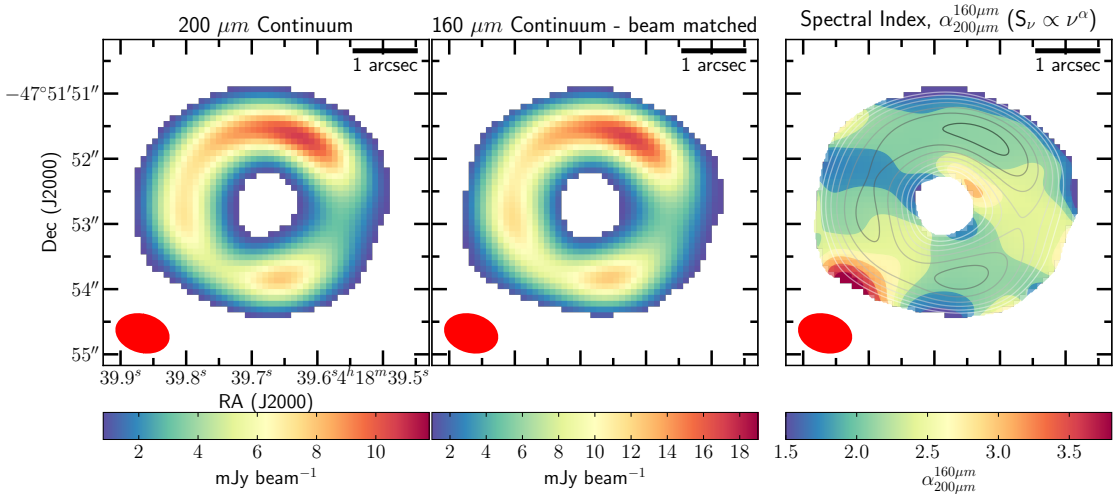


Figure 4.10 Spectral index map ($S_\nu \propto \nu^\alpha$) as calculated for dust continuum emission seen at $160\ \mu\text{m}$ and $200\ \mu\text{m}$ from SPT0418-47. The higher resolution $160\ \mu\text{m}$ map is smoothed to the exact same beam size and orientation as the $200\ \mu\text{m}$ map before calculating α . A steeper (shallower) spectral index – larger (smaller) α – requires the peak of the dust emission to be shifted to shorter (longer) wavelengths which could potentially be accounted for by hotter (cooler) dust temperature or dust emission that becomes optically thick at shorter (longer) wavelengths.

Regions away from the bright lensing arcs, both radially and azimuthally, show variation in the spectral index. The eastern (left) side shows a lower spec-

tral index ($\alpha \sim 1.7$) whereas the south-eastern (lower left) and western (right) end of the ring shows a higher spectral index ($\alpha \sim 2.7-3$). The very high spectral index (~ 4) on the south-eastern end may be in part due to the increasing noise due to the primary beam response falling off for the $160 \mu\text{m}$ map.

It is interesting to note that the radially outer most regions just above (below) the peak emission around the northern (southern) image, show low spectral index ($\alpha \sim 1.3$). As the magnification due to gravitational lensing is achromatic, each pixel corresponding to the same spatial location undergoes the same magnification, and should not bias our results in the image plane. To first order, the low spectral index could be due to a gradient in dust temperature across the source. If the outer parts of the continuum source have colder dust, the emission would peak at longer wavelengths, thereby making the spectral index shallower between 160 and $200 \mu\text{m}$. The spectral index is however, always greater than one. Dust emission from a 18 K blackbody would have its peak at $160 \mu\text{m}$, therefore, given the spectral index, α , is always greater than 1, we could infer that the dust emission is warmer than 18 K everywhere in the source. This should be reasonable, given the temperature of the CMB at $z=4.225$ is about 14.5 K .

In Section 3.5.1, we estimate, based on a modified black body fit to the integrated SED of SPT0418-47, that the peak of the dust emission occurs close to (rest-frame) $85 \mu\text{m}$ but is optically thick ($\tau \sim 1$) out to $200 \mu\text{m}$. Given we are working with observations at two wavelengths and limited spatial resolution, we can not, just yet, break the degeneracy between variation in dust temperature and dust opacity across the source. We would require high(er) spatial resolution observations of the dust continuum at $220 \mu\text{m}$ and closer to the peak

of the SED (i.e., at shorter wavelengths).

4.6 Conclusions

We have presented new observations of far-infrared fine-structure lines of [C II], [N II] and [O III] from gravitationally-lensed, dusty, star-forming galaxy, SPT0418-47 at $z=4.225$. We resolve the source in great detail with bright continuum emission detected around an Einstein ring at both (rest-frame) 160 and 200 μm . We also present new observations of spatially resolved [C II] 158 μm and [N II] 205 μm spectral lines that reveal spatial variation across the source in line-to-continuum and the [C II] / [N II] ratio.

We estimate that $\sim 20\%$ of the total [C II] emission from SPT0418-47 arises from ionized gas. We use the joint constraints from the [O III], [N II] and [C II] lines and the total infrared luminosity to suggest that most of the ionized gas emission arises in moderately dense, $n_r \sim 100 \text{ cm}^{-3}$ gas. We find that the present day stellar mass function due to the on-going star-formation activity is headed by O7V stars. The Lyman continuum flux required to support the observed line intensities is $N_{LyC} \sim 2.7 \times 10^{55} \text{ s}^{-1}$, which could be supported by an on-going star-formation episode with $\text{SFR} = 450 M_{\odot} \text{ yr}^{-1}$ for at least 6 Myrs. The bolometric luminosity of the on-going star-burst contributes to $\sim 15\%$ of the observed IR luminosity and have assembled $\sim 2.7 \times 10^9 M_{\odot}$ of young stellar population.

Using integrated SED models, we find that the dust emission from SPT0418-47 is optically thick out to 200 μm and that the dust SED peaks at $\sim 60 \text{ K}$. Both with SED and lensing models, we estimate that the size of the dust continuum

emitting source is ~ 1.3 kpc in diameter. The high resolution $160 \mu\text{m}$ continuum reveals that there are at least 4 bright clumps all within 1 kpc of each other that are likely buried deep under dust and are each less than 200 pc wide. The brightness temperature map of the continuum suggests that these clumps are unresolved at $0''.15$ resolution of our data (which in source plane corresponds to 200 pc) and contain dust that is hotter than 60 K.

Based on decomposition of the observed emission, into the foreground lensing galaxy and the background high-redshift galaxy, we observe that at $3.4 \mu\text{m}$, where the rest-frame $\text{H}\alpha$ line from SPT0418-47 is redshifted to, the foreground galaxy dominates the total emission by roughly a factor of 4. However, by $8 \mu\text{m}$ the high- z galaxy is expected to be brighter than the lensing galaxy by a factor of 2-4. It is important to recall that, being gravitationally-lensed, the total emission from SPT0418-47 will be spread over 5 times larger area than the lensing galaxy and surface brightness considerations should be taken into account when planning future observations of SPT0418-47 with the James Webb Space Telescope (JWST). Given the favorable contrast, between the lensing galaxy and the high- z source, we recommend that the best wavelength range for spatially resolved observations of SPT0418-47 would be at wavelengths $\lambda > 8 \mu\text{m}$, using the MIRI instrument or spectroscopic observations using the NIRSpec instrument between 2 and $5 \mu\text{m}$ that could allow access to potentially bright optical lines like $[\text{O III}] 5007$ and $\text{H}\alpha$.

We have demonstrated the utility of far-IR, fine structure line to study the interstellar medium and stellar populations of high-redshift galaxies in detail. Future spatially resolved observations will help us address the potential issue of differential lensing between different lines and also study the relative changes

in line emission at scales as small as 100 pc in a galaxy that is undergoing star-formation activity across the source building up its stellar mass.

CHAPTER 5
FUTURE WORK

5.1 Discovery of a compact sub-arcsecond Einstein Ring with ALMA

5.1.1 Introduction

As the number and depth of statistical surveys of sub-millimeter galaxies has increased, so too has the observed diversity of the samples. A deeper understanding of the nature of sub-millimeter galaxies requires in depth examination of properties of individual galaxies, and especially investigation of those systems which lie at the edges of population distributions, representing unique systems. As discussed in Chapter 3, G12v2.43 is one such galaxy with extreme luminosity and observed line emission properties. The relative sensitivities of ZEUS-2 on APEX and Atacama Large Millimeter/sub-millimeter Array (ALMA) provide an important synergy in that, once detected with ZEUS-2 the same lines can be mapped over ~ 20 beams with ALMA in a similar amount of observing time.

We present preliminary results based on the lens modeling of the observed dust continuum and [C II] line emission from G12v2.43. With the lensing galaxy's redshift still elusive, we estimate its mass based on continuum methods as a function of its redshift and validate that against the estimate of the lensing mass from the lens models.

5.1.2 Observations

Here we present new observations taken with ALMA that resolve G12v2.43 with an angular resolution of $0''.1$. As we had speculated in the discussion for Chapter 3, imaging the source at this higher resolution clearly reveals that it is strongly lensed with bright emission from dust at (rest-frame) $160\ \mu\text{m}$ spread around an extremely compact Einstein ring with a radius of just $0''.45$. There is an additional surprising discovery – at the center of the Einstein ring – a bright detection of a $\sim 9\ \text{mJy}$ source. The brightness of this source at the center rules out it being the central de-magnified image of the lensed galaxy. The lensing geometry that results in an Einstein ring requires that most of the mass responsible for that gravitational potential that bends the light has to be within the ring itself. So, it is reasonable to attribute this emission to be coming from a foreground galaxy that is indeed the lensing galaxy for G12v2.43. Not only do our observations confirm the G12v2.43 is gravitationally lensed, but they also provide strong evidence that it is a case of strong galaxy-galaxy lensing with the discovery of the lensing galaxy, for the first time at sub-mm wavelengths.

We imaged the high resolution ALMA data with CASA version 5.0 after processing the data with the provided pipeline. We collapsed the spectral channels that are free from any spectral line emission and imaged the observed continuum emission. We imaged the channels that contain the [C II] line separately to create a spectral cube for the observed line emission.

We collapsed the [C II] data cube to create a total intensity map of the line emission. We use this map and the corresponding visibilities to perform lens modeling that is described in detail in the next section. The emission observed in the image strongly constrains the lensing configuration and suggests that

the gravitational potential that is causing the observed lensing, is concentrated within the Einstein ring.

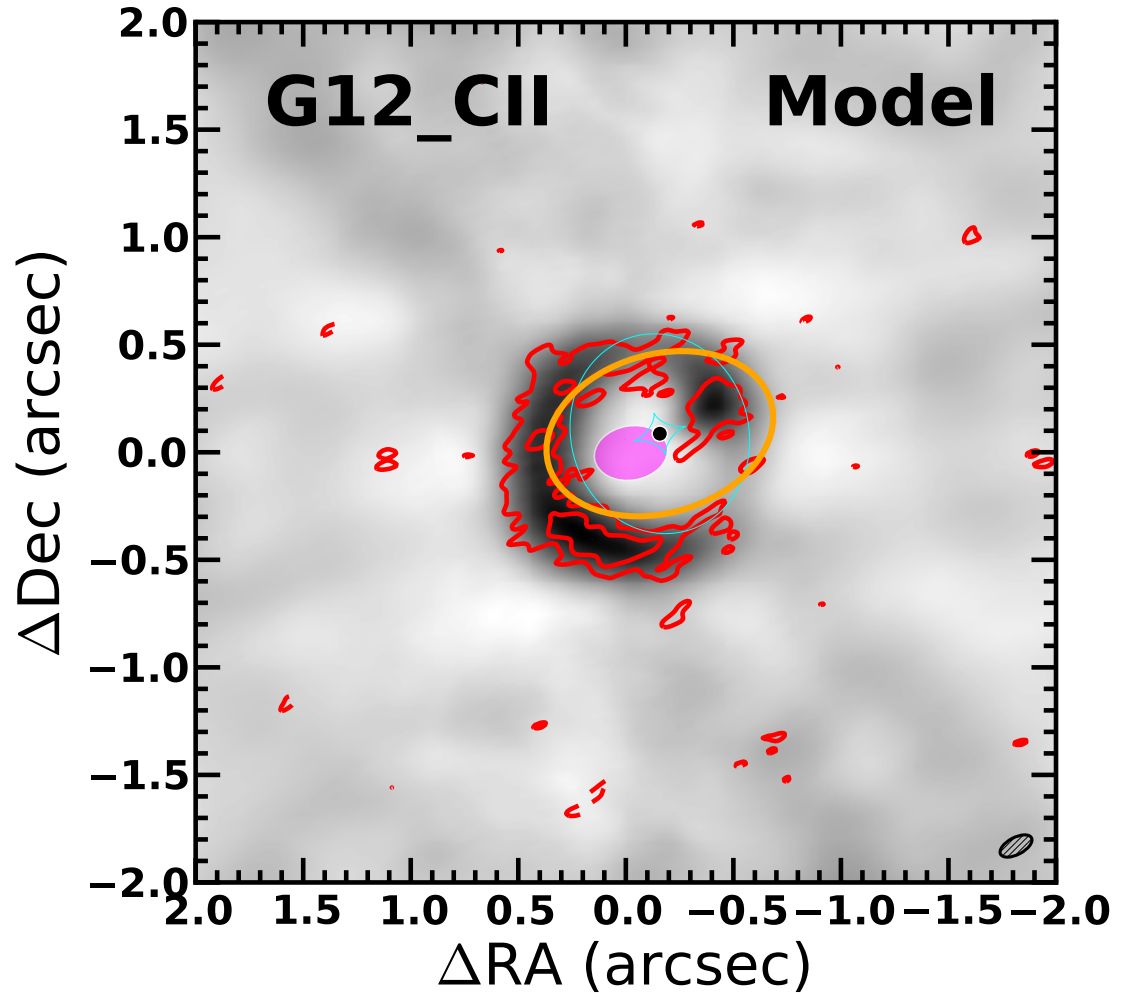


Figure 5.1 Best fit gravitational lensing model for the [C II] emission seen from G12v2.43.

5.1.3 Gravitational Lens Modeling

We use the gravitational lens modeling tool `uvmcmfit` to model the sub-mm emission from G12v2.43 detected with the ALMA observations. `uvmcmfit` utilizes a fast ray-tracing code to create an image of the lens plane emission and

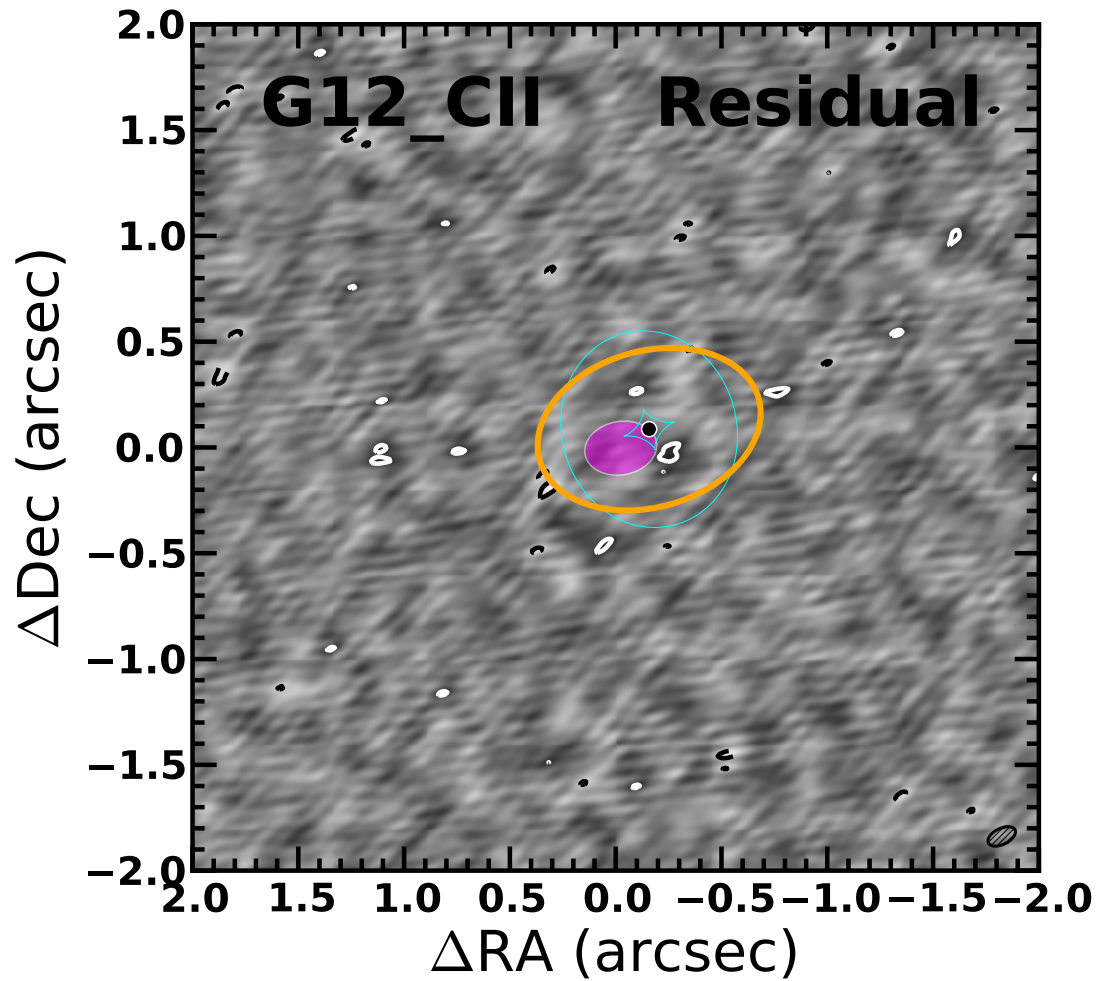


Figure 5.2 Residuals between the observed emission and the best fit gravitational lensing model shown above.

convolves it with the same uv-coverage as our observations to create an interferometric image that can be compared to the observations. The lensing galaxy is assumed to be a singular isothermal ellipsoid (SIE) and the source is assumed to be a 2-D Gaussian. Multiple realizations for the image plane emission are created by varying model parameters including the relative location of the lensing and lensed galaxies, shape of the lensing potential, Einstein radius of the lens-

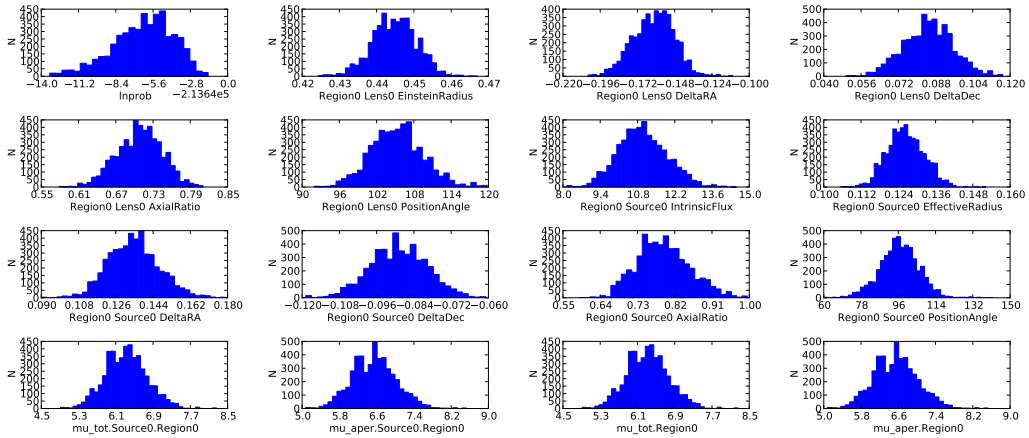


Figure 5.3 Distribution of the parameters used to estimate the best fit model for observed emission. We assume a single lensing galaxy, with parameters for the the location of the galaxy on the sky and the shape of its lensing potential. These parameters include the Einstein radius, relative positions of the foreground and background galaxies. The source is assumed to be a single 2-D Gaussian with parameters effective radius (FWHM), axial ratio and position angle.

ing galaxy, and the shape and orientation of the lensed galaxy with respect to the lensing caustic of the lensing galaxy. The best-fit parameters were estimated using chi-square minimization between the model and observed images.

We show the best fit lensing model in Figure in Figure 5.1 and the corresponding residuals in Figure 5.2. Based on visual inspection of the continuum image, the centroid of the lensing potential (galaxy) was allowed to move $\pm 1''.5$ from the center of the observed ring. This limited the range of models that need to be run and given the Einstein radius is estimated to be $\sim 0''.5$, this choice of limiting the parameter space is justified. A complete probability distribution for all the parameters explored during the lens modeling exercise is shown in Figure 5.3. All the model parameters are very well constrained with uncertainties consistent to what would be expected given the beam size of the interferometric observations.

The observed emission can strongly constrain the Einstein radius of the lensing galaxy but there is significant degeneracy between the mass of the lensing galaxy (interior to the Einstein radius) and the redshift of the galaxy itself. An estimate of the lensing mass is shown in Figure 5.4 and remains below $10^{11} M_{\odot}$ for $z < 1$. Typical sub-mm discovered galaxies have copious amounts of dust and are typically fairly massive. Given the foreground galaxy is causing strong galaxy-galaxy lensing and the estimate of the mass rises steeply beyond redshift 2, it is probable that the lensing galaxy is indeed a high-redshift galaxy that is heavily obscured.

If indeed the lensing galaxy is at $z \sim 2$, the observed flux density of 9 mJy at $651 \mu\text{m}$ could correspond to emission on the Rayleigh-Jeans tail from dust within the lensing galaxy. If the galaxy is at a lower redshift, the dust emission is certainly on the long wavelength end. We use template spectral energy distributions from Polletta et al. (2007) for star-forming galaxies in the nearby Universe and compare them with the observed continuum emission. The flux density reported in the templates are scaled to a fixed infrared luminosity with the galaxy placed at a redshift of $z = 0.01$. As we redshift the template galaxies, in order to fit the observed continuum emission we scale the infrared luminosity of the templates and store the scale factor for the best-fit model at each redshift. Using these best-fit models at each redshift, we then use the scaling between infrared luminosity and star-formation rate from Kennicutt & Evans (2012) to infer the star-formation rate in the lensing galaxy as a function of its redshift, see Figure 5.4.

Following the method of Scoville et al. (2016), we can employ the observed long wavelength dust emission to estimate the mass of the interstellar medium

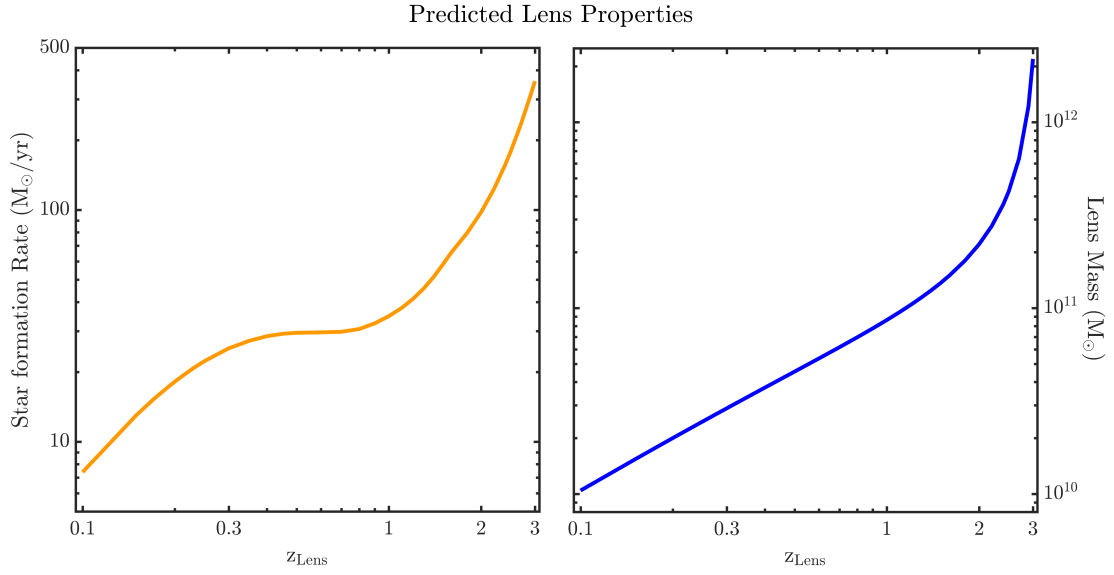


Figure 5.4 (left) An estimate of the star formation rate based on the continuum source detected in the center of Einstein ring using template matching for SED templates for star-forming galaxies.(right) An estimate of the mass within the Einstein ring required to reproduce the observed lensing configuration based on the best-fit model parameters. It is clear from the plot that the lensing galaxy mass is a strong function of the lens redshift, particularly at the high- z end.

in the galaxy. This estimate of the ‘ISM mass’ provides us a useful comparison with the lensing mass estimated using the gravitational lensing models. As these estimates are used making two completely independent methods, each with their corresponding uncertainties, the comparison allows us to explore possible solutions for the redshift-mass degeneracy. We use three different dust temperatures for estimating the ISM mass using the R-J continuum. This should allow us to capture a wide range of possible conditions in the ISM of the host galaxy. We present the individual estimates of the lensing mass and the ISM mass and the corresponding ratios as a function of redshift in Figure 5.5.

We find that two ranges of redshift stand out where the lensing mass and the ISM mass estimates are identical. As the Einstein radius is quite small, $\theta_E=0''.44$, the spatial scale at any redshift for the lensing galaxy are ~ 850 pc (at $z\sim 0.1$) and

up to 3.8 kpc (at $z \sim 1.5$) and we do not expect significant contribution from dark matter to the lensing mass. Also, if the observed sub-mm emission at the center is from the lensing galaxy then the measured size of the source is only about $0''.25$ (FWHM).

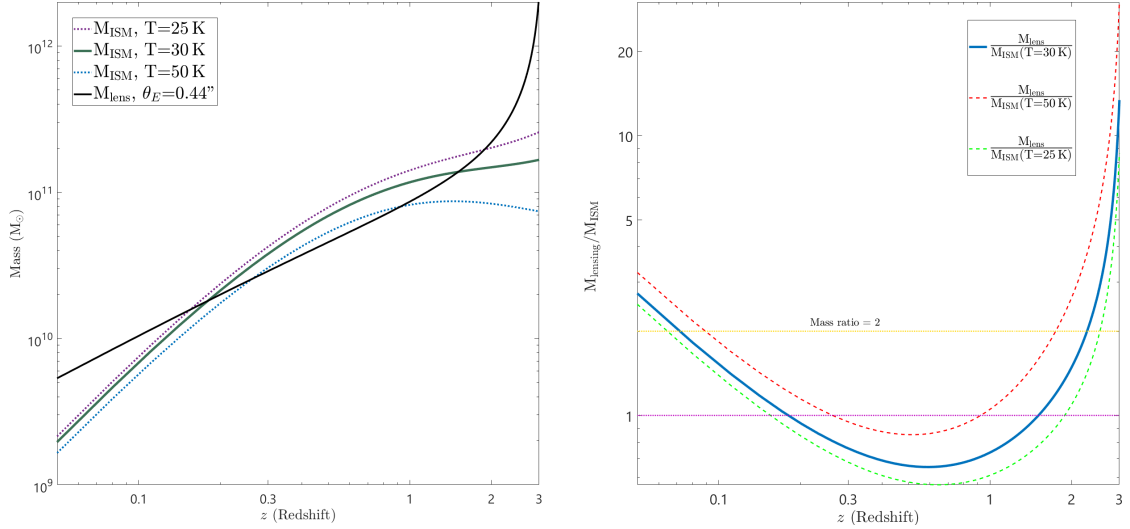


Figure 5.5 (left) An estimate of the mass based on the best-fit lensing configuration and the ISM mass estimate derived based on the method outlined in [Scoville et al. \(2016\)](#). (right) The ratio of the estimated lensing mass and ISM mass. As a reasonable estimate, we suggest that the mass ratio should be close to unity for most galaxies, allowing us to identify two likely solutions, one around $z \sim 0.2$ and another between $z \sim 1-2.5$.

In case of the low- z solution, $z \sim 0.2$, the mass of the lensing galaxy is rather small, $2-3 \times 10^{10} M_{\odot}$. The source size ($0''.25$), corresponds to only about 850 pc. Based on non-detections in optical and near-infrared bands, we can strongly rule out a massive stellar mass component to this galaxy. This leaves the possibility for an obscured, low mass, but yet dust-rich galaxy. As seen in most local ULIRGs, dust emission is typically associated with recent or on-going star-formation activity. A low stellar mass and the bright dust emission might indicate that this galaxy at $z \sim 0.2$ has recently started building up its stellar mass. It would be instructive to study the environment in which this galaxy resides,

and whether that is correlated with its apparent lack of star formation and stellar mass. We can already rule out the presence of any massive galaxies within $8''$ with the help of Hubble near-infrared observations presented in [Vishwas et al. \(2018\)](#). In order to account for the the observations and the scenario in which this galaxy is at low-redshift, an explanation that puts this galaxy in a local void might work. Being in a local void, the galaxy would be lagging behind in accumulating gas and the absence of any environmental triggers could lead to it having a smaller stellar mass. If not for the chance alignment with a high-redshift source, such galaxies would be easily missed in other surveys.

The alternate explanation would land the lensing galaxy squarely in the typical ‘SMG’ category, a dust rich, obscured luminous/ultra-luminous galaxy at the Cosmic Noon. The observed dust emission would be extended over ~ 1.5 - 2 kpc, consistent with average size of the dust emission observed in galaxies at $z \sim 1$ - 4 . However, this explanation raises a question about the physical properties like dust temperature, star-formation rate of the lensed galaxy. These properties for G12v2.43 were presented in [Vishwas et al. \(2018\)](#) based on the source integrated SED that uses observations that can not resolve the dust emission of the lensed galaxy from the lensing galaxy. The dust emission from most galaxies peaks between 50 and $100 \mu\text{m}$ (rest-frame), that would indicate that the (observed-frame) $651 \mu\text{m}$ emission at the center of the Einstein ring is not tracing the peak of the dust emission from the lensing galaxy, a SMG at $z \sim 1$ - 2 . The observed flux density in the SPIRE bands that is assumed to be coming from the high-redshift lensed galaxy would be severely contaminated by the foreground lens. To address this complication, we measured the resolved continuum of G12v2.43. We find that the observed flux density at $651 \mu\text{m}$ measures brighter than what is predicted by the SED. It would suggest that the dust temperature of

G12v2.43 is slightly lower than what was estimated earlier. Previous detections of bright molecular gas lines and the [O III] detection with ZEUS-2, combined with the detection of the [C II] line in the ALMA data indicate that the estimated gas mass and the overall far-infrared luminosity of the source should not be significantly different from earlier measurements.

These data will benefit from manual calibration and additionally, as the source is very bright, from self-calibration. The self-calibrated data products should have a significantly better image quality than the current pipeline reduced datasets. The preliminary estimates are unlikely to change but the confidence in the inferred results would increase if we can improve the line and continuum image quality. The higher quality spectral line data would allow us to study the kinematics of the gas as traced by the [C II] line at a spatial scale of 80150 pc. Using the resolved dust continuum measurements and modeling of the data using priors for dust temperature and redshift for a foreground source, we will be able to quantify the estimates of dust mass and dust temperature in the lensing galaxy and re-evaluate the dust temperature and star-formation rate in the high-redshift source, G12v2.43. With these measurements we will be able to estimate the dust-to-gas mass ratio and even study if it varies across the lensed morphology of the source.

This work is a follow-up study to results presented in Chapter 3 of this thesis and is in progress for future publication in *The Astrophysical Journal*.

BIBLIOGRAPHY

- Abbott, T. M. C., Abdalla, F. B., Allam, S., et al. 2018, *ApJS*, 239, 18
- Appleton, P. N., Guillard, P., Boulanger, F., et al. 2013, *The Astrophysical Journal*, 777, 66
- Aravena, M., Spilker, J. S., Bethermin, M., et al. 2016, *Monthly Notices of the Royal Astronomical Society*, 457, 4406
- Benford, D. J., Gaidis, M. C., & Kooi, J. W. 1999, in *Tenth International Symposium on Space Terahertz Technology*, ed. T. W. Crowe & R. M. Weikle
- Bothwell, M. S., Smail, I., Chapman, S. C., et al. 2013, *MNRAS*, 429, 3047
- Bothwell, M. S., Aguirre, J. E., Aravena, M., et al. 2016, *Monthly Notices of the Royal Astronomical Society*, 466, 2825
- Bradford, C. M., Stacey, G. J., Swain, M. R., et al. 2002, *Appl. Opt.*, 41, 2561
- Brauher, J. R., Dale, D. A., & Helou, G. 2008, *ApJS*, 178, 280
- Brisbin, D., Ferkinhoff, C., Nikola, T., et al. 2015, *ApJ*, 799, 13
- Bruzual, G., & Charlot, S. 2003, *MNRAS*, 344, 1000
- Bussmann, R. S., Pérez-Fournon, I., Amber, S., et al. 2013, *ApJ*, 779, 25
- Bussmann, R. S., Riechers, D., Fialkov, A., et al. 2015, *The Astrophysical Journal*, 812, 43
- Calanog, J. A., Fu, H., Cooray, A., et al. 2014, *ApJ*, 797, 138
- Calzetti, D., Armus, L., Bohlin, R. C., et al. 2000, *ApJ*, 533, 682

- Carlstrom, J. E., Ade, P. A. R., Aird, K. A., et al. 2011, *Publications of the Astronomical Society of the Pacific*, 123, 568
- Carniani, S., Maiolino, R., Pallottini, A., et al. 2017, *A&A*, 605, A42
- Carral, P., Hollenbach, D. J., Lord, S. D., et al. 1994, *The Astrophysical Journal*, 423, 223
- Casey, C. M. 2012, *MNRAS*, 425, 3094
- Charlot, S., & Fall, S. M. 2000, *ApJ*, 539, 718
- Ciesla, L., Boselli, A., Elbaz, D., et al. 2016, *A&A*, 585, A43
- Clements, D. L., Rigby, E., Maddox, S., et al. 2010, *A&A*, 518, L8
- Colbert, J. W., Malkan, M. A., Clegg, P. E., et al. 1999, *The Astrophysical Journal*, 511, 721
- Combes, F., Rex, M., Rawle, T. D., et al. 2012, *Astronomy & Astrophysics*, 538, L4
- Cormier, D., Madden, S. C., Lebouteiller, V., et al. 2015, *A&A*, 578, A53
- Crawford, M. K., Genzel, R., Townes, C. H., & Watson, D. M. 1985, *ApJ*, 291, 755
- da Cunha, E., Charlot, S., & Elbaz, D. 2008, *MNRAS*, 388, 1595
- da Cunha, E., Walter, F., Smail, I. R., et al. 2015, *ApJ*, 806, 110
- Dale, D. A., Helou, G., Magdis, G. E., et al. 2014, *ApJ*, 784, 83
- Decarli, R., Walter, F., Neri, R., et al. 2012, *ApJ*, 752, 2
- Díaz-Santos, T., Armus, L., Charmandaris, V., et al. 2017, *ApJ*, 846, 32

- Douthit, G., Stacey, G., Nikola, T., et al. 2018, in Society of Photo-Optical Instrumentation Engineers (SPIE) Conference Series, Vol. 10708, Millimeter, Submillimeter, and Far-Infrared Detectors and Instrumentation for Astronomy IX, 107081P
- Downes, D., Solomon, P. M., & Radford, S. J. E. 1993, *The Astrophysical Journal*, 414, L13
- Draine, B. T. 2003, *ARA&A*, 41, 241
- . 2010, *Physics of the Interstellar and Intergalactic Medium* (University Press Group Ltd)
- Draine, B. T., & Li, A. 2007, *ApJ*, 657, 810
- Ekström, S., Georgy, C., Eggenberger, P., et al. 2012, *A&A*, 537, A146
- Farrah, D., Lebouteiller, V., Spoon, H. W. W., et al. 2013, *ApJ*, 776, 38
- Ferkinhoff, C. 2014, PhD thesis, Cornell University
- Ferkinhoff, C., Brisbin, D., Nikola, T., et al. 2015, *The Astrophysical Journal*, 806, 260
- Ferkinhoff, C., Hailey-Dunsheath, S., Nikola, T., et al. 2010, *ApJ*, 714, L147
- Ferkinhoff, C., Brisbin, D., Nikola, T., et al. 2011, *ApJ*, 740, L29
- Ferkinhoff, C., Nikola, T., Parshley, S. C., et al. 2012, in *Proc. SPIE*, Vol. 8452, Millimeter, Submillimeter, and Far-Infrared Detectors and Instrumentation for Astronomy VI, 845207
- Ferkinhoff, C., Brisbin, D., Parshley, S., et al. 2014, *ApJ*, 780, 142

- Fixsen, D. J., Cheng, E. S., Gales, J. M., et al. 1996, *The Astrophysical Journal*, 473, 576
- Fritz, J., Franceschini, A., & Hatziminaoglou, E. 2006, *MNRAS*, 366, 767
- Genzel, R., Tacconi, L. J., Lutz, D., et al. 2015, *ApJ*, 800, 20
- Goldsmith, P. F., Yıldız, U. A., Langer, W. D., & Pineda, J. L. 2015, *The Astrophysical Journal*, 814, 133
- Graciá-Carpio, J., Sturm, E., Hailey-Dunsheath, S., et al. 2011, *ApJ*, 728, L7
- Griffin, M. J., Abergel, A., Abreu, A., et al. 2010, *A&A*, 518, L3
- Gullberg, B., Breuck, C. D., Vieira, J. D., et al. 2015, *Monthly Notices of the Royal Astronomical Society*, 449, 2883
- Güsten, R., Booth, R. S., Cesarsky, C., et al. 2006, in *Proc. SPIE, Vol. 6267, Society of Photo-Optical Instrumentation Engineers (SPIE) Conference Series*, 626714
- Hailey-Dunsheath, S. 2009, PhD thesis, Cornell University
- Hailey-Dunsheath, S., Nikola, T., Stacey, G. J., et al. 2010, *ApJ*, 714, L162
- . 2008, *ApJ*, 689, L109
- Harris, A. I., Baker, A. J., Frayer, D. T., et al. 2012, *ApJ*, 752, 152
- Hashimoto, T., Laporte, N., Mawatari, K., et al. 2018a, *Nature*, 557, 392
- Hashimoto, T., Inoue, A. K., Mawatari, K., et al. 2018b, arXiv e-prints, arXiv:1806.00486
- Herrera-Camus, R., Sturm, E., Graciá-Carpio, J., et al. 2018, *The Astrophysical Journal*, 861, 94

- Hezaveh, Y. D., Marrone, D. P., Fassnacht, C. D., et al. 2013, *The Astrophysical Journal*, 767, 132
- Hodge, J. A., Swinbank, A. M., Simpson, J. M., et al. 2016, *ApJ*, 833, 103
- Inoue, A. K., Tamura, Y., Matsuo, H., et al. 2016, *Science*, 352, 1559
- Kennicutt, R. C., & Evans, N. J. 2012, *Annual Review of Astronomy and Astrophysics*, 50, 531
- Komatsu, E., Smith, K. M., Dunkley, J., et al. 2011, *The Astrophysical Journal Supplement Series*, 192, 18
- Kurucz, R. L. 1979, *ApJS*, 40, 1
- . 1993, *VizieR Online Data Catalog*, 6039
- Lamarche, C., Verma, A., Vishwas, A., et al. 2018, *The Astrophysical Journal*, 867, 140
- Laporte, N., Ellis, R. S., Boone, F., et al. 2017, *ApJ*, 837, L21
- Latvakoski, H. M. 1997, PhD thesis, CORNELL UNIVERSITY
- Leitherer, C., Schaerer, D., Goldader, J. D., et al. 1999, *ApJS*, 123, 3
- Leroy, A. K., Bolatto, A., Gordon, K., et al. 2011, *ApJ*, 737, 12
- Lord, S. D., Hollenbach, D. J., Haas, M. R., et al. 1996, *The Astrophysical Journal*, 465, 703
- Lu, N., Zhao, Y., Díaz-Santos, T., et al. 2017, *The Astrophysical Journal*, 842, L16
- Ma, J., Gonzalez, A. H., Spilker, J. S., et al. 2015, *ApJ*, 812, 88
- Madau, P., & Dickinson, M. 2014, *ARA&A*, 52, 415

- Magdis, G. E., Rigopoulou, D., Huang, J.-S., & Fazio, G. G. 2010, *MNRAS*, 401, 1521
- Maraston, C. 2005, *MNRAS*, 362, 799
- Marrone, D. P., Spilker, J. S., Hayward, C. C., et al. 2017, *Nature*, 553, 51
- Martins, F., Schaerer, D., & Hillier, D. J. 2005, *A&A*, 436, 1049
- Marton, G., Calzoletti, L., Perez Garcia, A. M., et al. 2017, *ArXiv e-prints*, arXiv:1705.05693
- Neri, R., Genzel, R., Ivison, R. J., et al. 2003, *ApJ*, 597, L113
- Niemack, M. D., Zhao, Y., Wollack, E., et al. 2008, *Journal of Low Temperature Physics*, 151, 690
- Noll, S., Burgarella, D., Giovannoli, E., et al. 2009, *A&A*, 507, 1793
- Oberst, T. E. 2009, PhD thesis, Cornell University
- Oberst, T. E., Parshley, S. C., Nikola, T., et al. 2011, *The Astrophysical Journal*, 739, 100
- Oberst, T. E., Parshley, S. C., Stacey, G. J., et al. 2006, *The Astrophysical Journal*, 652, L125
- Ott, S. 2010, in *Astronomical Society of the Pacific Conference Series*, Vol. 434, *Astronomical Data Analysis Software and Systems XIX*, ed. Y. Mizumoto, K.-I. Morita, & M. Ohishi, 139
- Parshley, S. C., Ferkinhoff, C., Nikola, T., et al. 2012, in *Proc. SPIE*, Vol. 8452, *Millimeter, Submillimeter, and Far-Infrared Detectors and Instrumentation for Astronomy VI*, 84521R

- Pavesi, R., Riechers, D. A., Capak, P. L., et al. 2016, *ApJ*, 832, 151
- Planck Collaboration, Aghanim, N., Akrami, Y., et al. 2018, arXiv e-prints, arXiv:1807.06209
- Poglitsch, A., Waelkens, C., Geis, N., et al. 2010, *A&A*, 518, L2
- Polletta, M., Tajer, M., Maraschi, L., et al. 2007, *The Astrophysical Journal*, 663, 81
- Rigopoulou, D., Pereira-Santaella, M., Magdis, G. E., et al. 2017, *Monthly Notices of the Royal Astronomical Society*, 473, 20
- . 2018, *Monthly Notices of the Royal Astronomical Society*, 473, 20
- Rubin, R. H. 1985, *ApJS*, 57, 349
- . 1989, *The Astrophysical Journal Supplement Series*, 69, 897
- Schulz, B., Marton, G., Valtchanov, I., et al. 2017, arXiv:1706.00448v1
- Scoville, N., Sheth, K., Aussel, H., et al. 2016, *ApJ*, 820, 83
- Serjeant, S. 2012, *MNRAS*, 424, 2429
- Serra, P., Amblard, A., Temi, P., et al. 2011, *ApJ*, 740, 22
- Solomon, P. M., & Vanden Bout, P. A. 2005, *ARA&A*, 43, 677
- Speagle, J. S., Steinhardt, C. L., Capak, P. L., & Silverman, J. D. 2014, *ApJS*, 214, 15
- Spilker, J. S., Marrone, D. P., Aravena, M., et al. 2016, *The Astrophysical Journal*, 826, 112
- Stacey, G. J., Geis, N., Genzel, R., et al. 1991, *The Astrophysical Journal*, 373, 423

- Stacey, G. J., Hailey-Dunsheath, S., Ferkinhoff, C., et al. 2010, *ApJ*, 724, 957
- Stacey, G. J., Hayward, T. L., Latvakoski, H., & Gull, G. E. 1993, in *Proc. SPIE*, Vol. 1946, *Infrared Detectors and Instrumentation*, ed. A. M. Fowler, 238–248
- Stacey, G. J., Aravena, M., Basu, K., et al. 2018, in *Society of Photo-Optical Instrumentation Engineers (SPIE) Conference Series*, Vol. 10700, *Ground-based and Airborne Telescopes VII*, 107001M
- Staggs, S., Dunkley, J., & Page, L. 2018, *Reports on Progress in Physics*, 81, 044901
- Tacconi, L. J., Neri, R., Genzel, R., et al. 2013, *ApJ*, 768, 74
- Tacconi, L. J., Genzel, R., Saintonge, A., et al. 2017, *ArXiv e-prints*, arXiv:1702.01140
- Tielens, A. G. G. M., & Hollenbach, D. 1985, *ApJ*, 291, 722
- Uzgil, B. D., Bradford, C. M., Hailey-Dunsheath, S., Maloney, P. R., & Aguirre, J. E. 2016, *The Astrophysical Journal*, 832, 209
- Valtchanov, I., Virdee, J., Ivison, R. J., et al. 2011, *MNRAS*, 415, 3473
- Vieira, J. D., Marrone, D. P., Chapman, S. C., et al. 2013, *Nature*, 495, 344
- Vishwas, A., Ferkinhoff, C., Nikola, T., et al. 2018, *The Astrophysical Journal*, 856, 174
- Walter, F., Riechers, D., Novak, M., et al. 2018, *ApJ*, 869, L22
- Wardlow, J. L., Cooray, A., Osage, W., et al. 2017, *ApJ*, 837, 12
- Weiß, A., Breuck, C. D., Marrone, D. P., et al. 2013, *The Astrophysical Journal*, 767, 88

Wong, K. C., Ishida, T., Tamura, Y., et al. 2017, *The Astrophysical Journal*, 843, L35

Wright, E. L., Eisenhardt, P. R. M., Mainzer, A. K., et al. 2010, *AJ*, 140, 1868

Yang, C., Omont, A., Beelen, A., et al. 2016, *A&A*, 595, A80